





This is to certify that the

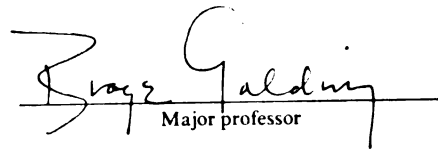
dissertation entitled

Surface Acoustic Wave Investigation of  
Hydrogen Tunneling in Niobium Films at  
Low Temperature  
presented by

Amy K. Bylsma Engebretson

has been accepted towards fulfillment  
of the requirements for

Ph.D degree in Physics

  
Major professor

Date 5/15/98

**LIBRARY**  
**Michigan State**  
**University**

**PLACE IN RETURN BOX**  
to remove this checkout from your record.  
**TO AVOID FINES** return on or before date due.

DATE DUE	DATE DUE	DATE DUE
MAR 30 2000		
<del>MAR 24 2004</del>		
MAR 23 2004		

**SURFACE ACOUSTIC WAVE INVESTIGATION OF HYDROGEN TUNNELING IN  
NIOBIUM FILMS AT LOW TEMPERATURES**

**By**

**Amy K. Bylsma Engebretson**

**A DISSERTATION**

**Submitted to  
Michigan State University  
in partial fulfillment of the requirements  
for the degree of**

**DOCTOR OF PHILOSOPHY**

**Department of Physics and Astronomy**

**1998**

## ABSTRACT

### SURFACE ACOUSTIC WAVE INVESTIGATION OF HYDROGEN TUNNELING IN NIOBIUM FILMS AT LOW TEMPERATURES

By

Amy K. Bylsma Engebretson

The tunneling of hydrogen in niobium at temperatures below 10 Kelvins is of great interest as it represents a model system in which a well known tunneling atom interacts with electrons and phonons. This tunneling system has been studied thoroughly in bulk samples of Nb:H. Prior results have been explained successfully with a "standard model" containing a narrow density of states, a low-energy cutoff, and a weak tunneling system-phonon coupling. The tunneling of hydrogen in thin polycrystalline films of Nb, however, has not been studied. We have used GHz surface acoustic waves to examine the properties of Nb:H films to see if the standard model applied to thin films. The changes in attenuation and velocity of the surface waves were measured from 0.1 K to 10 K. The standard model explains our results in a qualitative way. To improve agreement with the data, a small number of strongly-coupled tunneling systems must be added to the model. We also find indications that states may exist at energies excluded from the standard model.

**To my family**

## ACKNOWLEDGEMENTS

I wish to acknowledge my thesis advisor, Dr. Brage Golding for providing the support, both tangible and intangible, necessary for carrying out this research.

In addition I would like to thank those who have passed on their knowledge of techniques and helped me with the many experimental conundrums which confront a beginning graduate student, Dr. Glenn Alers, Eric Meixner, Mike Jaeger and Dr. Wenhao Wu.

I owe much gratitude to Lowell McCann for being a being a good companion in our pursuits of the elusive Ph.D. He has been a sounding board for ideas and a friend during times of discouragement. In addition I wish to thank Dr. Boakang Bi for helping make the basement a pleasant place to be.

The “shop guys” Tom Palazzolo, Jim Muns and Tom Hudson must be thanked for all of their help in the design and fabrication of equipment. In addition their willingness to teach me to use the machine shop (and to come running when the equipment made a funny noise) was much appreciated. Also I wish to thank Stephanie Holland for untangling the many bureaucratic snafus which occur at a university of this size.

And finally and most importantly I wish to thank my family. My husband Dan has been a rock of support. Without him, this degree would not have possible. Ariel, our daughter, has brought great joy and many smiles on gray days. And thanks to my parents who never told me that anything was too difficult for me to try.

## TABLE OF CONTENTS

LIST OF TABLES.....	viii
LIST OF FIGURES.....	ix
I. Introduction.....	1
II Background.....	4
II. 1. The Niobium:Hydrogen System.....	4
III.1.i Self trapping of hydrogen in niobium.....	6
III.1.ii Trapping of hydrogen by impurities.....	6
III.1.iii Evidence for hydrogen tunneling in niobium.....	7
III.2 Tunneling system model.....	8
III.2.i General description of a two level tunneling system.....	8
III.2.ii Distribution of tunneling energies.....	10
III.2.iii Tunneling system interactions: phonons and electrons.....	12
III.2.iv Change in velocity and attenuation of phonons due to tunneling systems.....	18
III. Experimental.....	23
III. 1. Acoustics.....	23
III.1.i Interactions between thin films and surface acoustic waves.....	27
III.1.ii. Design of Transducers.....	31
III.2 Electron beam lithography.....	35
III.3 Characterization of transducers.....	42
III.3.i Saw device characteristics.....	43

III.4 Niobium film deposition.....	45
III.4.i Description of UHV system.....	45
III.4.ii Evaporation of niobium films.....	46
III.4.iii Characterization of films.....	48
III.4.iv SAW devices with Nb film overlayers.....	51
III.5 Low Temperatures.....	55
III.6 Electronics.....	58
IV. Results.....	65
IV.1 Velocity measurements.....	66
IV.2 The change in velocity in the acoustic path.....	69
IV.2.i. Method for measuring the change in velocity.....	69
IV.2.ii Results from Run 4.16.....	70
IV.3 Change in Attenuation.....	72
IV.3.i Attenuation change between 10 and 300 K, Run 4.16.....	72
IV.3.ii Change in attenuation below 11 K, Run 4.16.....	74
IV.3.iii Change in attenuation below 11 K, Run 4.15.....	77
IV.3.iv Search for nonlinear propagation below 1K.....	79
IV.4 Discussion of the behavior near $T_c$ .....	80
IV.5 Magnetic field data.....	81
V. Discussion.....	84
V.1 Qualitative discussion of results.....	84
V.2. Tunneling systems in Nb:H.....	85
V.2.i Velocity and attenuation dependence on parameters.....	86
V.3 The polycrystalline data described by the standard tunneling model.....	92
V.3.i Method for fitting the standard model to the Nb:H film data.....	92

V.3.ii. Fits to the standard Nb:H tunneling model.....	94
V.3.iii Comparison of Nb:H film and single crystal tunneling parameters...	97
V.3.iv Fit after temperature-dependent $(\Delta v/v)_{anh}$ has been subtracted.....	100
V.4 Evidence for anomalous attenuation.....	102
V.5 Summary and Conclusions.....	104
V.6 Future experiments.....	105
Appendix A, Circuitry.....	109
A.1 The circuit used above 1.2 K.....	109
A.1.i Pulse forming circuit.....	109
A.1.ii Detection circuit.....	112
A.1.iii Phase Lock Circuit.....	114
A.2 The circuit used below 1.2 K.....	116
Appendix B, Velocity measurements.....	118
B.1 Measuring the velocity at constant temperature.....	118
B.2 Derivation of frequency to velocity conversion factor.....	120
B.2.i General derivation.....	121
B.2.ii Specific derivation for Run 4.16.....	122
B.2.iii The conversion for Run 4.15.....	124
Appendix C, Thermometer Calibrations.....	125
C.1 Run 4.15.....	125
C.2 Run 4.16.....	126
Appendix D, Previous Research on Nb:H.....	128

## LIST OF TABLES

Table 3.1. The delays and velocities measured at room temperature .....	53
Table 3.2. The measured lengths in the acoustic channels .....	54
Table 4.1. Delays and velocities measured in Run 4.16.....	68
Table 4.2. Summary of attenuation changes, 6 to 300 K.....	74
Table B.1. The phase, $\phi$ , of the two paths before and after the velocity changes in Path B.....	121

## LIST OF FIGURES

- Figure 2.1. The phase diagram for  $\text{NbH}_x$  after T. Schober and H. Wenzl.....5
- Figure 2.2. Tetrahedral interstitial sites in a BCC lattice. The large circles are the host atoms and the smaller are the tetrahedral sites. From H. Wipf. ....5
- Figure 2.3. Two Nb bcc unit cells. Nb atoms occupy the vertices. The tetrahedral sites are denoted by letters and an octahedral site occupied by a large atom, e.g. O, N, or C is depicted as a filled circle.....6
- Figure 2.4. Temperature dependence of the specific heat from Ref(1).  $\circ$  is nominally pure Nb,  $\square$  is  $\text{NbN}_{0.003}$ ,  $\triangle$  is  $\text{NbH}_{0.002}$ ,  $\diamond$  is  $\text{NbN}_{0.006}\text{H}_{0.002}$ ,  $\blacklozenge$  is  $\text{NbN}_{0.003}\text{D}_{0.002}$ . The solid curves are guides to the eye, the dashed curves are the data from Ref. (1), and the dot-dashed line is the calculated specific heat for pure Nb.....8
- Figure 2.5. Double potential wells, (a) symmetric wells; (b) asymmetric wells,  $d$  is the generalized coordinate between sites and  $V$  barrier height.....9
- Figure 2.6. Normalized density of states described by Eq. 2.3. Dashed line,  $W/k_B = 5$  K, solid line,  $W/k_B = 30$  K, and dotted line,  $\Delta_0/k_B = 1$  K.....11
- Figure 2.7. The density of states for an amorphous material.  $r = 1$  corresponds to symmetric double wells.....12
- Figure 2.8.  $T_{1,el}^{-1}$  as a function of temperature for different  $E / \Delta(0)$ .  $T_{1,el}^{-1}$  is calculated every 0.2 K with  $E = \Delta_0$  and  $K = 0.15$ .....15
- Figure 2.9. Relaxation rates for  $E = \Delta_0 = 0.033\text{K}$  with  $K=0.15$ , and  $\gamma = 0.023$  eV.....17
- Figure 2.10. Relaxation rates for  $E = \Delta_0 = 20$  K with  $K = 0.15$ , and  $\gamma = 0.023$  eV.....17
- Figure 2.11. The resonant, relaxational and total velocity for superconducting Nb with  $\Delta_0 = 0.7$  K,  $W = 30$  K,  $T_c = 8.4$  K,  $\gamma = 0.023$  eV,  $K = 0.15$ ,  $\omega = 4.3 \times 10^9$  s<sup>-1</sup> and  $v = 3.1 \times 10^5$  cm/s. The velocities' amplitudes are set so that  $n_o \gamma^2 / \pi \rho v^2 k_B = 10^{-4}$  K. No offset was added to the velocities.....19
- Figure 3.1. Rayleigh wavefronts, from Morgan.....25

Figure 3.2. The motion of the atoms in a Rayleigh wave. The dots are the equilibrium position of the atoms and the lines are their displaced positions. The dotted circles are the particle trajectories (from Morgan).....26

Figure 3.3. Schematic of a double electrode transducer.  $\lambda$  is the periodicity or wavelength,  $W$  is the aperture, the number of repetitions,  $N_p$ , is 3. The ground and ac electrical connections are shown.....32

Figure 3.4. Standard process of electron beam lithography. a) resist is spun onto the substrate, b) exposure by electrons, c) development, d) metal is deposited, and e) lift off.....36

Figure 3.5. The pattern used to write the transducers. Irregularities of the fingers are due to the resolution of the printer and are not part of the pattern.....39

Figure 3.6. Schematic of the substrates with an inset SEM picture of the electrodes....40

Figure 3.7. A side view of the room temperature sample holder. The short plugs in the back row are the ground contacts while the coaxial lines in the front row carry the ac signal.....42

Figure 3.8. The resonance curves of the two channels as measured in the room temperature tester.  $\blacksquare$  is the A channel and  $\circ$  is the C channel. The curves have been offset for clarity.....43

Figure 3.9. A schematic of the UHV chamber in which the Nb was evaporated on to the LiNbO<sub>3</sub>. 12" is the distance between the Nb charge and the substrate.....45

Figure 3.10. The pattern used for resistance measurements.....48

Figure 3.11. Resistance measuring circuit. R is a 0.5 M $\Omega$  decade resistor, B is 2 mercury batteries (2.7 V), and V is a HP3457A multimeter.....49

Figure 3.12. The insert for the Oxford Kelvinox. Drawing is adapted from that in the Kelvinox operating manual.....56

Figure 3.13. At left is a side view of one chamber of the heatsink. At the right, the cover has been removed from the chamber so the sapphire substrate is visible. The launcher tongues of the SMA rest on the 0.025" wide gold strip.....57

Figure 3.14. The circuit for measurements above 1.2 K. Pulsed signals are sent to the generating transducer. The attenuation of the signal in the acoustic path is measured by diode detectors. The velocity is measure by phase locking the circuit.....60

Figure 3.15. On the left is a photo of the Kelvinox sample holder with a wired sample. On the right is a schematic of the same. A Nb film is shown between the transducers.....61

Figure 4.1. The effective velocity change with temperature. The high temperature tail is an experimental artifact.....	70
Figure 4.2. The change in velocity below 11 K.....	71
Figure 4.3. The change in velocity below 11 K on a log/linear plot.....	72
Figure 4.4. The change in attenuation as measured during cooling down.....	73
Figure 4.5. Smooth curve extrapolated from the change in attenuation as the samples cooled.....	73
Figure 4.6. The change in attenuation for both samples below 10 K.....	75
Figure 4.7. The change in attenuation in sample A between 0.16 K and 11 K.....	76
Figure 4.8. Log plot of change in attenuation below 11 K.....	76
Figure 4.9. The change in attenuation during Run 4.15.....	78
Figure 4.10. The change in attenuation in Run 4.15 on a log-linear plot.....	78
Figure 4.11. The change in attenuation for 3 different input powers. The attenuation has been normalized by the input power. ( $0.1\text{cm}^{-1} = 0.131\text{ dB}$ ).....	79
Figure 4.12. The change in the velocity, resistance, and attenuation near $T_c$ from Run 4.16.....	80
Figure 4.13. The change in the resistance and attenuation near $T_c$ in Run 4.15.....	81
Figure 4.14. The change in attenuation as a function of temperature with and without an applied magnetic field. The dotted lines represent the $T_c$ of the resistive sample. The temperatures are approximately 0.5 K too low.....	82
Figure 4.15. Effect of magnetic field at 5.5 K. $\square$ , field increasing; $+$ , field decreasing.....	83
Figure 5.1. The change in attenuation and velocity; 3 mm Nb:H sample in Run 4.16....	84
Figure 5.2. Plot of $\Delta v/v$ and attenuation using Eq. 5.1 and 5.2 with several values of $\Delta_0$ . Tunneling parameters are: $W/k_B = 30\text{ K}$ , $\gamma = 0.023\text{ eV}$ , $K = 0.15$ and $\omega = 4.3 \times 10^9\text{ s}^{-1}$ .....	87
Figure 5.3. Plot of $\Delta v/v$ and attenuation using Eq. 5.1 and 5.2 with several values of $K$ . For all plots $\Delta_0/k_B = 0.7\text{ K}$ , $W/k_B = 30\text{ K}$ , $\gamma = 0.023\text{ eV}$ , and $\omega = 4.3 \times 10^9\text{ s}^{-1}$ ....	88
Figure 5.4. Plot of $\Delta v/v$ and attenuation using Eq. 5.1 and 5.2 with several values of $\gamma$ . For all graphs, $\Delta_0/k_B = 0.7\text{ K}$ , $W/k_B = 30\text{ K}$ , $K = 0.15$ , and $\omega = 4.3 \times 10^9\text{ s}^{-1}$ .....	89

- Figure 5.5. Plot of  $\Delta v/v$  and attenuation using Eq. 5.1 and 5.2 several values of  $W$ . For all figures,  $\Delta_0/k_B = 0.7$  K,  $\gamma = 0.023$  eV,  $K = 0.15$ , and  $\omega = 4.3 \times 10^9 \text{ s}^{-1}$  .....90
- Figure 5.6. Effect of a narrow distribution of  $\Delta_0$  on velocity and attenuation due to tunneling. Solid line;  $\Delta_0 = 0.71$  K; dashed line; distribution of  $\Delta_0$  of width 1 K.  $W/k_B = 140$  K,  $\gamma = 0.023$  eV,  $K = 0.17$ , and  $\omega = 4.3 \times 10^9 \text{ s}^{-1}$  .....91
- Figure 5.7.  $(\Delta v/v)_{\text{TLS}}$ . Solid line, calculation with the full electronic relaxation rate; dashed line, calculations using the  $E = 0$  approximate electronic rate.....94
- Figure 5.8. Tunneling contribution to the attenuation,  $\alpha_{\text{TLS}}$ , from the full electronic relaxation rate (solid line); calculated with the approximate relaxation rate (dashed line). The measured attenuation, top curve, includes  $\alpha_{\text{BCS}}$ .....95
- Figure 5.9.  $\Delta_0/k_B = 0.567$  K,  $W/k_B = 18$  K and  $K = 0.189$ . Dotted line,  $\alpha_{\text{BCS}}$ ; dashed line,  $\alpha_{\text{TLS}}$  with full relaxation rate summed with  $\alpha_{\text{BCS}}$ ; solid line,  $\alpha_{\text{TLS}}$  with approximate relaxation rate added to  $\alpha_{\text{BCS}}$ . The solid line falls directly on the data below  $T_c$  and thus the line cannot be seen between 6.5 K and  $T_c$ .  $\alpha$  is assumed equal to zero at 0.2 K.....96
- Figure 5.10. Single crystal  $\text{NbN}_{0.0015}\text{H}_{0.003}$  data from Ref (1). a) velocity, the dashed line is hydrogen free data b.) attenuation, the solid line is hydrogen free data,  $\bullet$  is in the normal state, and  $\circ$  data is from the superconducting state.....97
- Figure 5.11. Single crystal Nb:N:H data from Ref.(1) with our calculations (lines). a)  $\Delta v/v$  at 90 MHz (with no anharmonic correction). b) attenuation (hydrogen free Nb background subtracted).  $\Delta$ ,  $\omega/2\pi = 150$  MHz;  $\circ$ ,  $\omega/2\pi = 90$  MHz;  $\square$ ,  $\omega/2\pi = 30$  MHz.....98
- Figure 5.12. Our data along with the best fit with  $\Delta_0$  fixed at 1.4 K. Solid line is  $(\Delta v/v)_{\text{TLS}}$  and  $\alpha_{\text{TLS}}$  (see text).....99
- Figure 5.13. a) Anharmonic contribution to the velocity with  $\beta = -0.00112$  (solid line) b)  $\Delta v/v$  with anharmonic background subtracted.....100
- Figure 5.14. Fit to the data after an approximate anharmonicity subtracted. In the upper graph: solid line,  $(\Delta v/v)_{\text{TLS}}$ . In the lower graph the linearized attenuation data; dashed line,  $\alpha_{\text{TLS}}$ ; dotted line,  $\alpha_{\text{BCS}}$  with normal amplitude of  $0.24 \text{ cm}^{-1}$ ; solid line,  $\alpha_{\text{TLS}} + \alpha_{\text{BCS}}$ . All were calculated with the full electronic relaxation rate.....101
- Figure 5.15. The residual attenuation after  $\alpha_{\text{TLS}}$  with  $\gamma = 0.023$  eV and  $\alpha_{\text{BCS}}$  have been subtracted. The solid line is the calculation with  $\gamma = 1.85$  eV.....103
- Figure 5.16. The velocity. Dashed line,  $\alpha_{\text{TLS}}$  with  $\gamma = 1.85$  eV; solid line,  $\alpha_{\text{TLS}}$  from the  $\gamma = 0.023$  eV fit plus  $\alpha_{\text{TLS}}$  calculated with  $\gamma = 1.85$  eV.....104

Figure A.1. The pulse forming circuit.....110

Figure A.2. The attenuation measurement circuit.....113

Figure A.3. Phase locking circuit.....115

Figure A.4. The homodyning circuit used below 1.2 K.....117

Figure B.1. A signal is split and travels through two different paths. The signal is then recombined in a mixer and the combined signal observed on an oscilloscope.....118

Figure B.2. A signal is split and travels through two different paths. The velocity is constant in path A and varies in path B. The signal is then recombined in a mixer and sent to the boxcar/integrator which varies the frequency of the signal generator so that constant phase at the mixer is maintained.....121

Figure C.1. The RuO thermometer calibration used in Run 4.15. , th e superconducting standard points measured 2/95.....125

Figure C.2. The Pt thermometer calibration curve. The line is the prtmdj, a spline fit to the data points of Pt95.dat.....126

Figure C.3. RuO calibration during Run 4.16. The points are the conductance read when the superconducting standard underwent transitions as the Kelvinox was heated or cooled.....127

# I. Introduction

For the past two decades, physicists have been fascinated by the tunneling systems found in amorphous solids at low temperatures. These systems offer insights into the interactions between defects and excitations such as electrons and phonons. The phenomenology of tunneling systems in disordered materials has been successfully explained with a two level tunneling model. In this model, the atoms forming the tunneling systems are not specifically identified. The key assumption is that of a distribution of tunneling energies which is responsible for the low temperature properties of the material. The distribution corresponds to a broad and uniform density of states. The tunneling systems in amorphous solids strongly couple to phonons, reducing the thermal conductivity of insulators.

In order to study tunneling processes in more detail, simpler materials in which there is only a single type of tunneling object have proven useful and interesting. A system believed to possess a narrow density of states is hydrogen tunneling systems in transition metals such as Nb. Nb:H is also a superconductor, therefore it is possible to study how the appearance of the superconducting gap modifies the interaction between the conduction electrons and the tunneling systems.

In Nb:H, hydrogen tunnels between two nearly equivalent tetrahedral interstitial sites of the Nb lattice in a double well potential for which an impurity occupying an octahedral site is required. Neutron spectroscopy, specific heat, high frequency phonon attenuation and change in velocity, and low frequency internal friction studies on bulk crystalline Nb:H at temperatures below 20 K have been described successfully with a theory based

upon a narrow distribution of tunneling state energies. These tunneling systems have a relatively weak coupling to both phonons and electrons.

In the present research we have studied polycrystalline films of Nb:H to see if the standard tunneling model would be applicable to thin films as well as single crystals of Nb:H. Films of Nb:H are particularly attractive since they are easily prepared by electron beam evaporation. Hydrogen can be introduced by diffusion subsequent to evaporation since it diffuses rapidly into Nb films. In addition, by varying the deposition conditions and exposure to gaseous dopants, the dopant concentration can be controlled. In principle, the amount of H can be varied from extremely dilute to the highly concentrated phases where hydrogen ordering occurs.

Can polycrystalline films be described by the narrow distribution, weak coupling model? To answer this question, the interaction of high frequency sound waves with tunneling systems have been used to probe the dynamics and distribution of two level states. Surface waves propagate in a region one acoustic wavelength in depth at the surface of a substrate. If a thin film is deposited on the substrate most of the energy is restricted to a small volume, so that the propagation characteristics of sound are strongly affected by the film overlayer. This provides sufficient sensitivity to small changes in sound velocity and attenuation arising from tunneling systems. We wished to see if the distribution of states would be influenced by disorder associated with the polycrystalline texture.

Prior to this research, no surface acoustic wave experiments have provided information on tunneling processes in metals. Therefore, we have studied the tunneling of hydrogen in polycrystalline, thin films of Nb:H to temperatures as low as 100 mK.

Tunneling was probed by measuring the change in attenuation and velocity of 0.7 GHz phonons, introduced into the films via surface acoustic waves, or SAWs.

The narrow density of states with weak coupling to phonons used to describe the tunneling of H in bulk, single crystal Nb has been applied to the thin film system. The model is only qualitatively applicable to our results. We find that a description of the low temperature attenuation requires that the model be modified to incorporate states with a strong coupling to phonons. In addition, we find that there may be states with energies outside of the narrow distribution invoked by the standard Nb:H tunneling model.

### *Outline of the thesis*

In this thesis evidence for the tunneling of hydrogen in Nb is shown by studies of the acoustic attenuation and velocity in thin films of Nb:H. The theoretical and historical background necessary for understanding the standard model for the tunneling of trapped hydrogen in Nb is contained in Chapter II. Chapter III describes the experimental methods used to detect the tunneling of hydrogen. The preparation of the Nb films, generation and detection of surface waves, and the equipment used to cool the samples to 100 mK are discussed here. The results of the measurements are presented in Chapter IV. In Chapter V the results will be compared with the theory outlined in Chapter II. The results for polycrystalline films are contrasted with the properties of bulk samples and necessary modifications to the standard theory presented.

## II Background

### II. 1. The Niobium:Hydrogen System

Niobium is a type II superconductor with a body-centered cubic, bcc, structure. Pure single crystal niobium has a superconducting transition temperature,  $T_c$ , of 9.2 K.<sup>1</sup>

The behavior of hydrogen in niobium is unusual in many ways. Due to its low mass, hydrogen is mobile at all temperatures. However, at relatively low temperatures it does not move from site to site by hopping, but by quantum mechanical tunneling. Relative to hopping rates, tunneling rates are significant for hydrogen in Nb at temperatures as high as 300 K.<sup>2,3</sup>

The Nb:H equilibrium phase diagram is shown in Figure 2.1. In the  $\alpha$  and  $\alpha'$  phases the Nb lattice assumes a bcc structure with hydrogen occupying the tetrahedral interstitial sites as shown in Figure 2.2.<sup>4</sup> All other phases are ordered phases.  $NbH_x$  is unusual in that  $x$  can be greater than 1.

In this thesis we shall be concerned with hydrogen concentrations less than 1%. In this dilute regime, the  $\alpha$  phase exists at room temperature with the hydrogen behaving like a gas: the hydrogen atoms are randomly distributed and there are few H-H interactions. At lower temperatures, hydrogen precipitates into the ordered  $\epsilon$  phase, with an orthorhombic unit cell corresponding to  $Nb_4H_3$ .<sup>4</sup> All hydrogen eventually “precipitates” into the  $\epsilon$  phase. For  $x = 0.01$  the precipitation begins at 220 K, at  $x = 0.001$  it forms at about 160 K, and for  $x = 0.0001$  precipitation begins at about 130 K. By 50 K essentially all free H has been precipitated into the  $\epsilon$  phase.<sup>5,6</sup>

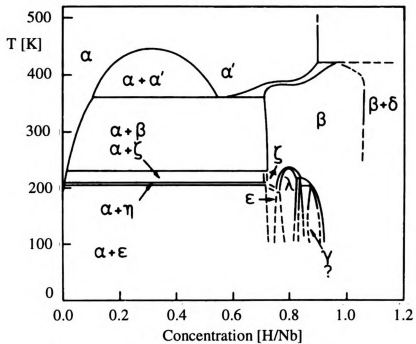


Figure 2.1. The phase diagram for NbH<sub>x</sub> after T. Schober and H. Wenzl.<sup>4</sup>

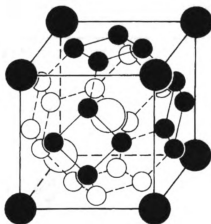


Figure 2.2. Tetrahedral interstitial sites in a BCC lattice. The large circles are the host atoms and the smaller are the tetrahedral sites. From H. Wipf.<sup>7</sup>

### III.1.i Self trapping of hydrogen in niobium

There are two basic ways in which H is trapped in the tetrahedral sites of the Nb. In self-trapping, a H atom in a tetrahedral site displaces the 4 nearest neighbor Nb atoms by about  $0.1 \text{ \AA}$ . The energy difference between the total energies of the undistorted and relaxed Nb lattice is approximately  $450 \text{ meV}$ . This is called the self-trapping energy. The hydrogen cannot move without likewise distorting the lattice at the new site.<sup>8,9</sup>

### III.1.ii Trapping of hydrogen by impurities

Hydrogen can also be trapped in tetrahedral sites upon distortion of the Nb lattice by an O, N, or C impurity at an octahedral site. This distortion breaks the degeneracy of some of the interstitial tetrahedral sites. The specific sites in which H can be trapped are denoted by e in Figure 2.3. Note that there are 16 sites with equivalent energies denoted by e per octahedral impurity. However, each site has only one nearest-neighbor site with equivalent energy at a distance of  $1.17 \text{ \AA}$ . The next nearest site of equivalent energy is

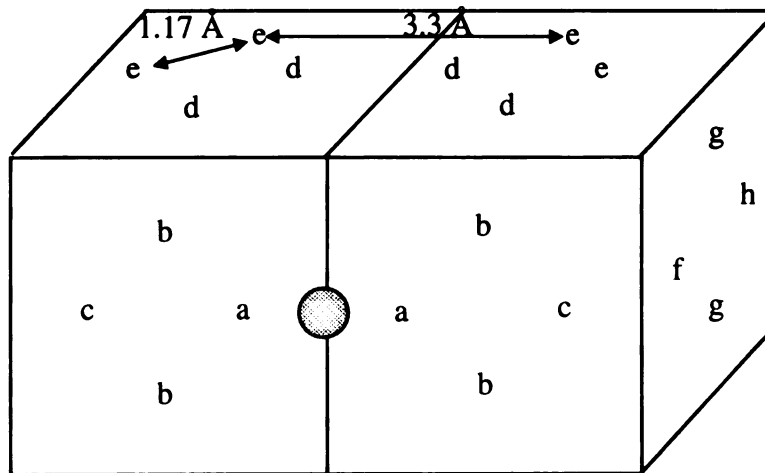


Figure 2.3. Two Nb bcc unit cells. Nb atoms occupy the vertices. The tetrahedral sites are denoted by letters and an octahedral site occupied by a large atom, e.g. O, N, or C is depicted as a filled circle.

3.3 Å away. Thus at temperatures below 150 K, the H is trapped in the double well formed by two nearest neighbor e sites.<sup>10</sup> The occupied sites were ascertained by considering the vibrational energy of trapped hydrogen and limitations introduced by specific heat data on the tunneling distance between the two sites.<sup>6</sup> Only one H may be trapped per octahedral impurity.<sup>5</sup>

### III.1.iii Evidence for hydrogen tunneling in niobium.

Sellers, Anderson, and Birnbaum<sup>11</sup> noted that specific heat measurements of Nb between 0.06 and 2 K exhibited a contribution which could not be ascribed to either lattice or electronic effects. This contribution depended upon the concentration of hydrogen, or deuterium, in the Nb. Based upon a large isotope effect, they attributed this additional term in the specific heat to some sort of tunneling of hydrogen. Morkel, Wipf, and Neumaier<sup>12</sup> extended the specific heat measurements and found that the specific heat only deviated from that of pure Nb when the Nb contained both N and H, as shown in Figure 2.4. In addition, they verified the isotope dependence observed by Sellers et al.. The isotope dependence is an indication that the deviation is due to contributions to the specific heat by tunneling systems. This is due to the fact that which tunneling states can contribute to the specific heat is dependent upon the tunneling matrix element (which will be formally introduced in III.2.i). The tunneling matrix element is dependent on the mass of the tunneling object; a larger mass corresponds to a smaller tunneling matrix element. A smaller tunneling matrix element corresponds to a lower temperature at which the tunneling systems cease to contribute to the specific heat.<sup>13</sup> Thus tunneling D will continue to contribute to the specific heat at lower temperatures than tunneling H

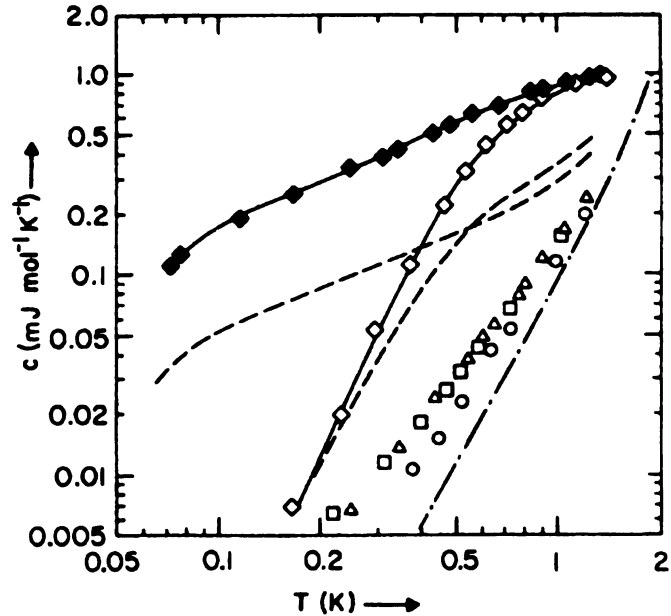


Figure 2.4. Temperature dependence of the specific heat from Ref(12).  $\circ$  is nominally pure Nb,  $\square$  is  $\text{NbN}_{0.003}$ ,  $\triangle$  is  $\text{NbH}_{0.002}$ ,  $\diamond$  is  $\text{NbN}_{0.006}\text{H}_{0.002}$ ,  $\blacklozenge$  is  $\text{NbN}_{0.003}\text{D}_{0.002}$ . The solid curves are guides to the eye, the dashed curves are the data from Ref. (11), and the dot-dashed line is the calculated specific heat for pure Nb.

as shown in the data of Figure 2.4.

Therefore it was concluded that the excess specific heat was due to hydrogen (deuterium) tunneling between the two sites of a double potential well associated with the occupation of an octahedral impurity site. Additional specific heat, neutron scattering and acoustic experiments that bear on the tunneling of hydrogen trapped by octahedral impurities in Nb are summarized in Appendix D.

### III.2 Tunneling system model

#### III.2.i General description of a two level tunneling system

At low temperatures many of the properties of Nb are dominated by the tunneling of

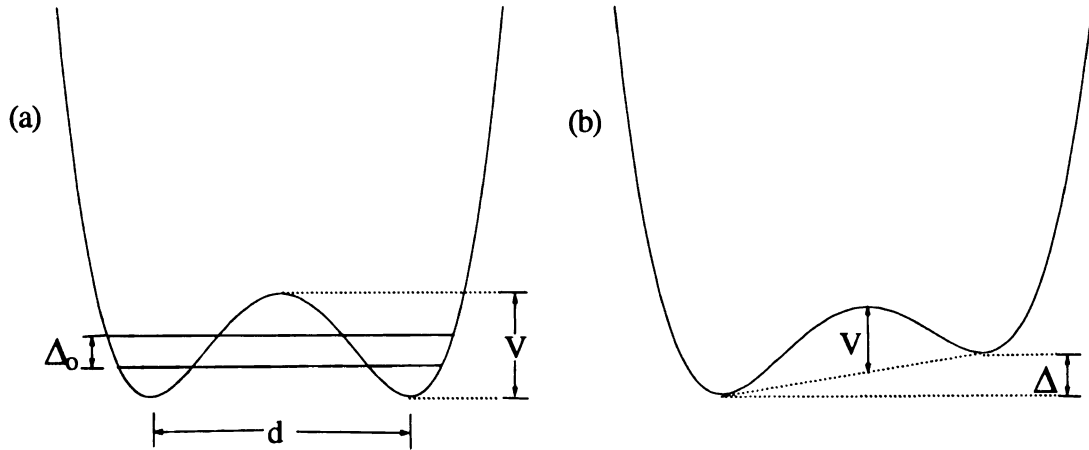


Figure 2.5. Double potential wells, (a) symmetric wells; (b) asymmetric wells,  $d$  is the generalized coordinate between sites and  $V$  barrier height.

hydrogen at tetrahedral interstitial sites associated with octahedral impurities. This double potential well in which the hydrogen resides can be described by a two level tunneling model.

Figure 2.5 is a schematic diagram of one dimensional symmetric and asymmetric potential wells that lead to low-lying energy levels. For interstitial hydrogen trapped by octahedral impurities in niobium, the left and right well would correspond to the nearest neighbor tetrahedral interstitial sites with  $d \cong 1.17 \text{ \AA}$  and  $V \approx 70 \text{ meV}$ .<sup>14</sup>

The Hamiltonian of a particle in a double well can be written as

$$H_0 = \frac{1}{2} \begin{pmatrix} \Delta & -\Delta_0 \\ -\Delta_0 & -\Delta \end{pmatrix} \quad (2.1)$$

where  $\Delta$  is the asymmetry energy of the two wells,  $\Delta_0$  is the tunneling matrix element (a measure of the mixing of the two wells):  $\Delta_0 = \hbar \omega_0 \exp(-\lambda)$ , where  $\lambda = d\hbar^{-1} \sqrt{2mV}$ ,  $m$  is the effective mass of the tunneling object, and  $\hbar \omega_0$  is the vibrational energy of a single well. The eigenstates of this two level tunneling system are symmetric and

antisymmetric superpositions of the wavefunctions of the left and right wells. In the symmetric case, the energy splitting  $E$  between the two states is just  $\Delta_0$ , the tunneling matrix element. With asymmetric wells,  $E = \sqrt{\Delta^2 + \Delta_0^2}$ , which is obtained by diagonalizing Eq. 2.1.<sup>13,15,16,17</sup>

### III.2.ii Distribution of tunneling energies.

Hydrogen's lowest vibrational energy in niobium is extremely high  $\hbar\omega_0 = 100$  meV ( $\sim 1100$  K).<sup>8</sup> Since this vibrational energy is greater than or on the order of the barriers between the interstitial sites, it is unlikely that the hydrogen can hop over the barrier. Rather the hydrogen tunnels between interstitial sites below room temperature.

In  $\text{NbH}_x(\text{O,N,C})_y$  (where  $x$  is the atomic percent of hydrogen and  $y$  is the atomic percentage of impurities, such as O, N, or C, occupying the octahedral sites) with only one type of atomic tunneling object, the distribution of tunneling energies should be a delta function. In most materials, however, the tunneling sites are not identical due to structural imperfections leading to a distribution of energies. These effects lead to a broadening of resonance lines as studied by Stoneham.<sup>18</sup> The sources of spectral broadening were described and experimental results were compared to continuum and discrete lattice models. The basic assumptions made in finding the line shape were that the transition energy is linear in local strain, that all contributions to the energy by defects add linearly and the defects are dilute enough so that they are not correlated. By looking at the distribution of energies of centers and the distribution's effect on the line width, it was shown that the strain introduced by point defects leads to a Lorentzian line shape. In experiments on doped NaCl it was found that the zero phonon line at very low

concentrations of defects was nearly Gaussian due to dislocations in the NaCl. As the point defect concentration increased the defects' influence on the line shape increased and the broadening became progressively more Lorentzian.

Since the asymmetry of a  $\text{NbH}_x(\text{O},\text{N},\text{C})_y$  tunneling system is due to random strain caused by point defects, the distribution of asymmetry energies is represented by a Lorentzian function centered at zero energy.

$$n(\Delta) = \frac{dn}{d\Delta} = \frac{n_o}{\pi} \frac{W}{W^2 + \Delta^2} \quad (2.2)$$

where  $n_o$  is the total number of states,  $W$  is the width of the distribution at half maximum and  $\int_{-\infty}^{\infty} n(\Delta) d\Delta = n_o$ . The distribution leads to a tunneling density of states given by

$$n(E) = 2 \frac{dn}{d\Delta} \frac{d\Delta}{dE} = 2 \frac{n_o}{\pi} \frac{W}{W^2 + (E^2 - \Delta_o^2)} \frac{E}{\sqrt{E^2 - \Delta_o^2}} \quad (2.3)$$

where  $\int_0^{\infty} n(E) dE = n_o$ .  $n(E)$  diverges as  $E \rightarrow \Delta_o$  and there are no states for  $E < \Delta_o$  as

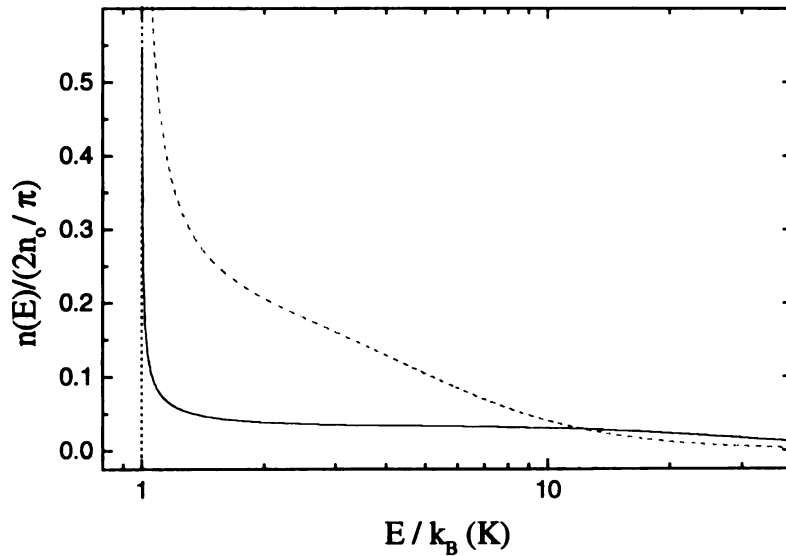


Figure 2.6. Normalized density of states described by Eq. 2.3. Dashed line,  $W/k_B = 5$  K, solid line,  $W/k_B = 30$  K, and dotted line,  $\Delta_o/k_B = 1$  K.

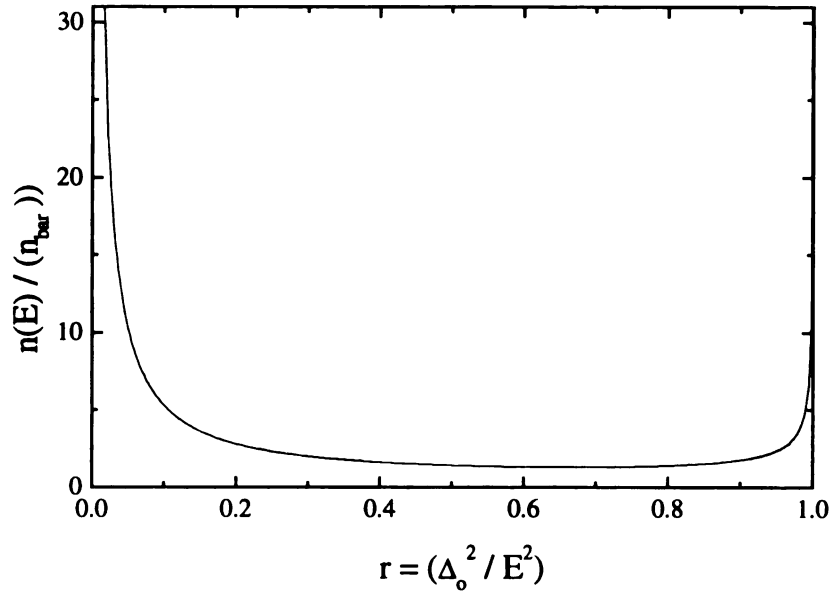


Figure 2.7. The density of states for an amorphous material.  $r = 1$  corresponds to symmetric double wells.

shown in Figure 2.6. As the width increases, more states exist at higher energies.

In a highly disordered system, such as glasses or a system with a high concentration of defects, e.g. KBr-KCN, there will be distributions of  $\Delta_0$  as well as  $\Delta$ . The density of states in this case is described by a standard distribution function,

$$n(E, r) = \frac{1}{2} \bar{n} \frac{1}{r\sqrt{1-r}} \quad (2.4)$$

where  $\bar{n}$  is the defect concentration and  $r = (\Delta_0 / E)^2$ .<sup>20</sup> Figure 2.7 is a plot of this distribution.

### III.2.iii Tunneling system interactions: phonons and electrons

In a metal two level tunneling systems can interact with phonons and electrons. In many cases these interactions can be treated as perturbations of  $H_0$ . The full Hamiltonian written in the basis of the eigenstates of  $H_0$  is given by

$$H = ES_z + (2MS_x + DS_z)\varepsilon + N^{-1}(v_{\perp}S_x + v_{\parallel}S_z)\sum_{\mathbf{kq}} c_{\mathbf{k}}^{\dagger}c_{\mathbf{k+q}} \quad (2.5)$$

where the  $S_i$  are spin  $1/2$  operators,  $M = \Delta_0\gamma / E$ ,  $D = 2\Delta\gamma / E$ ,  $\gamma = d\Delta/d\varepsilon$  (phonon-tunneling system coupling),  $\varepsilon$  is the phonon strain field,  $N$  is the number of atoms,  $v_{\perp}$  and  $v_{\parallel}$  are the off diagonal and diagonal electron-tunneling system coupling matrix elements, and  $c^{\dagger}$  and  $c$  are the electron creation and annihilation operators.<sup>19,20</sup> The phonon-tunneling system coupling parameter  $\gamma$  for H in Nb determined from acoustic experiments is  $\approx 0.02$  eV. This can be contrasted with intrinsic tunneling states in amorphous metals where  $\gamma$  is on the order of 1 eV. The electron-tunneling system coupling is often expressed in terms of  $K$ , a dimensionless parameter where  $v_{\perp}$  and  $K$  are related by the expression,  $(\rho v_{\perp})^2 = 2K(\Delta_0/E)^2$ .  $\rho$  is the electronic density of states per atom at the Fermi energy. For Nb:H  $K \approx 0.1$ , consistent with the upper limit  $K \leq 0.5$ .<sup>21</sup>

#### *Phonon interactions with tunneling systems*

We shall be concerned with two classes of processes that phonons have with two level tunneling systems: resonant and relaxational. In the resonant interaction which dominates below a few  $K$ , a phonon with energy equal to the energy splitting of the levels,  $\hbar\omega = E$ , is absorbed and the TLS is excited into its upper state. A resonant phonon incident upon a tunneling system in its excited state will stimulate the emission of a phonon with frequency  $E/\hbar$ .

For a one-phonon process, the rate at which the tunneling system decays from the excited to the ground state is given by<sup>22</sup>

$$T_{1,\text{ph}}^{-1} = \frac{\gamma^2}{v^5} \frac{E\Delta_0^2}{2\pi\rho\hbar^4} \coth\left(\frac{E}{2k_B T}\right) \quad (2.6)$$

In the relaxational process the phonons induce a distortion in the asymmetry and thus the populations of the two states. The time for the system to relax to its original configuration is  $T_1$ .

*Electron interactions with tunneling systems.*

Electrons as well as phonons can relax tunneling systems. In the normal state, the electrons relax the tunneling systems by a Korringa-like decay rate which is given by,<sup>19</sup>

$$T_{1,el,n}^{-1} = \frac{\pi K}{2\hbar} \left( \frac{\Delta_o}{E} \right)^2 E \coth \left( \frac{E}{2k_B T} \right) \quad (2.7)$$

If the metal is superconducting, the electronic relaxation rate is modified by the BCS-like superconducting gap,  $\Delta(T)$ , and is given by

$$\begin{aligned} T_{1,el}^{-1} = & \frac{\pi K}{2\hbar} \left( \frac{\Delta_o}{E} \right)^2 \int_{-\infty}^{\infty} d\varepsilon_1 \int_{-\infty}^{\infty} d\varepsilon_2 n(\varepsilon_1) n(\varepsilon_2) \left( 1 - \frac{\Delta(T)^2}{\varepsilon_1 \varepsilon_2} \right) f(\varepsilon_1) f(\varepsilon_2) \delta(\varepsilon_2 - \varepsilon_1 - E) \\ & + \frac{\pi K}{2\hbar} \left( \frac{\Delta_o}{E} \right)^2 \int_{-\infty}^{\infty} d\varepsilon_1 \int_{-\infty}^{\infty} d\varepsilon_2 n(\varepsilon_1) n(\varepsilon_2) \left( 1 - \frac{\Delta(T)^2}{\varepsilon_1 \varepsilon_2} \right) f(\varepsilon_1) f(\varepsilon_2) \delta(\varepsilon_2 - \varepsilon_1 + E) \end{aligned} \quad (2.8)$$

where  $\varepsilon$  = the electron energy,  $n(\varepsilon) = \begin{cases} |\varepsilon| / \sqrt{\varepsilon^2 - \Delta(T)^2} & \text{if } |\varepsilon| > \Delta(T) \\ 0 & \text{if } |\varepsilon| \leq \Delta(T) \end{cases}$ , and  $f(\varepsilon)$  is the

Fermi-Dirac function equal to  $1/(\exp(\varepsilon/k_B T) + 1)$ .<sup>23</sup> Note that the symbol for the superconducting gap,  $\Delta(T)$ , is similar to that for the asymmetry,  $\Delta$ , of the tunneling systems. Since the asymmetry is not temperature dependent it will always be denoted by  $\Delta$  whereas the temperature dependent superconducting gap will be denoted by  $\Delta(T)$ .

As the electrons form Cooper pairs in the superconducting state, they cease to relax the tunneling systems with the mechanism described in Eq. 2.8. Therefore well below  $T_c$ , the electronic relaxation rate rapidly approaches zero. When  $E > 2\Delta(T)$ , however, an

additional relaxation channel for the tunneling systems exists as the tunneling systems can create or annihilate a pair of quasiparticles. This results in a relaxation rate greater than the normal relaxation rate. At  $E = 2\Delta(T)$  there is a discontinuity in the relaxation rate as this additional channel is closed. Both of these phenomena are accounted for by Eq. 2.8. Solving this equation, however, requires numerical integration. In the  $E \rightarrow 0$  limit, which neglects pair breaking, the solution to Eq. 2.8 below  $T_c$  is

$$T_{1,\text{el},s}^{-1} = \frac{2\pi K}{\hbar} \left( \frac{\Delta_0}{E} \right)^2 \frac{k_B T}{e^{\Delta(T)/k_B T} + 1} \quad (2.9)$$

Above  $T_c$ , Eq. 2.8 simplifies to Eq. 2.7.

In Figure 2.8 the full electronic relaxation rate calculated for different values of  $E / \Delta(0)$  is shown and compared to the low energy approximation. The discontinuity in the electronic relaxation rate at  $E = 2\Delta(T)$  is apparent. The  $E \rightarrow 0$  approximation is

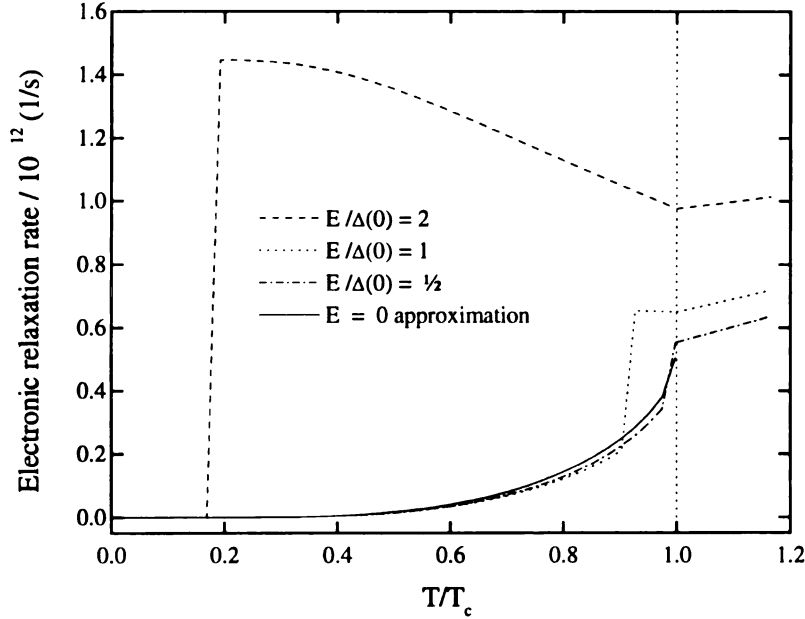


Figure 2.8.  $T_{1,\text{el}}^{-1}$  as a function of temperature for different  $E / \Delta(0)$ .  $T_{1,\text{el}}^{-1}$  is calculated every 0.2 K with  $E = \Delta_0$  and  $K = 0.15$ .

inaccurate near  $T_c$  when  $E / \Delta(0) \gtrsim 0.5$ . When  $E / \Delta(0) = 0.1$ , the zero energy approximation deviates from the full electronic relaxation rate by less than 3% near  $T_c$ . At temperatures  $T < 0.4 T_c$  the rates are on the order of GHz or lower and the deviation of Eq. 2.9 from Eq. 2.8. rises from 3% to 8% with falling rates and temperature.

*Numerical estimates of relaxation rates for Nb:H.*

Using parameters valid for niobium, the phononic and electronic rates were calculated for various energy splittings. In Figures 2.9 and 2.10 the relaxation rates are shown for  $E = \Delta_0 = 0.033$  K, corresponding to  $\omega = 2\pi \times 700$  MHz phonons, and  $E = \Delta_0 = 20$  K. The couplings  $K = 0.15$ , and  $\gamma = 0.023$  eV were used along with Eq. 2.6 and 2.8 to calculate the phononic and electronic relaxation rates respectively. A superconducting transition temperature of 8.4 K, similar to our samples, was used in calculating the electronic relaxation rate. When  $E / k_B = 0.033$  K,  $T_{1,ph}^{-1}$  is on the order of a few hundred Hz.  $T_{1,el}^{-1}$  is less than the  $T_{1,ph}^{-1}$  below 0.6 K but then quickly rises to the hundreds of GHz. For  $E = \Delta_0 = 20$  K,  $T_{1,ph}^{-1}$  is on the order of  $10^8$  Hz and  $T_{1,el}^{-1}$  is less than  $T_{1,ph}^{-1}$  until 2 K at which time it quickly rises into the  $10^{11} - 10^{12}$  Hz regime. Thus, in superconducting niobium with  $E \leq 20$  K,  $T_{1,ph}^{-1}$  is dominant at temperatures less than a few Kelvin.  $T_{1,el,s}^{-1}$  and thus the relaxational interaction dominate at higher temperatures. In normal niobium and for high energy tunneling system splittings the electronic relaxation rate dominates at all temperatures.

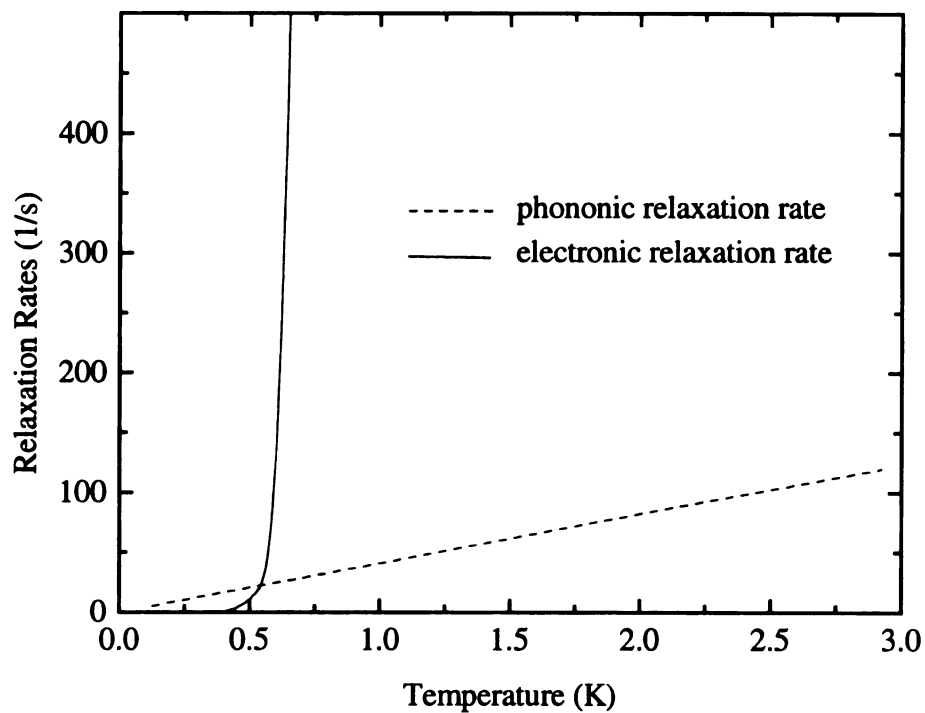


Figure 2.9. Relaxation rates for  $E = \Delta_0 = 0.033K$  with  $K = 0.15$ , and  $\gamma = 0.023$  eV.

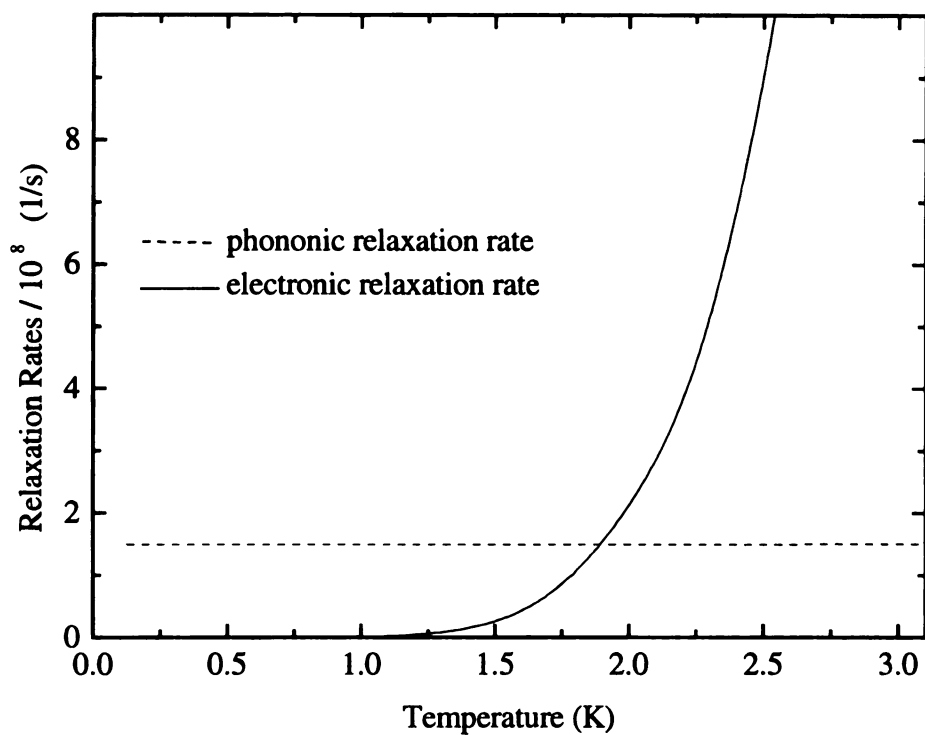


Figure 2.10. Relaxation rates for  $E = \Delta_0 = 20$  K with  $K = 0.15$ , and  $\gamma = 0.023$  eV.

### III.2.iv Change in velocity and attenuation of phonons due to tunneling systems.

The change in velocity of phonons due to the resonant interaction is given by

$$\left(\frac{\Delta v}{v}\right)_{\text{res}} = -\frac{n_o \gamma^2}{\rho v^2} \left(\frac{\Delta_o}{E}\right)^2 \frac{1}{E} \tanh\left(\frac{E}{2k_B T}\right) \quad (2.10)$$

where  $n_o$  is the concentration of tunneling systems,  $\rho$  is the density and  $v$  is the sound velocity of the material.<sup>24,25</sup> In order to calculate  $\Delta v/v$  (attenuation) for a specific type of tunneling system,  $n_o$  is replaced by the proper distribution and the velocity (attenuation) integrated over the distributed variable. As an example, with a Lorentzian distribution of  $\Delta$  the resonant change in velocity is given by

$$\left(\frac{\Delta v}{v}\right)_{\text{res}} = -\int_{-\infty}^{\infty} n(\Delta) \frac{\gamma^2}{\rho v^2} \left(\frac{\Delta_o}{E}\right)^2 \frac{1}{E} \tanh\left(\frac{E}{2k_B T}\right) d\Delta \quad (2.11)$$

Because of the negative sign  $\left(\frac{\Delta v}{v}\right)_{\text{res}}$  rises with increasing temperature until a maximum is reach at which point it becomes temperature independent as shown in Figure 2.11. For amorphous materials the velocity varies as  $\log T$ .

The relaxational attenuation and change in velocity are given by<sup>19</sup>

$$\alpha_{\text{rel}} = \frac{n_o \gamma^2}{\rho v^3} \frac{1}{k_B T} \left(\frac{\Delta}{E}\right)^2 \frac{\omega^2 T_1}{1 + \omega^2 T_1^2} \text{sech}^2\left(\frac{E}{2k_B T}\right) \quad (2.12)$$

$$\left(\frac{\Delta v}{v}\right)_{\text{rel}} = -\frac{n_o \gamma^2}{2\rho v^2} \frac{1}{k_B T} \left(\frac{\Delta}{E}\right)^2 \frac{1}{1 + \omega^2 T_1^2} \text{sech}^2\left(\frac{E}{2k_B T}\right) \quad (2.13)$$

where  $T_1^{-1} = T_{1,\text{el}}^{-1} + T_{1,\text{ph}}^{-1}$  and  $\omega$  is the phonon frequency. As one can see in Eq. 2.12,

when  $T_1^{-1} = \omega$ , a peak in the attenuation results. For dilute defects, there is a distribution of  $T_1^{-1}$  which will broaden the peak. As shown in Eq. 2.13 the relaxational velocity will fall after being temperature independent at the lowest temperatures (when  $\omega T_1 > 1$ ).

Figure 2.11 shows the resonant, Eq. 2.10, and relaxational terms, Eq. 2.13, of the change in velocity for tunneling systems integrated over a Lorentzian distribution of asymmetries with  $T_1^{-1}$  equaling the sum of Eq. 2.9 and Eq. 2.6. A peak is observed in the sum of the two terms as  $T_{1,el}^{-1}$  becomes much greater than  $T_{1,ph}^{-1}$  and there is a crossover between the resonant and relaxational processes dominating.

When integrated over the broad distribution necessary for an amorphous material the relaxational attenuation must be calculated numerically. Essentially, the relaxational

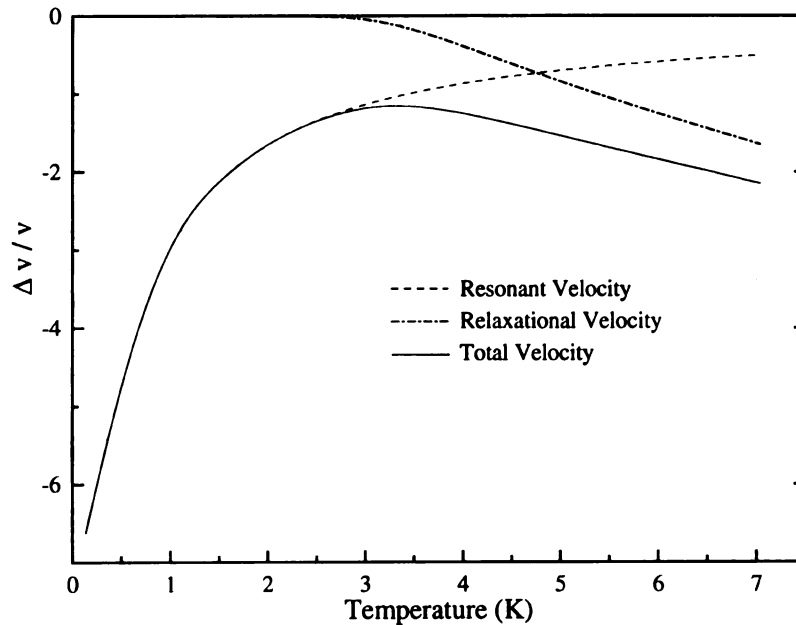


Figure 2.11. The resonant, relaxational and total velocity for superconducting Nb with  $\Delta_0 = 0.7$  K,  $W = 30$  K,  $T_c = 8.4$  K,  $\gamma = 0.023$  eV,  $K = 0.15$ ,  $\omega = 4.3 \times 10^9$  s $^{-1}$  and  $v = 3.1 \times 10^5$  cm/s. The velocities' amplitudes are set so that  $n_0 \gamma^2 / \pi \rho v^2 k_B = 10^{-4}$  K. No offset was added to the velocities.

contribution to the attenuation is zero at the lowest temperatures and then rises with increasing temperature until it reaches a temperature independent plateau. For  $\omega T_1 \ll 1$

the relaxational change in the velocity saturates at  $-\frac{1}{2} \left( \frac{\Delta v}{v} \right)_{\text{res}}$ .<sup>26</sup>

- 
- <sup>1</sup> “Superconductivity in the metal-hydrogen system”, B. Stritzker and H. Wühl, in *Hydrogen in Metals II*, edited by G. Alefeld and J. Völkl (Springer-Verlag, New York, 1978) pp. 243-272.
- <sup>2</sup> “Quantum theory of diffusion with application to light interstitials in metals”, C.P. Flynn and A.M. Stoneham, *Physical Review B* 1, 3966-3978 (1970).
- <sup>3</sup> “Quantum transition state theory and the diffusion of hydrogen in metals”, M.J. Gillian *Journal of the Less-Common Metals* 172-174, 529-537 (1991).
- <sup>4</sup> “The systems NbH(D), TaH(D), VH(D): structures, phase diagrams, morphologies, methods of preparation”, T. Schober and H. Wenzl, in *Hydrogen in Metals II*, edited by G. Alefeld and J. Völkl (Springer-Verlag, New York, 1978) pp. 11-71.
- <sup>5</sup> “The trapping of hydrogen in niobium by nitrogen interstitials”, G. Pfeiffer and H. Wipf, *Journal of Physics F* 6, 167-178 (1976).
- <sup>6</sup> “Local hydrogen vibrations in Nb in the presence of interstitial (N,O) and substitutional (V) impurities”, A. Magerl, J.J. Rush, J.M. Rowe, D. Richter, and H. Wipf, *Physical Review B* 27, 927-934 (1983).
- <sup>7</sup> “Diffusion of hydrogen in metals”, H. Wipf in *Hydrogen in Metals III*, edited by H. Wipf, (Springer-Verlag, New York, 1997) pp. 51-91.
- <sup>8</sup> “Theory of tunneling and diffusion of light interstitials in metal”, H. Grabert and H.R.

---

Schober *ibid* pp. 5-49.

- <sup>9</sup> “Diffusion of hydrogen in transition metal”, H.R. Schober and A.M. Stoneham, *Journal of Less-Common Metals* 172-174, 538-547 (1991).
- <sup>10</sup> “Quantum diffusion of trapped-hydrogen interstitial in Nb: the role of tunnel splitting”, D. Steinbinder, H. Wipf, A.-J. Dianoux, A. Magerl, K. Neumaier, D. Richter, and R. Hemplemann, *Europhysics Letters* 16, 211-216 (1991).
- <sup>11</sup> “Anomalous heat capacities of niobium and tantalum below 1 K”, G.J. Sellers, A.C. Anderson and H.K. Birnbaum, *Physical Review B* 10, 2771-2776 (1974).
- <sup>12</sup> “Nitrogen-hydrogen interstitial pair in niobium as a new system showing atomic tunneling”, C. Morkel, H. Wipf and K. Neumaier, *Physical Review Letters* 40, 947-950 (1978).
- <sup>13</sup> “Tunneling states in amorphous solids”, W.A. Phillips, *Journal of Low Temperature Physics* 7, 351-360 (1972).
- <sup>14</sup> “Diffusion of hydrogen in metals”, J. Völkl and G. Alefeld in *Hydrogen in Metals I*, edited by G. Alefeld and J. Völkl, (Springer-Verlag, New York, 1978) pp. 321-348.
- <sup>15</sup> “Two level systems in glasses”, W.A. Phillips, *Rep. Prog. Phys.* 50, 1657-1708 (1987).
- <sup>16</sup> “Anomalous low –temperature thermal properties of glasses and spin glasses”, P.W. Anderson, B.I. Halperin, and C.W. Varma, *The Philosophical Magazine* 25, 1-9 (1972).
- <sup>17</sup> “On the ultrasonic attenuation in glasses at low temperatures”, J. Jäckle, *Z Physik* 257, 212-223 (1972).
- <sup>18</sup> “Shapes of inhomogeneously broadened resonance lines in solids”, A.M. Stoneham,

---

*Review of Modern Physics* 41, 82-108 (1969).

- <sup>19</sup> “Relaxation of tunneling systems by conduction electrons in a metallic glass”, B. Golding, J.E. Graebner, A.B. Kane, and J.L. Black, *Physical Review Letters* 41, 1487-1491 (1978).
- <sup>20</sup> “Low energy excitations in metallic glasses”, J.L. Black in *Glassy Metals I*, edited by H.-J. Güntherodt and H. Beck (Springer-Verlag, New York, 1981), 167-190.
- <sup>21</sup> “Application of the orthogonality theorem to the motion of a charged particle in metals”, K. Yamada, A. Sakuri and M. Takeshige, *Progress in Theoretical Physics* 70, 73-84 (1983).
- <sup>22</sup> “Relaxation times of tunneling systems in glasses”, B. Golding and J.E. Graebner in *Amorphous Solids, Low-Temperature Solids*, edited by W.A. Phillips, (Springer-Verlag, New York, 1981) pp. 107- 133.
- <sup>23</sup> “Influence of the superconducting state upon the low temperature properties of metallic glasses”, J.L. Black and P. Fulde, *Physical Review Letters* 43, 453- 456 (1979).
- <sup>24</sup> “Elastic effect of structural relaxation in glasses at low temperatures”, J. Jäckle, L. Piché, W. Arnold, and S. Hunklinger, *Journal of Non-Crystalline Solids* 20, 365-391 (1976).
- <sup>25</sup> “Isotope dependence of hydrogen tunneling in niobium”, W. Morr, A Müller, G. Weiss, H. Wipf, and B. Golding, *Physical Review Letters* 63, 2084- 2087 (1989).
- <sup>26</sup> Influence of conduction electrons on tunneling states in amorphous materials”, G. Weiss, *Materials Science and Engineering* A133, 45 –50 (1991).

## III. Experimental

### III. 1. Acoustics

#### *Introduction*

Acoustic methods have been successfully applied to the study of atomic tunneling processes in a wide variety of materials. The choice of experimental technique and the frequency regime of the sound wave are dictated by the propagation characteristics of the material, namely its acoustic attenuation and velocity. The ability to examine specific interactions may depend on the presence of a weak background, or the magnitude of competing acoustic contributions. The experimentalist is often able to operate in a favorable regime by judicious choice of the acoustic frequency and the physical characteristics of the materials under study.

Most investigations of tunneling systems have been performed on three-dimensional, bulk solids. For example, the interaction between phonons and the tunneling of hydrogen in niobium has been studied using many different methods, all of which have used bulk materials. Experiments in the kHz frequency range have been performed by suspending a sample at one end and electrostatically exciting standing wave modes. The elastic energy loss is then measured.<sup>1</sup> Acoustic measurements in the 1 – 100 MHz range have been made by affixing quartz transducers onto the polished faces of bulk single crystal Nb.<sup>2</sup> For higher frequencies, thin film transducers, such as ZnO, have been deposited onto the polished faces of bulk single crystals and the attenuation and velocity of phonons measured.<sup>3</sup>

In this investigation we have studied thin films of Nb deposited from the vapor phase by electron-beam evaporation with a typical film thickness of 200-300 nm. The major reason for examining thin Nb films is the ease with which one can introduce hydrogen into the material as well as the rapidity that it diffuses into the film. By varying the evaporation parameters or exposing the films to gaseous dopants subsequent to evaporation, one can in principle control dopant incorporation. In the case of Nb, one should also be able to influence the superconducting transition temperature  $T_{c,f}$  of the film by control of its microstructure and residual impurities.

In order to measure the change in attenuation and velocity in a thin film with a volume many orders of magnitude smaller than bulk crystals, we employed surface acoustic waves. Surface acoustic waves, or SAWs, are modes that propagate parallel to the surface of the substrate but decay exponentially with a decay length on the order of an acoustic wavelength. At an acoustic wavelength of 6  $\mu\text{m}$ , a film with a 300 nm thickness will correspond to an interaction volume of roughly 5%, there is nevertheless sufficient sensitivity to measure changes in the acoustic properties of less than 0.1%. Since the attenuation of phonons is generally proportional to the square of the phonon frequency, the sensitivity of the experiment is enhanced by using SAW with a resonant frequency in the 0.1 to 1 GHz range.

SAW experiments to probe the tunneling of hydrogen in niobium have been carried out at temperatures between 0.1 and 10 K. It was necessary to go to such low temperatures for several reasons. First of all, extraneous or background contributions to acoustic attenuation and velocity are substantially reduced at low temperatures. Second, relaxation interactions are enhanced when defect relaxation rates are in the same range as

the acoustic frequencies. For instance we are able to observe a relaxational peak which occurs when the frequency of the phonons matches the relaxation rate of the tunneling hydrogen atoms. Third, since the energy of a GHz phonon corresponds to a thermal energy of about 0.1 K, resonant features will only come into play when the temperature is less than 1 K. Finally, since Nb is a superconductor we are interested in examining the role that pairing interactions among conduction electrons play in influencing the tunneling dynamics of the hydrogen impurities. By descending to temperatures well below  $T_{c,f}$  or by applying magnetic fields greater than  $H_{c2}$  we are able to modulate the electronic state of the metal and its coupling to the tunneling atoms.

*Basic concepts of surface acoustic waves.*

Before delving into the specific nature of the surface acoustic waves used in our experiments, it is necessary to introduce a few basic concepts. The surface acoustic waves used in our experiments were a variant of Rayleigh waves. Rayleigh waves are a surface wave solution for an isotropic medium. They are a sum of partial longitudinal and shear waves which propagate in the  $x_1$  direction with wavefronts parallel to the  $x_2$  axis as shown in Figure 3.1.

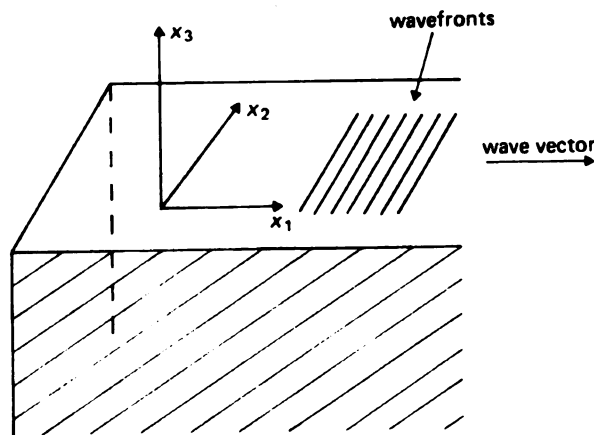


Figure 3.1. Rayleigh wavefronts, from Morgan<sup>5</sup>.

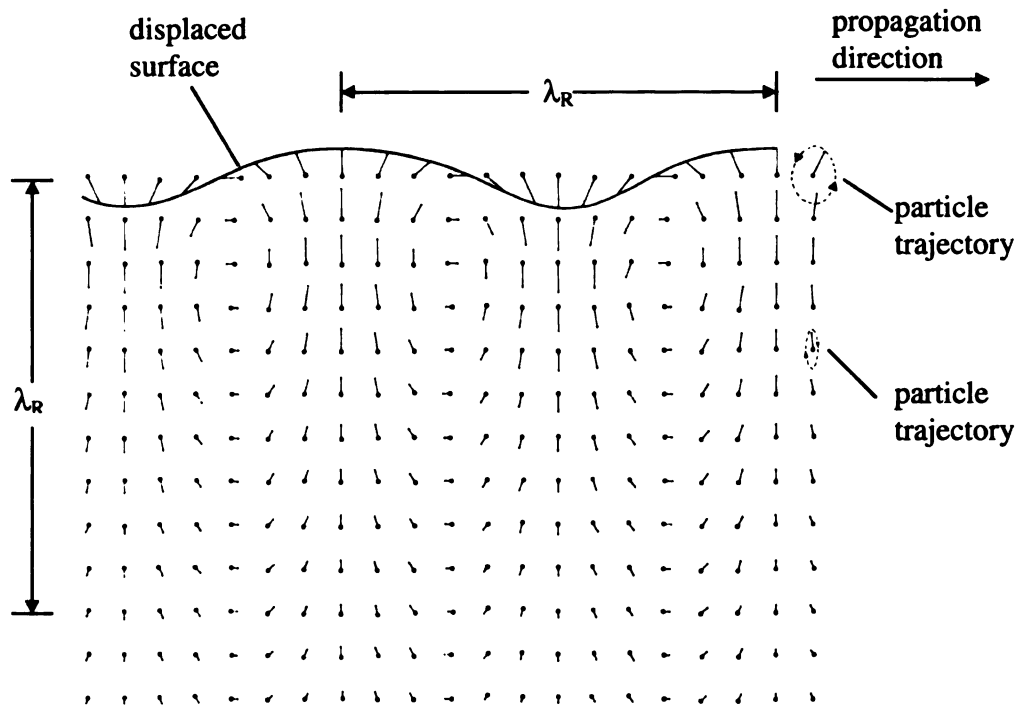


Figure 3.2. The motion of the atoms in a Rayleigh wave. The dots are the equilibrium position of the atoms and the lines are their displaced positions. The dotted circles are the particle trajectories (from Morgan).<sup>5</sup>

All atom motion is confined to the  $x_1$ - $x_3$ , sagittal, plane. The atoms near the surface move in a retrograde ellipse while those below move in a prograde direction. As shown in Figure 3.2 the Rayleigh wave decays exponentially with depth and has a perturbation depth of about a wavelength. The velocity of a Rayleigh wave velocity is slower than both the bulk transverse and shear velocities.

#### *Surface acoustic waves on a piezoelectric*

The substrates used in the experiments were  $\text{LiNbO}_3$ , an anisotropic piezoelectric crystal. A piezoelectric is a material for which there is a linear coupling between an applied electric field and strain. This coupling is described by the coupled equations

$$\begin{aligned} T_{ij} &= c_{ijkl}^E S_{kl} - e_{kij} E_k \\ D_i &= \epsilon_{ij}^S E_j + e_{ijk} S_{jk} \end{aligned} \quad (3.1)$$

where  $T$  is the stress tensor,  $c$  is the elastic constant or stiffness tensor,  $S$  is the strain tensor,  $S_{ij} = \frac{1}{2} \left( \frac{\partial u_i}{\partial x_j} + \frac{\partial u_j}{\partial x_i} \right)$ ,  $u_i$  is the displacement from the spatial coordinate  $x_i$ ,  $e$  is the piezoelectric constant,  $E$  is the electric field,  $D$  is the electric displacement and  $\epsilon$  is dielectric tensor.<sup>4</sup>

A strain electrically polarizes the crystal and thus generates an electric field. A solution to the surface wave equation for an anisotropic piezoelectric substrate such as  $\text{LiNbO}_3$  is the piezoelectric Rayleigh wave.<sup>5</sup> This wave is very similar to the isotropic Rayleigh wave in that the propagation vector is parallel or nearly parallel to the sagittal plane. However, the wave is now accompanied by an electric field and its velocity is dependent upon the angle between the propagation direction and the crystal axes. The electric field extends above the surface of the substrate and can interact with overlayers.

### III.1.i Interactions between thin films and surface acoustic waves.

#### *Electron phonon interaction*

For a piezoelectric substrate, the electromechanical coupling constant,  $\kappa^2$ , gives a measure of the coupling between an electric field and a specific strain. When a metal film is deposited on the surface of a substrate, the surface becomes an equipotential and the electric field is shorted. The  $\kappa^2$  measures the fraction of the total potential energy of the SAW that is used to produce the electric field accompanying the SAW. A larger  $\kappa^2$  corresponds to a larger coupling between the electric and acoustic fields and represents a

more “efficient” transducer. Typically this coupling is on the order of a few percent or less. The electromagnetic coupling is related to the change in velocity upon deposition of a massless infinitely conducting metallic film by the expression,<sup>6</sup>

$$\kappa^2 = -2 \left( \frac{v_{\text{metal}} - v_o}{v_o} \right) \equiv 2 \frac{\Delta v}{v} \quad (3.2)$$

Snider et al.<sup>7</sup> modeled the change in the velocity and attenuation upon deposition of a thin metallic film on top of a piezoelectric. A metallic film can perturb the acoustic properties of a SAW by both its mass and its electrical characteristics. Their assumptions were that the metal was homogenous, the free electron model was applicable and the electron mean free path was much smaller than the acoustic wavelength. By imposing boundary conditions on the surface wave equations, they derived a 6x6 matrix from the partial wave equations with a determinant equal to zero. From this determinant, the Rayleigh velocity and attenuation due to the film can be derived. This determinant however, is quite difficult to solve.

By treating the film as a velocity perturbation, Farnell<sup>4</sup> calculated the change in velocity due to the mass of the film as well as its electrical characteristic. The change in velocity due to the mass is given by

$$\left( \frac{\Delta v}{v} \right)_{\text{mass}} = \frac{\omega}{4P_1} qh \left[ \left( \frac{c_{11}^2 - c_{12}^2}{c_{11}} - \rho v^2 \right) |u_1(0)|^2 + (c_{44} - \rho v^2) |u_2(0)|^2 - \rho v^2 |u_3(0)|^2 \right] \quad (3.3)$$

where  $\omega$  is the frequency of the surface wave,  $v$  the unperturbed velocity,  $q = \omega/v$ ,  $u_i$  is the displacement in the direction  $i$  ( $u_1$  is the displacement along the propagation axis and  $u_3$  is the displacement along the axis perpendicular to the surface.),  $c_{ij}$  are the elastic

constants of the layer material,  $h$  is the thickness of the film,  $\rho$  is the density of the film, and  $P_1$  is the power/unit width carried in the surface wave. If the propagation direction is a pure mode direction, i.e. the energy flow is parallel to the wavevector, only  $P_1$  is non zero. Similarly the change in velocity due to the electrical shorting can be calculated,

$$\left(\frac{\Delta v}{v}\right)_{\text{elec}} = -(\epsilon_0 + \epsilon)|\phi(0)|^2 \frac{\omega}{4P_1} = \frac{\kappa^2}{2} \quad (3.4)$$

where  $\epsilon_0$  is the dielectric constant in a vacuum,  $\epsilon$  is the dielectric constant of the substrate for the substrate at constant stress, and  $\phi(0)$  is the electrical potential at the surface of the substrate.

Levy et al.<sup>8</sup> developed an equation for the attenuation due to the electron-phonon interaction in a thin film in which the attenuation of sound in a bulk material is scaled by a factor of  $(qh)F(v)$ .  $F(v)$  is a complicated function of Poisson's ratio.<sup>9</sup> The thin film attenuation is then given by

$$\alpha_{\text{SAW}} = \frac{Nm v_F^2 \omega^2 \tau_e}{\rho v_S^3} qhF(v) \quad (3.5)$$

where  $N$  is density of electrons,  $m$  is the free electron mass,  $v_F$  is the Fermi velocity of the electrons,  $\tau_e$  is the electron relaxation time, and  $v_S$  is the SAW velocity under the film. This equation can also be used to determine the mean free path of the electrons,  $l_e = v_F \tau_e$ , if the attenuation is known.

Levy<sup>10</sup> also showed that the BCS equation for the change in the phonon attenuation due to the electron-phonon interaction for a superconducting bulk metal describes the attenuation of a SAW traveling through a superconducting film. The ratio of the normal to the superconducting attenuation is given by,

$$\frac{\alpha_s}{\alpha_n} = \frac{2}{e^{\Delta(T)/k_B T} + 1} \quad (3.6)$$

where  $\alpha_n$  is the normal state attenuation,  $\alpha_s$  is the superconducting attenuation,  $\Delta(T)$  is the temperature dependent BCS energy gap, and  $k_B$  is Boltzman's constant. This change in attenuation upon our sample becoming superconducting will have to be subtracted from effects due to the tunneling systems.

### *Acoustoelectric effect*

The attenuation and velocity of SAW traveling through metallic films are also affected by the acoustoelectric effect. This effect is due to the fact that the polarization of the piezoelectric causes image charges to be formed in the metallic overlayer.<sup>11</sup> These image charges move with the SAW velocity and produce energy dissipation. The amount of dissipation is dependent on the conductivity of the film. An infinitely conducting film (superconductor) will result in zero energy dissipation. An insulator, zero conductivity, also results in zero energy dissipation as no image charges are produced. The attenuation and change in velocity due to the acoustoelectric effect are given by

$$\alpha = \frac{\kappa^2}{v_s} \frac{\omega^2 \tau}{1 + \omega^2 \tau^2} \quad (3.7)$$

$$\frac{\Delta v}{v} = -\frac{\kappa^2}{2} \frac{1}{1 + \omega^2 \tau^2} \quad (3.8)$$

where  $\omega\tau = v_s(\epsilon_0 + \epsilon)/\sigma_{\square}$  for films with thickness less than  $\lambda/2\pi$ ,  $\epsilon$  is the dielectric permittivity of the substrate, and  $\sigma_{\square}$  is the sheet conductivity of the film.<sup>12</sup> For YZ cut  $\text{LiNbO}_3$  covered by a film with a resistivity of  $12 \mu\Omega\text{-cm}$ ,  $\tau \sim 10^{-15}$  s.

### III.1.ii. Design of Transducers

As mentioned in the introduction of this chapter, we wished to send GHz surface acoustic waves through thin films. To this end we fabricated GHz surface acoustic wave devices.

*A method for generating and receiving SAWs.*

To generate surface acoustic waves a metallic grating is deposited on a piezoelectric substrate. This grating acts as a transducer converting electromagnetic signals to acoustic and vice versa. A potential difference between two fingers of the grating will cause the surface of the piezoelectric to contract or expand depending upon the sign of the difference. Alternating the sign of the potential difference across successive pairs of fingers will set up a standing wave on the surface. Varying the potential difference with a frequency,  $f = v / \lambda$  where  $v$  is the substrate velocity and  $\lambda$  is the periodicity of the fingers will send a surface acoustic wave skimming across the surface with a wavelength of  $\lambda$ . In other words, for a static electric field the wave vector is equal to zero. By conservation of momentum, two counterpropagating SAWs must be created with  $k_1 = -k_2$ , where  $k = 2\pi/\lambda$  and  $\lambda$  is equal to the periodicity of the electric field. The electric field accompanying the SAW can be “picked up” by a grating with a periodicity equal to  $\lambda$ .

Figure 3.3 shows a diagram of a metallic grating which could be used to generate or detect a SAW. Such gratings are often called transducers. The transducer pattern is bi-directional in that it generates waves to both the left and the right, as well as can receive from both directions. The transducer’s fingers are a double electrode pattern.

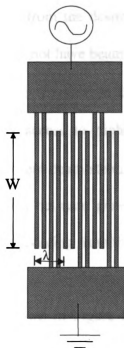
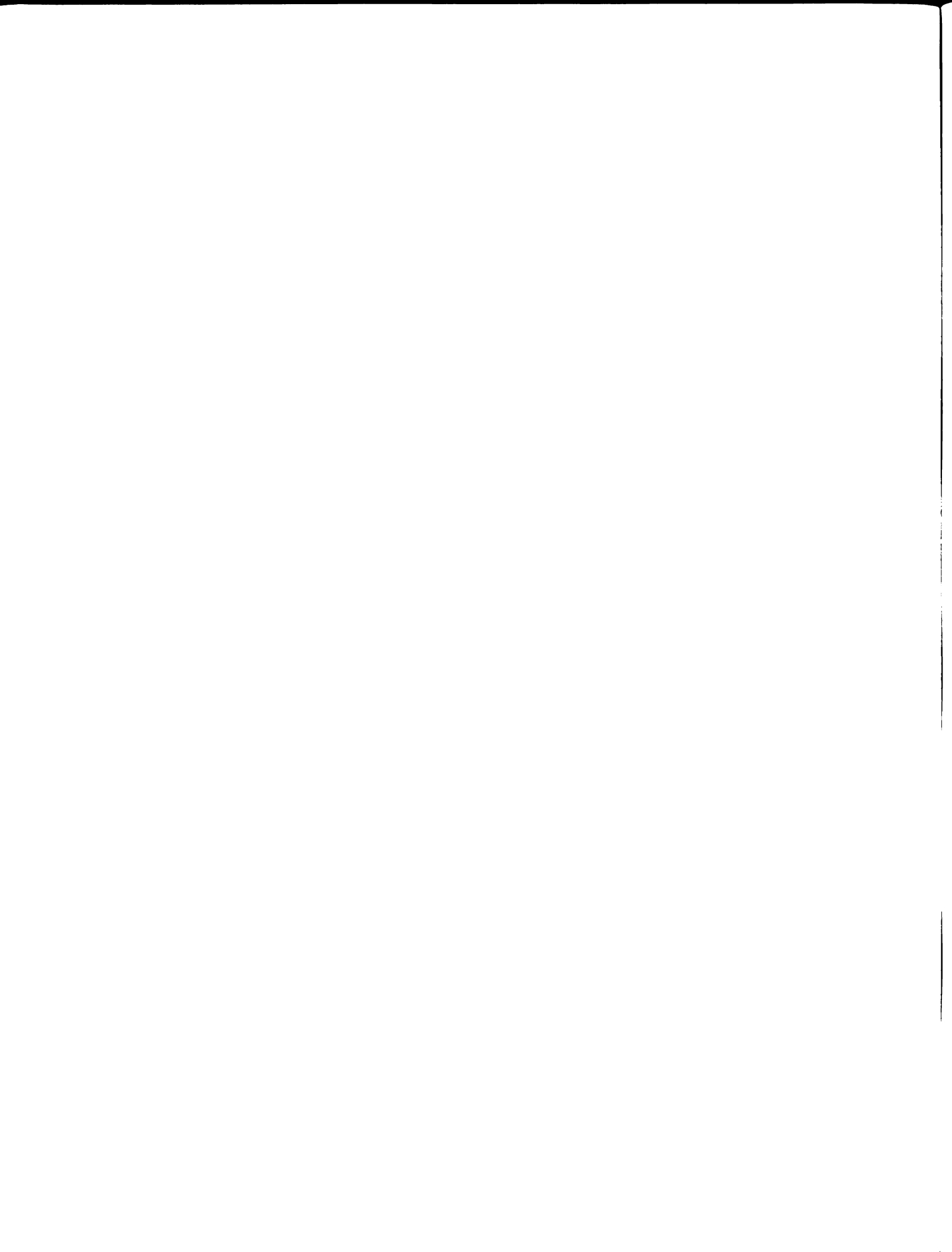


Figure 3.3. Schematic of a double electrode transducer.  $\lambda$  is the periodicity or wavelength,  $W$  is the aperture, the number of repetitions,  $N_p$ , is 3. The ground and ac electrical connections are shown.

#### *Properties of the $128^\circ$ rotated cut of $\text{LiNbO}_3$*

Our piezoelectric substrate was  $128^\circ$  rotated Y-cut, X-propagating  $\text{LiNbO}_3$ . This substrate and cut were chosen for several reasons.  $\text{LiNbO}_3$  has high coupling between surface acoustic waves and the piezoelectric substrate,  $\Delta v/v = 2.72\%$ . In contrast, most piezoelectrics have electromechanical coupling constants of less than one percent. The  $128^\circ$  cut also has essentially nonexistent coupling to bulk waves thus eliminating spurious signals from bulk waves. In addition, it has a high velocity for a piezoelectric,  $3.992 \times 10^3$  m/s. Finally, in most piezoelectrics, the electrodes must be carefully aligned on the crystal or else the power flow of the surface wave will not be parallel to its



wavevector, i.e. the wave will deviate from the desired propagation direction. This is called beam steering. The  $128^\circ$  cut does not have beam steering.<sup>13</sup>

The last two characteristics increase the ease in fabrication of transducers. Since  $f = v / \lambda$ , the high velocity allows access to higher frequencies without requiring excessively narrow electrodes. The absent beam steering allows for slight misalignment of the electrodes without loss of signal between generating and receiving transducers. However, the velocity decreases upon deviating from the x axis.

#### *Design parameters for our transducers*

The double electrode pattern as shown in Figure 3.3 was used for our transducers because it causes reflections due to piezoelectric stiffening from neighboring electrodes to destructively interfere.<sup>14</sup> The strength of these reflections is proportional to  $\kappa^2$  and can distort the response of the transducer. With lithium niobate the reflections are about 20 dB below the incident power with only 10 single electrodes.<sup>15</sup> Thus although the double electrode pattern requires narrow fingers which are difficult to fabricate, they are necessary in order to reduce the internal reflections which complicate the transducer's response curve.

The transducers were designed for a fundamental frequency of 733 MHz. This required  $\lambda = 5.44 \mu\text{m}$  and thus transducer fingers and gaps of  $0.68 \mu\text{m}$  with the double electrode configuration. By designing the transducer to have a radiative resistance of  $50 \Omega$  we hoped to further minimize the insertion loss of the transducers. If a transducer has a radiative resistance of  $50 \Omega$  and is put in series with an inductor,<sup>1</sup> the loss in theory can be minimized to 3 dB. The radiative resistance is dependent only upon substrate

characteristics and the ratio of  $W / \lambda_c$ . For double electrodes on YZ lithium niobate, a resistance of  $50 \Omega$  occurs for  $W / \lambda_c = 60$ .<sup>16</sup> Therefore, our transducers had an aperture,  $W$ , of  $320 \mu\text{m}$ . The parameters for  $128^\circ$  cut  $\text{LiNbO}_3$  differ by 2.5% from those of the YZ and lead to a predicted a radiative resistance of  $49.7 \Omega$ . One other design characteristic which can improve the efficiency of a transducer is to make sure that the fingers are the same width as the gap.<sup>17</sup>

Since we planned on using square pulses as narrow as 100 nsec, it was necessary to have to have a bandwidth on the order of 60 MHz. If the number of electrode periods,  $N_p$ , on lithium niobate is greater than 4, the acoustic bandwidth at 1.5 dB is given by,<sup>18</sup>

$$\left( \frac{\Delta\omega}{\omega} \right)_{\text{unmatched}} = \frac{0.638}{N_p} \quad (3.9)$$

$$\left( \frac{\Delta\omega}{\omega} \right)_{\text{matched}} = \frac{1.14}{N_p} \quad (3.10)$$

Our patterns had  $N_p = 10$  which results in a predicted matched (unmatched) bandwidth of 83 MHz (46 MHz) at 733 MHz. The large number of fingers incorporated some redundancy into the pattern so that a few fingers could be flawed without having much effect on the transducer's performance.

Since the velocity of a SAW is affected by overlayers, including transducer fingers, transducers are typically fabricated from aluminum since its sound velocity is a good match to the lithium niobate. Nevertheless, we used gold electrodes in order to avoid complicating our low temperature data with features due to superconducting electrodes. Gold has a Rayleigh speed of  $1172 \text{ m/s}$ ,<sup>19</sup> much less than that of  $\text{LiNbO}_3$ . By keeping our

electrodes thin, however, we found that there was very little difference in the insertion loss between Al and Au electrodes.

## III.2 Electron beam lithography

### *General overview of electron beam lithography*

Since it was not possible to resolve three transducers with 0.68  $\mu\text{m}$  fingers using the contact photolithography equipment available, electron beam lithography was used to fabricate the transducers. The general outline of this lithographic process is outlined in Figure 3.4. The first step in electron beam lithography is to spin a polymer onto a substrate. This polymer, or resist, undergoes a structural change when exposed to electrons. Polymethyl methacrylate, PMMA, the resist used in our lithography, has crosslinks which are broken by electrons. The electron beam of a scanning electron microscope, SEM, is used to expose the resist. The exposed areas are then removed with a developer. After development metal is deposited onto the substrate and resist. The unexposed resist (and the metal on top of it) is removed in a process called lift off. Metal is then left in the area that was exposed by the electron beam.

### *Electron beam lithography of transducers on $\text{LiNbO}_3$ .*

$\text{LiNbO}_3$  is a difficult material to process since it is pyroelectric as well as piezoelectric. A change in the temperature of the crystal leads to electrical polarization. Therefore in heating or cooling, temperature gradients lead to an inhomogeneous charge distribution causing the substrate to crack or shatter. In general, the rate of temperature change must be less than 2 K / min. Care must be taken in cleaning the substrates prior to the lithography since a single dust particle may destroy an electrode. Contaminants will

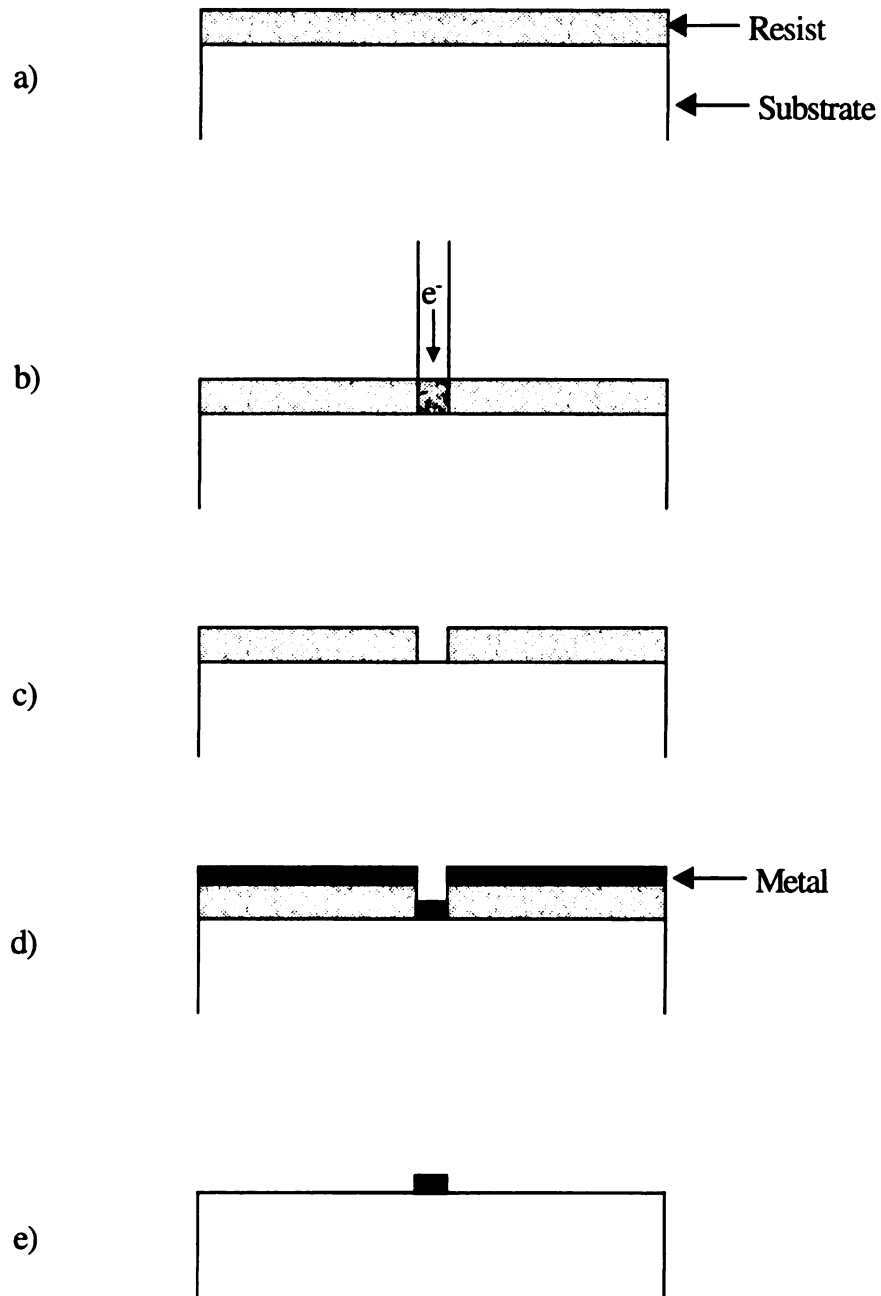


Figure 3.4. Standard process of electron beam lithography. a) resist  is spun onto the substrate , b) exposure by electrons, c) development, d) metal  is deposited, and e) lift off.

also cause poor adhesion of the PMMA or metal which will result in warped or wiggling fingers. Keeping  $\text{LiNbO}_3$  clean is a challenge, as there is usually an electrical charge present on the substrate which causes it to act as a “dust magnet”. This makes it necessary to do all processing during transducer fabrication and sample deposition in a clean environment.

When the  $2 \times 3 \text{ cm}^2$  substrates were cut from the 3”  $\text{LiNbO}_3$  wafer, care was taken to make sure than the cuts were parallel to the flats indicating the crystal axis’ of the wafer. The substrates were cut with wire saw using a 0.005” stainless wire and a slurry of 600 grit boron carbide and water. The wire saw did tend to wander, cutting a slot on the order of 0.01- 0.02”. In general, two perpendicular sides were less than 0.3 degrees from 90°.

The first step of the cleaning procedure consisted of removing protective layers of resist by soaking and ultrasounding in acetone. (Before cutting, substrates were coated with resist to protect the surface.) The substrate was then “scrubbed” with a cotton swab while it rested on the bottom of a beaker of acetone in order to remove any stubborn deposits of resist. After scrubbing, the substrates were rinsed with methanol and deionized water, DI, and inspected under a microscope. Once clean of resist the substrates were put in a beaker of 3:1:1 (DI :  $\text{NH}_4\text{OH}$  :  $\text{H}_2\text{O}_2$ ) degreaser which was then heated up to 70° C at 2 - 3° C / min. The substrates were kept at 65 - 75° C for 10 min and then were transferred into warmed DI. This degreaser does remove some PMMA as well as other organics so it can be used iteratively with the acetone scrub. Once the DI had cooled the substrates were rinsed with running DI and then ultrasounded in 2-propanol. Finally, the substrates were rinsed with 2-propanol, dried with  $\text{N}_2$  gas and

inspected. Since lithium niobate is quite brittle, polypropylene beakers were used whenever possible to minimize chipping of the substrate edges.

After cleaning, the substrates were spun with 4% PMMA at 4000 rpm for 30 sec. They were then placed into clean glass petri dishes for baking. Before placement in the oven, the petri dishes were loosely wrapped with aluminum foil in order to keep the dirt from the oven off the substrates. Each dish contained both test and real substrates as the electron beam exposure varied with position in the oven. The PMMA was baked in a programmable digital oven in which the temperature was ramped up to 150° C at 60° C / hour. Once the temperature had reached 150°, the temperature was ramped down to room temperature at the same rate.

To write the transducers with equal finger and gap width, the electron beam had to be focused within 1 mm of the writing location of a transducer. Therefore, dots of silver paint were carefully placed on the cooled resist near the planned location of each transducer. Since transducer fingers could not be written on top of silver paint, it was important to make the dots as small as possible and to avoid splattering the paint. If the environment was excessively dry, the LiNbO<sub>3</sub> had to be grounded in order to remove built up static charge. Otherwise the silver paint would be pulled off the applicator and spread across the substrate. An ethanol based paint was used since it would be removed by the developing process.

Lithium niobate is an insulator, and thus charges when an electron beam is incident upon it. Therefore, a 90 Å film of Al was deposited on top of the resist and silver paint to reduce the charging. This film was deposited in a thermal evaporator at pressures less than  $6 \times 10^{-6}$  torr and rates greater than 2 Å/sec. After deposition of the aluminum layer,

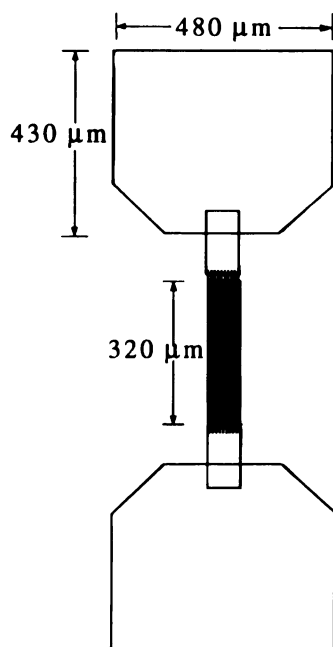


**Figure 3.5.** The pattern used to write the transducers. Irregularities of the fingers are due to the resolution of the printer and are not part of the pattern.

the substrates were ready for exposure in a JEOL 840 scanning electron microscope. The beam was computer controlled using the Nabity Pattern Generation System. Figure 3.5 is the pattern used to write the transducers. Due to the scattering of the electron beam by the substrate, this pattern had the electron beam write fingers with a width of  $0.605\ \mu\text{m}$  and gaps of  $0.755\ \mu\text{m}$ . This resulted in exposing fingers and gaps of the same width. The program also had the transducers rotated  $8.75^\circ$  to compensate for the fact that the x-y axis of the electron beam's scan is  $8.75^\circ$  off from the x-y axis of the translation stage when the stage is set at a working distance of 10 mm.

Our devices consisted of three transducers fabricated in a row along the propagation axis of the lithium niobate. As shown in Figure 3.6, they were separated by 6 mm. The center transducer was the generator while the outer transducers were receivers.

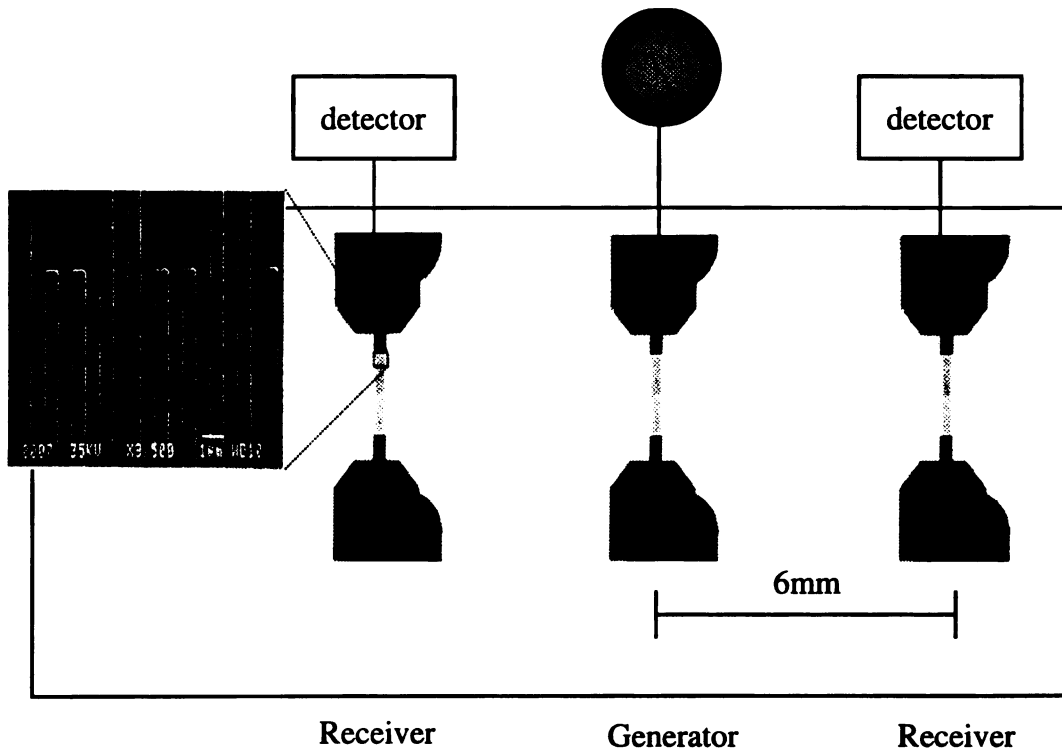


Figure 3.6. Schematic of the substrates with an inset SEM picture of the electrodes.

Before exposure the SEM current must be stable as it took three hours to write one set of three transducers and it was not possible to check the current during this time. While the beam stabilized, the substrate was aligned in the SEM. In order to align the x-y micrometers of the SEM to the crystal axis of the substrate, the stage was translated along an edge of the substrate at the same magnification at which the fingers were written. The rotation of the stage was adjusted until the edge remained in the center of the screen during translation. The cleanest edge, implying most likely to be along a crystal axis, was chosen for alignment.

Once the beam current had stabilized, the three transducers were written in succession. Each transducer was written after focusing on a silver paint dot within 1 mm of the writing location. To avoid exposing the resist in the acoustic pathway, the beam was

“blanked”, or covered, as it was moved between writing and focusing spots. Due to backlash in the x translation micrometer all motion along the x axis was in one direction.

After exposure, the aluminum layer was removed by agitating the substrate in a weak NaOH solution (1.25 g NaOH / 200 ml DI) for 80 sec. The substrate was then rinsed with running DI and dried with N<sub>2</sub> gas. The PMMA was developed in a 1:3 (4-methyl 2-pentanone: 2-propanol) solution for 70 sec. The development was stopped with 30 second agitation in 2-propanol and the substrate was then rinsed for 30 seconds with DI. After development, the resist was etched with an oxygen plasma for 30 seconds in order to remove any residual PMMA in the exposed regions.

The substrate was then metallized with 100 Å Ti and 500 Å Au in a thermal evaporator. The substrate was on a rotatable sample holder so that both evaporations could be done with the metal being deposited at normal incidence. Lift off was accomplished by soaking the substrate in acetone for a couple of hours. The substrate was then rinsed with methanol and DI and dried with nitrogen gas. The pads of the transducers as fabricated by lithography were only 0.48 x 0.43 mm. Thus for ease in making electrical contacts, larger pads were deposited which overlapped the lithographically produced pads. These pads were deposited through a mechanical mask that was held slightly above the substrate in order to avoid scratching the substrate or the transducers. These pads were composed of 100 Å Ti and 3000 – 5000 Å Au again evaporated at normal incidence.

### III.3 Characterization of transducers

To evaluate the transducers after fabrication and before Nb deposition, a room temperature sample holder was designed. Since the devices had to remain clean for sample deposition, we used small gold bellows to make electrical contact to the pads of the transducers. These bellows were soldered onto the center conductor of 0.085" semi rigid coaxial cable and lowered onto the pads of the signal side of the transducers. Bellows were soldered onto brass plugs and lowered onto the other side for grounding of the transducers. A side view of the sample holder is shown in Figure 3.7.

Because these contacts were just light pressure contacts, it was difficult to get exact results of the acoustic characteristics of a SAW device from the tester. However, one could test the general properties of the transducers. Using this tester, we measured the delay time of the channels, the velocity of the SAW, the insertion loss and the resonance peak of the transducers.

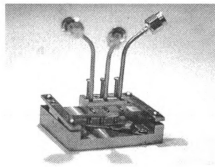


Figure 3.7. A side view of the room temperature sample holder. The short plugs in the back row are the ground contacts while the coaxial lines in the front row carry the ac signal.

### III.3.i Saw device characteristics

The device used in Run 4.16, the run from which most of the data presented in this thesis are from, was typical of devices fabricated by the above method. This device had two channels, labeled A and C. As shown in Figure 3.8, the resonance curves of the device were not featureless. However, it is possible to extract from them a resonant frequency, bandwidth (width at which the signal has dropped by 3 dB) and loss at the resonant frequency. The A channel had a resonant frequency of  $705 \pm 2$  MHz, a bandwidth of  $36 \pm 2$  MHz and a loss of  $20.8 \pm 0.5$  dB. The C channel had a resonant frequency of  $695 \pm 3$  MHz, a bandwidth of  $34 \pm 2$  MHz and a loss of  $19.8 \pm 0.5$  dB.

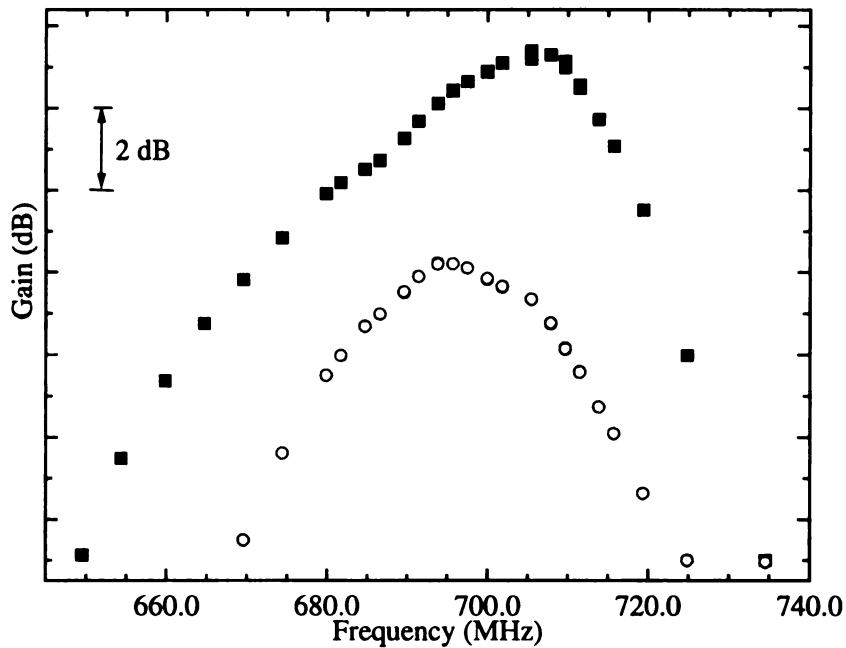


Figure 3.8. The resonance curves of the two channels as measured in the room temperature tester. ■ is the A channel and ○ is the C channel. The curves have been offset for clarity.

*Comparison to designed values for pitch and velocity of 128 Y-Cut LiNbO<sub>3</sub>*

All of the SAW devices manufactured using the method outlined in III.2 had resonant frequencies of about 700 MHz. This resonant frequency is lower than the 733 MHz for which the transducers were designed, probably due to miscalibration of the SEM's magnification. A transducer was profiled using an AFM and it was found to have a pitch, finger plus gap width, of  $1.40 \pm 0.02 \mu\text{m}$ . The designed value for the pitch was  $1.36 \mu\text{m}$ . Taking the measured pitch as  $\lambda/4$  and the frequency as  $700 \pm 5 \text{ MHz}$ , the velocity of the LiNbO<sub>3</sub> is found to be  $3920 \pm 70 \text{ m/s}$ . The value for 128° Y- cut LiNbO<sub>3</sub> is 3992 m/s which is just outside of the uncertainty. This would indicate that the alignment of the transducers' electrodes was quite close to perpendicular to the propagation, x, axis. The velocity will be discussed further in Section III.4.iv.

*Comparison of bandwidth and insertion loss to design and between sample holders*

The 3 dB bandwidth of a transducer pair should be the same as the 1.5 dB bandwidth of a single transducer. The predicted unmatched transducer bandwidth for our devices was 46 MHz and the predicted matched bandwidth was 83 MHz. The measured widths in the room temperature holder are below both of these values. Since the two channels have different resonant frequencies, it is very likely that the resonance frequencies for the generator and receiver transducers are not identical. This would result in a narrower bandwidth. This narrow width is also a good indication that the transducers are not impedance matched to their load. This is probably a combination of the transducer not being exactly  $50 \Omega$  and the electrical contacts not being  $50 \Omega$ . The mismatch of the electrical contacts in the room temperature sample holder is not too surprising as the

contacts to the transducers are just pressure contacts through a bellows. This bandwidth will be discussed further in III.4.iv.

### III.4 Niobium film deposition

#### III.4.i Description of UHV system

Niobium films were deposited in an Ultra High Vacuum (UHV) chamber by electron beam evaporation. Figure 3.9 is a schematic of the chamber. A typical base pressure in the main chamber is  $5 \times 10^{-10}$  torr. The main chamber is pumped by an ion pump and a titanium sublimation pump. A turbo pump, backed by an oil free diaphragm rough pump

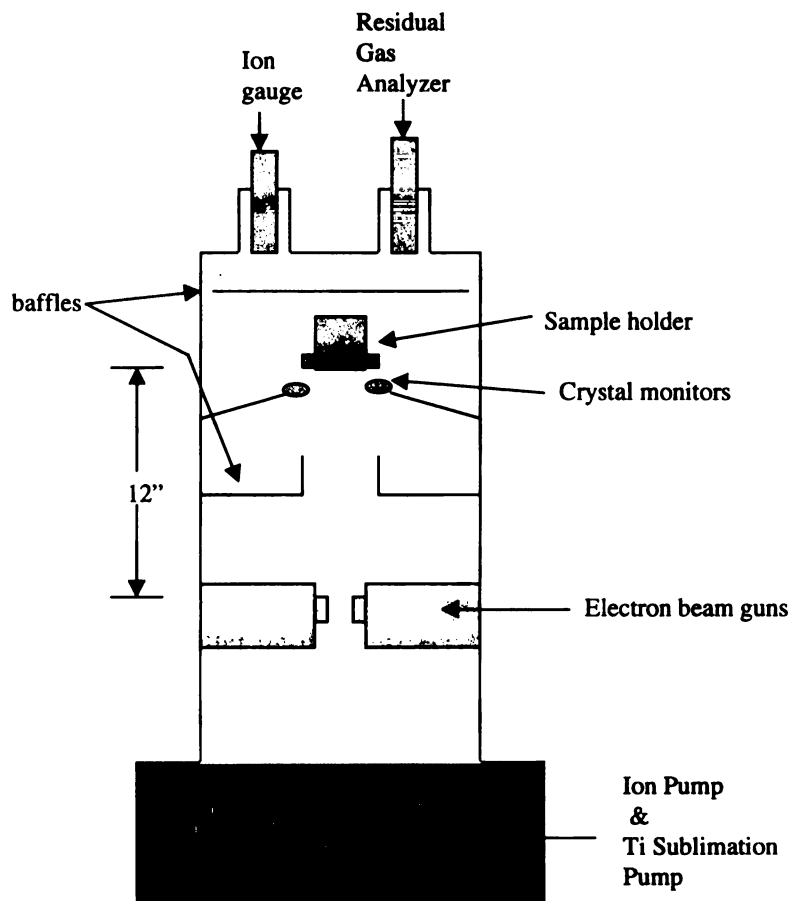


Figure 3.9. A schematic of the UHV chamber in which the Nb was evaporated on to the  $\text{LiNbO}_3$ . 12" is the distance between the Nb charge and the substrate.

is used to evacuate the load lock to  $10^{-7}$  torr.

The main chamber contains a mass spectrometer residual gas analyzer, RGA, which detects contaminants down to  $10^{-13}$  torr partial pressure. It is not useful for quantitatively determining the H concentration in the chamber as hydrogen is generated within the spectrometer from hydrogen containing species. If the system had been closed for a day, typical contaminants detected were  $H_2O$ , H,  $CO_2$ , and CO/  $N_2$  (these two have the same main peak and very small minor peaks and thus are difficult to discriminate between) usually with partial pressures less than  $5 \times 10^{-10}$  torr. If the chamber had been open to the load lock these partial pressures were an order of magnitude greater. There are two electron beam evaporation guns in the main chamber. A maximum total current of 660 mA can be applied to the two guns. The guns are water-cooled and a variety of pocket liners are used in the copper hearth. Typically an insulating liner is used to thermally isolate the charge and thus reduce the power necessary for evaporation. Since we were unable to find an insulating liner which did not react with Nb, we used a copper liner. In order to maximize the stability of the evaporation rate, the electron beam was swept in a circular pattern over the surface of the niobium charge. A crystal monitor located near the sample puck controlled the current to the gun. To minimize contamination, the sample was covered by a shutter until a satisfactory rate was reached. The sample puck had thermocouples on the back of its face and on the heater block for measuring the temperature.

#### III.4.ii Evaporation of niobium films

Nb films were evaporated through 0.01" stainless steel mechanical masks. The masks were held slightly off the substrate in order to protect the lithium niobate and the

fabricated transducers. This also served to insure that the edges of the niobium were tapered and thus minimized SAW reflections from the Nb. The mask contained square holes for evaporating niobium in the acoustic pathways in between the transducers. These holes were much wider than the aperture of the transducer so that edge effects due to the film's sides parallel to the propagation axis could be discounted. In addition, a six-probe pattern for resistance measurements, which will be discussed in III.4.iii, was deposited.

The high melting temperature and low vapor pressure of niobium restricted the rate at which the niobium could be evaporated. A current of around 500 mA was needed for a rate of 3 Å/sec, with a stability of 0.1 Å/sec. At 4 Å/sec the rate was much less stable. During evaporation of the samples the pressure in the system stabilized near  $4 \times 10^{-8}$  torr. The major contaminants during evaporation were hydrogen, methane (CH<sub>4</sub>) and CO / N<sub>2</sub>. During evaporation, the temperature on the back of the sample puck rose to 43° C suggesting that the LiNbO<sub>3</sub> was probably not stressed during the deposition. The sample was allowed to cool to 36° C before being transferred into the load lock, which was then vented to atmospheric pressure with nitrogen gas. The sample was in the UHV chamber and load lock for a total of about 1.5 hours before being removed. After removal, the sample was inspected, put in the Kevinox sample holder, and wires connected between the holder and the substrate. The sample was then put into the dilution refrigerator which was evacuated immediately to reduce the exposure to air. One can assume that upon exposure to air an oxide layer forms on Nb which acts as an hydrogen diffusion barrier.<sup>20</sup> Typical air exposure was about 5 hours.

### III.4.iii Characterization of films

#### *Measuring the resistance and resistivity.*

The niobium films were characterized by measuring the resistivity ratio, the superconducting transition temperature and the transition width. The resistance of the Nb film with the geometry shown in Figure 3.10. F and C are current leads, A, B, D, and E are two voltage leads and two spare leads. This film was deposited onto the lithium niobate concurrently with the deposition of the Nb film between the transducers. The dimensions shown in Figure 3.10 were measured with an Olympus BH-2 microscope and were used in computing the number of squares for the resistivity calculations. The number of squares is  $11.8 \pm 0.3$ .

The resistance of the sample was measured using the circuit shown in Figure 3.11. The current to the sample was  $5.40 \pm 0.025 \mu\text{A}$ . The thickness of the film was measured using a dektak surface profiler. Two films were studied in two separate runs, Run 4.15 and Run 4.16. In Run 4.16, the run upon most of this thesis is based, the film was  $2915 \pm 75 \text{ \AA}$  thick. The room temperature resistivity was  $30.0 \pm 1 \mu\Omega\text{-cm}$ , the resistivity ratio,

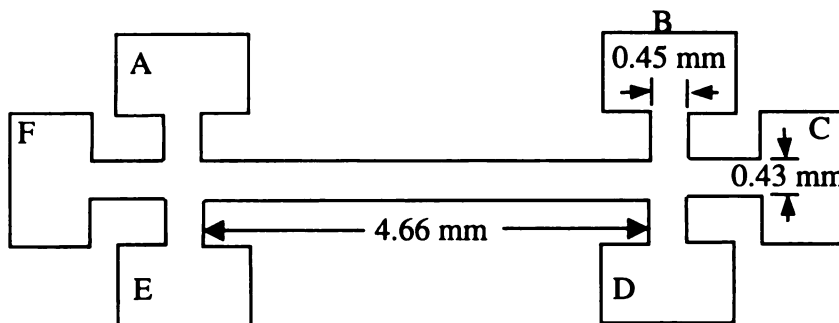


Figure 3.10. The pattern used for resistance measurements.

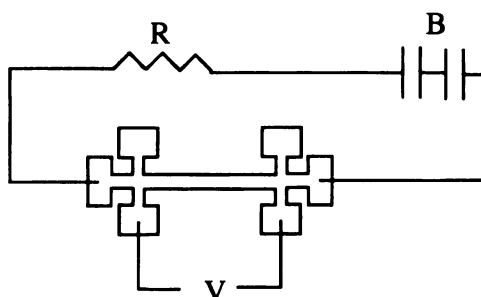


Figure 3.11. Resistance measuring circuit. R is a 0.5 M $\Omega$  decade resistor, B is 2 mercury batteries (2.7 V), and V is a HP3457A multimeter.

$\rho_{RoomTemp} / \rho_{9K}$ , was  $2.44 \pm 0.1$ . The superconducting transition temperature,  $T_{c,f}$ , was 8.437 K with a width of 0.025 K. In Run 4.15, the film was  $2710 \pm 50 \text{ \AA}$  thick. It had a room temperature resistivity of  $30.8 \pm 1 \mu\Omega\text{-cm}$  and a resistivity ratio of  $2.90 \pm 0.1$ . Due to difficulties with the thermometry, the exact  $T_{c,f}$  of this sample was difficult to determine, but it was higher than that of Run 4.16, probably around 8.7 K. The width of the transition was less than 0.05 K.

Since we are studying the tunneling of trapped hydrogen impurities in the Nb films, it would be useful to know the exact concentration of hydrogen and other impurities in our films. However, this is not easy to determine in thin films at low concentrations. The depressed  $T_{c,f}$  indicates that the niobium was not single crystal and included impurities. DeSorbo<sup>21</sup> found that oxygen impurities had a much larger effect on the  $T_c$  of high purity niobium than either nitrogen or hydrogen.  $T_c$  was decreased by 0.93K / at. % O for concentrations less than 3.83 at. %. Concentrations of H and N up to a few atomic percent only varied  $T_c$  by less than 0.1 K. This leads to the conclusion that our films had oxygen impurities  $\leq 1$  at. %. No conclusion about the concentration of N or H can be drawn from  $T_{c,f}$ . As shown by the narrow width, the films were homogeneous.

Typically concentrations of hydrogen in bulk Nb are determined by x-ray lattice parameter, extraction, or resistivity measurements. Interpretation of lattice parameter measurement on thin films is problematic as it has been found that at concentrations less than 2 at. % films remained clamped in the plane of the substrate and only expand perpendicular to the plane.<sup>22,23</sup> Also other impurities such as N, O, and C which we expect to be in our sample will cause expansion as well as H. Extraction of hydrogen is accomplished by heating the sample to 2000 °C<sup>24</sup> in a vacuum and monitoring the change in partial pressures. This would in all likelihood be detrimental to the LiNbO<sub>3</sub> substrate and in any case is beyond the capabilities of the heater in our UHV chamber.

Finally, Reisfeld et al.<sup>25</sup> have studied the change in resistivity of thin films of sputtered Nb with concentration of hydrogen. Their films had a  $T_{c,f}$  of about 8.8 K and resistivity ratios of 1.8 to 3. The uncharged resistivity of their films was on the order of 30  $\mu\Omega$ -cm. They measured an increase in the resistivity of 0.6  $\mu\Omega$ -cm / at. % H which is in close agreement with the value of 0.64  $\mu\Omega$ -cm / at. % found in bulk.<sup>26</sup> The resistivity of the samples discussed in this thesis is on the order of their base, uncharged, resistivity. This indicates that the concentration of hydrogen impurities is less than 1 at. %. This is also in agreement with the films grown by Steiger et al.<sup>27</sup> These films were deposited by electron beam evaporation in a UHV chamber and their hydrogen concentration measured using the nuclear reaction  ${}^1\text{H}({}^{15}\text{N},\alpha\gamma){}^{12}\text{C}$ . It was found that their base, uncharged, films contained a non zero concentration of hydrogen of < 1 at. %.

We thus conclude that our samples do contain hydrogen, oxygen and other impurities. The H and O impurities are on the order of or less than 1 at. %. Since C and N were also present in the UHV chamber, in all likelihood there was C and N in our samples as well.

### III.4.iv SAW devices with Nb film overlayers

#### *Change in resonant frequency and bandwidth of SAW device after mounting in Kelvinox*

After the Nb was deposited and the SAW device mounted in the Kelvinox sample holder (discussed further in III.5 and III.6), the bandwidth and resonant frequencies changed. The A channel had a resonant frequency of  $(687 \pm 5)$  MHz and a 3 dB bandwidth of 62 MHz. The C channel had a resonant frequency of  $(692 \pm 7)$  MHz and a 3 dB bandwidth of 60 MHz. The device was inspected after deposition and there were only slight changes in the transducers from before deposition. Thus the changes in bandwidth and resonant frequency are not due to the transducers, rather they are due to differences in the electrical connections to the transducers between the room temperature and Kelvinox sample holders (which is discussed further in III.5). In the Kelvinox sample holder electrical contact is made by wires silver painted onto the transducer pads. Since the bandwidth increased in the Kelvinox holder, the contacts are better matched to the impedance of the transducers than the bellows contacts.

#### *Change in attenuation due to deposition of niobium*

Measuring the attenuation of the acoustic signal at the resonant frequency as outlined in Appendix A, the change in attenuation upon deposition of the films was  $12.6 \pm 0.9$  dB for channel A (3 mm long sample of niobium) and  $7.9 \pm 0.9$  dB for channel C (1.5 mm long sample of Nb). There are several difficulties with this measurement. First it is comparing attenuations measured in the room temperature holder (pre Nb) with those measured in the Kelvinox holder (post Nb). From the above discussion, it is obvious that the resonance curves and thus the response of the transducers depend on the external circuit. The above uncertainties of 0.9 dB do not include a change in insertion loss and

thus are a gross understatement. By Eq. 3.4, the change in attenuation in the 1.5 mm channel should be  $\frac{1}{2}$  of the change in the 3 mm channel. In summary, channel C, 1.5 mm of Nb, did have less attenuation due to the deposition of Nb than channel A, 3.0 mm of Nb, but the exact change is difficult to determine.

#### *Change in velocity due to deposition of niobium*

The velocity of the acoustic wave was measured at room temperature before and after the deposition of the Nb. This was done by a technique similar to optical interferometry. A signal was split into two paths, one purely electromagnetic and continuous wave, the other pulsed electromagnetic and acoustic. The acoustic part of the second path is a SAW channel. The signals were then recombined in a microwave mixer. The output of this mixer is proportional to the phase difference between the two inputs. Using the relationship between the change in velocity and the change in frequency as derived in Appendix B, the velocities in Table 3.1 were found. Note that there are two delays stated for each channel. The interferometric delay was calculated using the equation derived in Appendix B.1. The time of flight delay was obtained from the time delay between the main pulse and the delayed pulse as observed on an oscilloscope.

The large uncertainties in the velocities are from uncertainties in the acoustic path lengths obtained from photographs from a Bausch and Lomb microscope. The various pathlengths are summarized in Table 3.2.

The 2915 Å of Nb film changed the velocity of the SAW in the region covered by Nb. Using the interferometric signal delays from Table 3.1, the delay changed by  $(0.204 \pm 0.005)$  μsec in channel A (3 mm of Nb) and by  $(0.104 \pm 0.004)$  μsec in channel C (1.5

Table 3.1 The delays and velocities measured at room temperature.

Measure- ment	Inter- ferometric signal $\tau_a$ ( $\mu\text{sec}$ )	Time of flight $\tau_a$ ( $\mu\text{sec}$ )	Inter- ferometric signal $\tau_c$ ( $\mu\text{sec}$ )	Time of flight $\tau_c$ ( $\mu\text{sec}$ )	LiNbO <sub>3</sub> phase velocity (m/s)	LiNbO <sub>3</sub> group velocity (m/s)	Nb:H on LiNbO <sub>3</sub> phase velocity (m/s)	Nb:H on LiNbO <sub>3</sub> group velocity (m/s)
No Nb R.T. Holder	1.520 $\pm$ 0.002	1.510 $\pm$ 0.015	1.539 $\pm$ 0.002	1.529 $\pm$ 0.01	3980 $\pm$ 30	4000 $\pm$ 40	—	—
No Nb R.T. Holder	1.527 $\pm$ 0.01	1.510 $\pm$ 0.01	1.544 $\pm$ 0.003	1.525 $\pm$ 0.01	3970 $\pm$ 40	4010 $\pm$ 40	—	—
Nb, in Kelvinox	1.725 $\pm$ 0.004	1.732 $\pm$ 0.01	1.642 $\pm$ 0.003	1.642 $\pm$ 0.01	3910 $\pm$ 120	3930 $\pm$ 130	3200 $\pm$ 100	3170 $\pm$ 110

Table 3.2. The measured lengths in the acoustic channels

Channel	Total length (mm)	Uncovered LiNbO <sub>3</sub> length (mm)	LiNbO <sub>3</sub> covered with Nb length (mm)
A	6.08 ± 0.06	3.06 ± 0.07	3.02 ± 0.03
C	6.10 ± 0.08	4.64 ± 0.09	1.46 ± 0.02

mm of Nb). We find a change in velocity,  $\frac{v_N - v_L}{v_L}$ , of  $(- 18.8 \pm 3) \%$ . Using Eq. 3.2, we found a predicted velocity change of  $(- 9.68 \pm 0.5) \%$  from mass loading using  $c_{11} = 2.46 \times 10^{11} \text{ (N/m}^2\text{)}$ ,  $c_{12} = 1.32 \times 10^{11} \text{ (N/m}^2\text{)}$ ,<sup>28</sup>  $v = (3937 \pm 91) \text{ m/s}$ ,  $h = (2915 \pm 50) \text{ \AA}$ ,  $\omega|u_1(0)|^2/P_1 = 3.16 \times 10^{-12} \text{ (m}^3\text{/J)}$ , and  $\omega|u_3(0)|^2/P_1 = 6.86 \times 10^{-12} \text{ (m}^3\text{/J)}$ .<sup>29</sup> The values for  $\omega|u_i(0)|^2/P_1$  are for Y-cut Z-propagating LiNbO<sub>3</sub> as values were not available for the 128° X-propagating cut. Thus they are only ballpark values for the 128° cut. For the change in the velocity due to electrical shorting of the surface a value for the 128° cut is available, it is  $- 2.72 \%$ .<sup>30</sup> Thus the sum of the predicted change in velocity is  $(-12.40 \pm 0.5)\%$ . This is smaller than the observed  $\Delta v/v$  of  $(-18.8 \pm 3) \%$ , but considering that the power flow from another cut of LiNbO<sub>3</sub> was used, the calculated value is not far off.

#### *Transducer fabrication conclusions.*

We conclude from Tables 3.1 and 3.2 that the path lengths were not identical in the two channels. Both the delays before the Nb was deposited and the measured lengths indicate that the path in channel C was slightly longer than that in channel A. This was

probably due to backlash in the translational stages of the SEM. The velocity in the  $\text{LiNbO}_3$  is close to the material specified velocity of 3992 m/s indicating that the transducer alignment on the crystal was quite good.

### III.5 Low Temperatures

In order to reach temperatures below 0.1 K, an Oxford Kelvinox Dilution Refrigerator was used. Figure 3.12 is a schematic of the Kelvinox, capable of reaching temperatures as low as 35 mK. This refrigerator was inserted into a cryogenic dewar which held a superconducting magnet, with maximum field of 14 T. A sample holder was suspended from the bottom of an extension from the carousel of the Kelvinox so that the sample was in the middle of the magnetic field with the field lines perpendicular to the substrate.

There were three thermometers in the refrigerator. A NBS superconducting standard and a Pt thermometer were mounted on the carousel. The superconducting standard was a fixed point thermometer with resistive transitions at 7.021 K, 3.42 K, 1.174 K, 0.844 K, 0.515 K, and 0.20593 K. The Pt thermometer was calibrated from room temperature to 7K. However, its resolution was quite poor below 15 K. A RuO thermometer was mounted on the back of the sample holder and calibrated against the fixed points of the superconducting standard. See Appendix C for the calibration curves of the thermometers.

#### *High frequency cables in the Kelvinox.*

The major modifications made to the Kelvinox to accomplish high frequency measurements were the addition of high frequency coaxial cables and a sample holder for SAW devices.

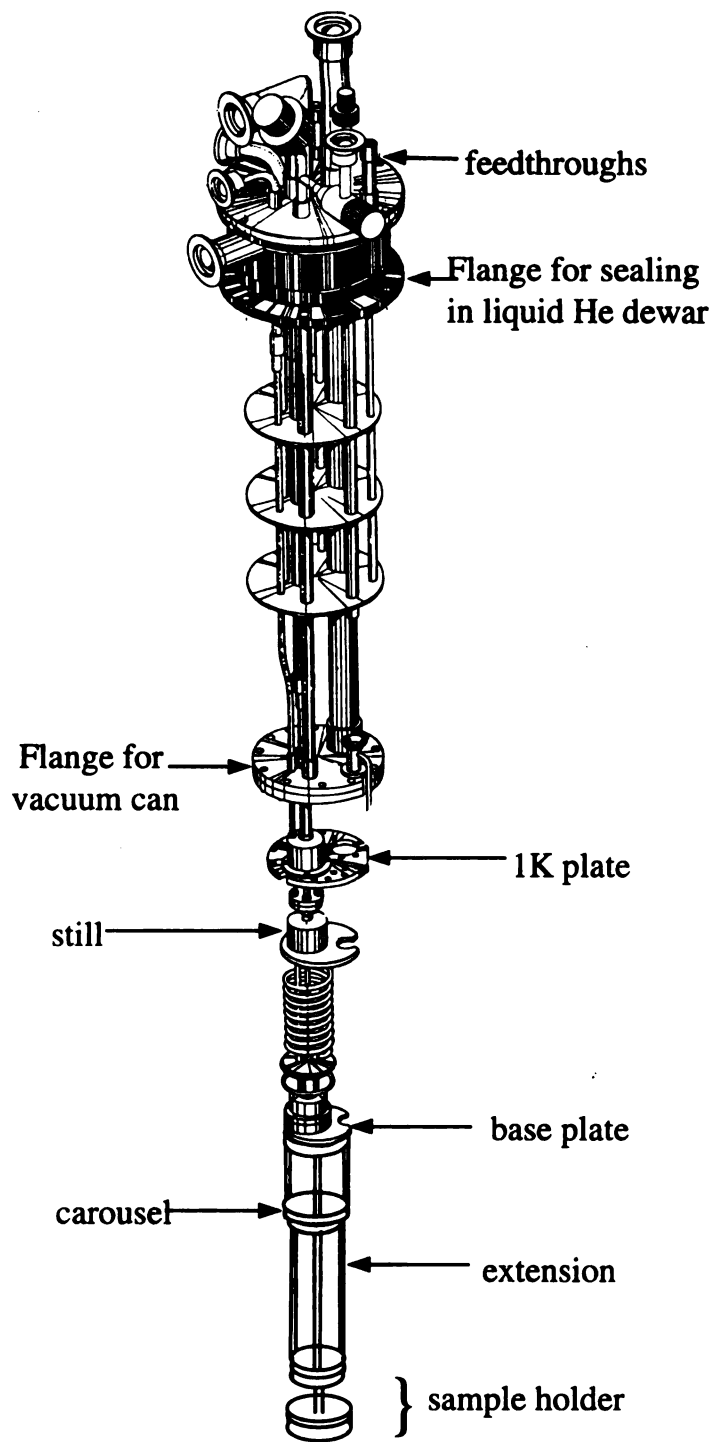


Figure 3.12. The insert for the Oxford Kelvinox. Drawing is adapted from that in the Kelvinox operating manual.

The design and installation of the high frequency cables was a group effort. The coaxial cable assemblies needed low loss, low heat leak, and to be leak tight at the top of the Kelvinox. The feedthrough at the top of the refrigerator was designed and made by Mike Jaeger and Ashraf Yussouff. It consisted of 4 homemade 0.085" semi-rigid coaxial cables. Stycast 2850 was used as the dielectric and SMA connectors were put on both ends of the cables. Three of the homemade coaxes were then connected to standard 0.085" semi-rigid BeCu coaxial cables. These cables ran from the feedthrough to a heat sink attached to the cold plate. The feedthroughs and the 0.085" cables had a rf loss of 1 to 1.5 dB per assembly at 700 MHz. Figure 3.13 is a schematic of one chamber of the heat sink.

The heat sink's purpose was to cool the center and outer conductors of the coaxes to the 1.2 K cold plate. It consisted of a brass box with 3 chambers around an OFHC copper block. Each chamber was used to cool one high frequency line. SMA launchers were installed on both ends of a chamber containing a sapphire microstrip waveguide. The

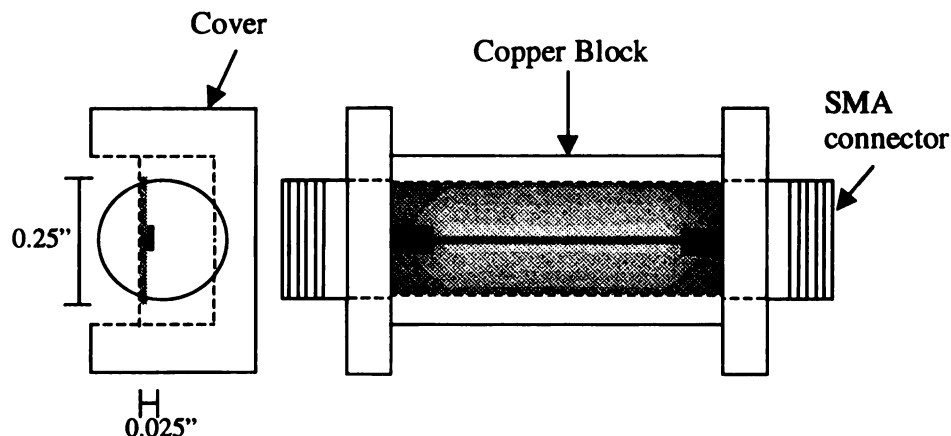


Figure 3.13. At left is a side view of one chamber of the heatsink. At the right, the cover has been removed from the chamber so the sapphire substrate is visible . The launcher tongues of the SMA  rest on the 0.025" wide gold strip .

outer conductor was cooled through physical contact to the heat sink box which was in turn connected to the cold plate. The waveguide consisted of a sapphire substrate with a thin film ground of Ti/Au completely covering the back and a 0.025" strip of Ti/Au on the top. The microstrip was designed for 50  $\Omega$  by adjusting the strip width. The sapphire substrate was greased onto the copper block which was thermally connected to the cold plate. Sapphire was chosen because of its high thermal conductivity. The heat sink attenuation was 0.5 dB at 700 MHz.

The coaxial cables between the heat sink and the sample holder were 0.020" O.D. coax with SMA connectors on both ends. The small size minimized the heat leak to the sample. Two cables, made of BeCu, were used for the receivers with a loss of about 1.2 dB each. The third transmitter coax had a stainless jacket with a center conductor of silver-plated copper-clad steel and contributed a 2.5 dB loss at 700 MHz. The total loss was 3 dB for the receiver assemblies and 4.7 dB for the transmitter assembly.

The sample holder was made of OHFC copper and attached to the bottom of the carousel extension on the Kelvinox. The length of the extension was adjusted to position the substrate at the center of the solinoid's the magnetic field. The SAW device was greased onto the face of the holder and held in place by BeCu clips to maintain good thermal contact with the holder.

### III.6 Electronics

Our experiments in the Kelvinox were carried out in a shielded room to minimize interference from outside electromagnetic forces. The electronics outlined below and in Appendix A were used in Run 4.16.

Pulse widths of 80-100 nsec and rates of 1000 Hz were used. Pulsed operation was used for several reasons. First, with pulsed signals we could separate acoustic from electromagnetic signals. The wires (or bellows in the room temperature sample holder) to the transducers sometimes acted as antennas. Thus the detectors would pick up switching noise from the pulse to the generating transducer as well as the signal received at the other receiver. By making the pulses short enough we could separate these various signals. Short pulses also allowed us to distinguish any signals due to the electromagnetic wave bouncing back in forth in the long, 10 m, cables connecting the electronic equipment outside and inside the shielded room. In addition to avoiding interference effects we used short pulses and low repetition rates to minimize any heating effects by the signals. The power per pulse using the standard diode detector setup was on the order of 40  $\mu$ W. When the sample was below 1 K and we were looking for saturation effects, the power per pulse was cut down to 9 nW.

Two basic circuits were used to measure the attenuation and change in velocity. Figure 3.14 is a diagram of the circuit used above 1.2 K. A more detailed discussion of the various components and the operation of the circuit are presented in Appendix A.

In this circuit the changes in attenuation were measured using diode detectors. The detectors were calibrated by substituting a variable attenuator for the coaxes in the refrigerator and the SAW device. The change in velocity was measured by homodyning. The output of a balanced mixer is proportional to the phase difference between the two inputs. The output signal was sampled by a boxcar; the resultant signal was fed to a voltage controlled oscillator via an integrater. This formed a phase-locked-loop which maintained constant phase difference by varying the oscillator frequency. The change in

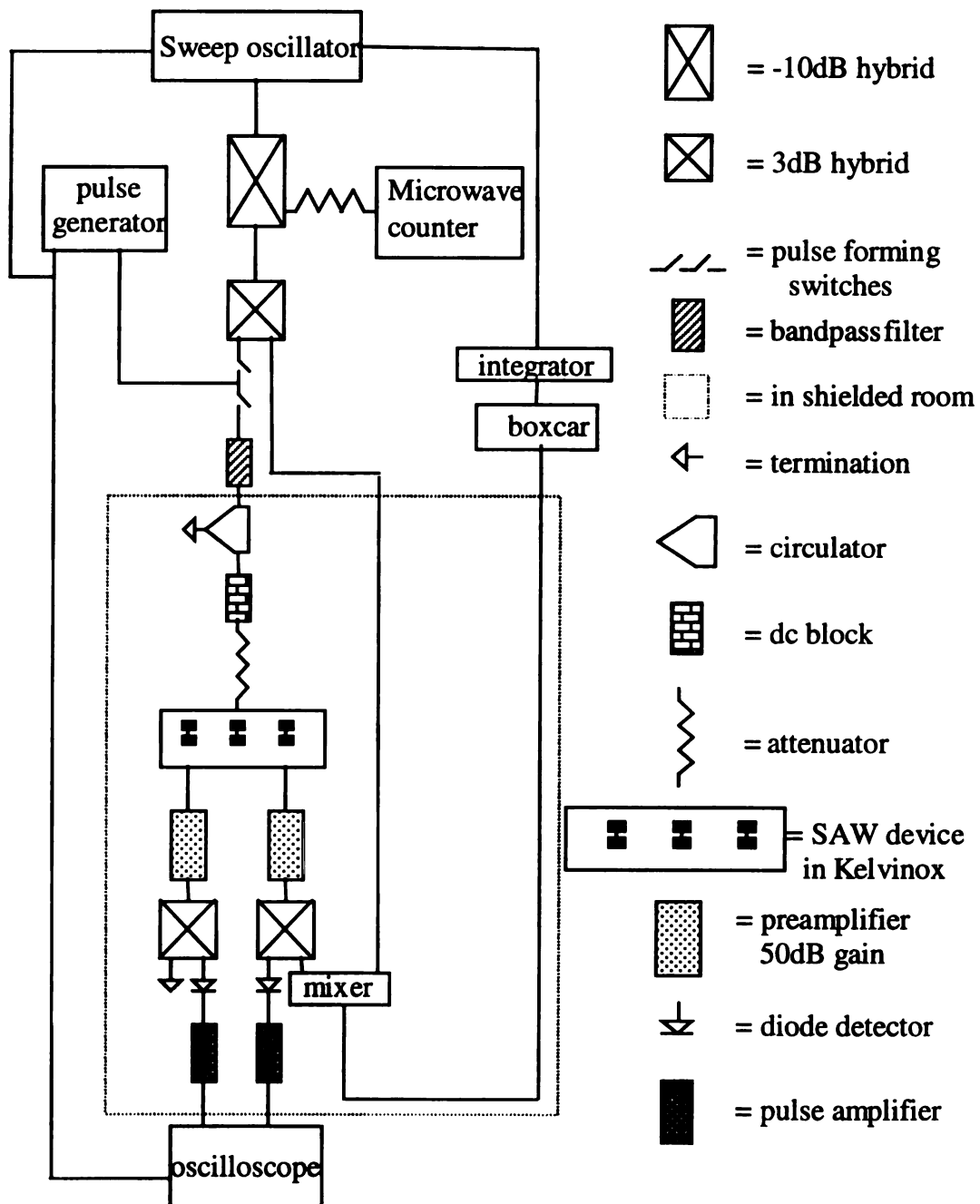


Figure 3.14. The circuit for measurements above 1.2 K. Pulsed signals are sent to the generating transducer. The attenuation of the signal in the acoustic path is measured by diode detectors. The velocity is measured by phase locking the circuit.

frequency was proportional to the change in the average velocity in the acoustic path. This relationship is discussed in greater detail in Appendix B.2.

Below 1.2 K the attenuation was measured with a homodyne circuit. This allowed us to greatly decrease the acoustic power. However, it was not possible to measure the attenuation of both acoustic channels using the homodyne method as explained in Appendix A. Therefore, in Run 4.16 only the 3 mm Nb channel was measured below 1.2 K.

The signal sides of the transducers were connected to the launcher tongues of the SMA connectors with 38 gauge insulated wire, see Figure 3.15. Connections were made using silver paint with butyl acetate as the solvent. The grounds of the transducers were individually grounded at separate screws on the sample holder. This was found to greatly reduce the pickup between the transducers. Also, to minimize the pickup between the wires, care was taken that no acoustic wires crossed any other wires.

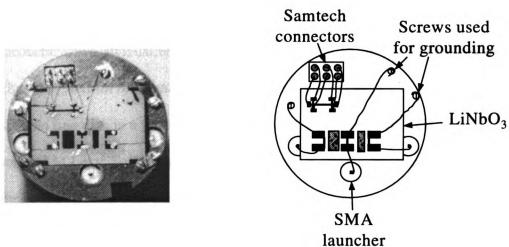


Figure 3.15. On the left is a photo of the Kelvinox sample holder with a wired sample. On the right is a schematic of the same. A Nb film is shown between the transducers.

- <sup>1</sup> “Tunneling of H and D by O(N) in niobium by anelastic relaxation measurements”, G. Cannelli, R. Cantelli, and F. Cordero, *Physical Review B* 34, 7721-7726 (1986).
- <sup>2</sup> “Low-temperature ultrasonic study of trapped hydrogen in niobium”, D.B. Poker, G.G. Setser, A.V. Granato, and H.K. Birnbaum, *Physical Review B* 29, 622-629 (1984).
- <sup>3</sup> “Isotope dependence of hydrogen tunneling in niobium”, W. Morr, A. Müller, G. Weiss, H. Wipf and B. Golding, *Physical Review Letters* 63, 2084-2087 (1989).
- <sup>4</sup> “Elastic Surface Waves”, G. W. Farnell in *Surface Wave Filters*, edited by H. Matthews, (John Wiley and Sons, New York, 1977) pp. 1-54.
- <sup>5</sup> *Surface – Wave Devices for Signal Processing*, by D.P.Morgan (Elsevier Science Publishing Co, New York, 1985) p. 33.
- <sup>6</sup> There is some disagreement on the prefactor. Farnell<sup>4</sup> defines it to be 2 in analogy to the bulk wave case while Morgan (p 153) defines it to be 2.255 using the number found with quasi-static analysis. In this thesis 2 will be used as the prefactor.
- <sup>7</sup> “Surface acoustic wave attenuation by a thin film”, D. R. Snider, H.P. Fredrickson, S.C. Schneider, *Journal of Applied Physics* 52, 3215-3222 (1981).
- <sup>8</sup> “Ultrasonic mean free path in a granular aluminum film”, M. Tachiki, H. Salvo, Jr., D.A. Robinson and M.Levy, *Solid State Communications* 17, 653 – 656 (1975).
- <sup>9</sup> Doctoral thesis H.P. Baum, University of Milwaukee, 1990 p. 40.
- <sup>10</sup> “ Surface acoustic wave investigation of superconducting films”, M. Levy, *Journal de Physique* C10, C10-691 – C10 – 698 (1985).
- <sup>11</sup> “Simple theory of acoustic amplification”, R. Adler, *IEEE Transactions on Sonics and Ultrasonics* SU – 18, 115-118 (1971).

- 
- <sup>12</sup> “Electron-phonon, acousto-electric and magneto-elastic SAW interactions with superconducting films, 2-D electron gas or magnetic films”, M. Levy and S.C. Schneider in *Perspectives in Physical Acoustics* Ed. by Y. Fu, R.K. Sundfors, and P. Suntharothok, (World Scientific, New Jersey, 1991) pp. 150-200.
- <sup>13</sup> “Optimum cut for rotated Y-Cut LiNbO<sub>3</sub> crystal used as the substrate of acoustic-surface-wave filters”, Kimio Shibayama, Kazuhiko Yamanouchi, Hirqaki, Sato and Toshiyasu Meguro, *Proceedings of the IEEE* 64, 595-597 (1976) and Morgan *ibid* p.152.
- <sup>14</sup> “Applications of double electrodes in acoustic surface wave device design”, T.W. Bristol, W.R. Jones, P.B. Snow and W.R. Smith, *IEEE Ultrasonics Symposium Proceedings*, 343 – 345 (1972).
- <sup>15</sup> “Principles of surface wave filter design”, R.H. Tancrrell in *Surface Wave Filters*, edited by H. Matthews, (John Wiley and Sons, New York, 1977) pp. 109-164.
- <sup>16</sup> Morgan, *ibid* p. 161.
- <sup>17</sup> Morgan, *ibid* p. 160.
- <sup>18</sup> Morgan, *ibid* p. 159-162.
- <sup>19</sup> “Elastic wave propagation in thin layers”, G.W. Farnell and E.L. Adler in *Physical Acoustics IX* edited by W.P. Mason, (Academic Press, NewYork, 1972) pp. 35-128.
- <sup>20</sup> “Elastic properties of hydrogen-loaded epitaxial films”, P.M. Reimer, H. Zabel, C.P. Flynn, A. Matheny, K. Riley, J. Steiger, S Blässer and A. Weidinger, *Zeitschrift für Physikalische Chemie* 181, 367-373 (1993).

- 
- <sup>21</sup> “Effect of dissolved gases on some superconducting properties of niobium”, Warren DeSorbo, *Physical Review* 132, 107-121 (1963).
- <sup>22</sup> “Hydrogen in Nb and Nb/Ti/Nb thin films”, J. Steger, S. Blasser, O. Boebel, J. Erxmeyer, B. Mertesacker and A. Weidinger, *Zeitschrift für Physikalische Chemie* 181, 381-386 (1993).
- <sup>23</sup> “Anomalous lattice expansion of metal-hydrogen thin films”, P.F.Miceli, H. Zabel, J.A.Dura, and C.P. Flynn, *Journal of Materials Research* 6, 964-968 (1991).
- <sup>24</sup> “Solution of hydrogen in niobium”, J.A. Pryde and C.G. Titcomb, *Transactions of the Faraday Society* 65, 2758-2765 (1969).
- <sup>25</sup> “Hydrogen absorption by thin Pd/Nb films deposited on glass”, G. Reisfeld, Najeh M. Jisrawi, M.W. Ruckman, and Myron Strongin, *Physical Review B* 53, 4974- 4979 (1996).
- <sup>26</sup> “The trapping of hydrogen in niobium by nitrogen interstitials”, G. Pfeiffer and H. Wipf, *Journal of Physics F* 6, 167-179 (1976).
- <sup>27</sup> “Solubility of hydrogen in thin niobium films”, J. Steiger, S. Blässer, and A. Weidinger, *Physical Review B* 49, 5570- 5574 (1994).
- <sup>28</sup> “The stability curve for short wavelength density fluctuations of deuterium in niobium”, H. Conrad G. Bauer, G. Alefeld, T. Springer and W. Schmatz., *Z. Physik* 266, 239-244 (1974).
- <sup>29</sup> “Elastic Surface Waves”, G. W. Farnell in *Surface Wave Filters*, edited by H. Matthews, (John Wiley and Sons, New York, 1977) pp. 1-54.
- <sup>30</sup> Morgan, *ibid* p. 152.

## IV. Results

The absolute velocity, change in velocity, and attenuation of Nb films on LiNbO<sub>3</sub> at temperatures between 100 mK and room temperature are presented in this chapter. Since the thickness of the film overlayers was less than 10% of the acoustic wavelength, the films acted as a weak perturbation on SAW propagation as discussed in Chapter III. In the temperature range of most interest,  $T < 20$  K, the attenuation and velocity due to LiNbO<sub>3</sub> is taken as temperature-independent. Thus we will focus on changes in velocity and attenuation below 11 K which are due solely to the Nb. Therefore the interactions between phonons, electrons, and tunneling systems in the Nb:H can be isolated and extracted.

The results presented below are derived from two independent experimental runs. By run, we use the experimental notation Run i.j, where  $i = 4$  denotes the Kelvinox cryostat and the second index denotes the  $j$ th cooldown of the system. Each run studied the Nb:H system using 700 MHz surface waves on LiNbO<sub>3</sub> substrates. Each run constituted a different Nb:H film prepared by electron beam evaporation. Within each run, two separate experiments were performed because the SAW design allowed for bidirectional propagation with two independent receivers. In Run 4.15, a SAW interacted with a Nb:H film, 3 mm long by 270 nm thick, in one channel. The other channel was masked during evaporation and contained a bare LiNbO<sub>3</sub> substrate. This allowed us to separate the properties of Nb:H on LiNbO<sub>3</sub> from the LiNbO<sub>3</sub> itself. In Run 4.16, from which most of the data presented below originate, two Nb films with identical physical properties but different lengths were studied: channel A comprised a film 3 mm in length, designated as sample A; sample C comprised a film 1.5 mm long. Since the samples were deposited

simultaneously, they had an identical thickness of 290 nm. The two samples allowed us to check that the results scaled appropriately with interaction length.

#### IV.1 Velocity measurements

The absolute phase velocity of the acoustic wave was measured at fixed temperatures throughout the experiments. The circuit used to measure the absolute velocity is similar to that used to measure the change in velocity as described in Appendix A except it is no longer phase-locked. A CW (continuous wave) signal from a signal generator is split into two paths. The CW path is purely electromagnetic. In the second path the signal is gated into short pulses and generates a SAW, propagating through the sample. Thus this path has a length in which the signal travels with an acoustic velocity in addition to a length in which it travels with an electromagnetic velocity. Signals from the two paths interfere in a microwave mixer. The output of a microwave mixer is proportional to  $\cos(\Delta\phi)$ , where  $\Delta\phi$  is the phase difference at the inputs. The mixer output can be observed on a scope and the change in frequency,  $\Delta f$ , of the signal generator corresponding to a  $2\pi$  shift is measured. From  $\Delta f$  the acoustic delay was obtained using the result derived in Appendix B.1.

Since the transmitter-receiver separation was 6 mm, the SAW always propagated through a region without any Nb:H. In Run 4.16 when both acoustic paths contained Nb:H, we calculated the bare  $\text{LiNbO}_3$  velocity,  $v_L$ , and the Nb:H on  $\text{LiNbO}_3$  velocity,  $v_N$  with,

$$v_L = \frac{L_{LC} - L_{LA} \left( \frac{L_{NC}}{L_{NA}} \right)}{\tau_C^{ac} - \tau_A^{ac} \left( \frac{L_{NC}}{L_{NA}} \right)} \quad (4.1)$$

$$v_N = \frac{L_{NA}}{\tau_A^{ac} - \frac{L_{LA}}{v_L}} \quad (4.2)$$

where  $\tau_A^{ac}$ ,  $L_{LA}$ , and  $L_{NA}$  are the measured acoustic delay time, the length of the bare  $\text{LiNbO}_3$ , and the length of the Nb:H on  $\text{LiNbO}_3$  region in sample A, respectively. The delay and lengths of sample C are similarly denoted. This relationship is also derived in Appendix B.1.

Table 4.1 summarizes the velocity results from Run 4.16. Note that there are two delays stated for each acoustic path. The “interferometric” delay was found using the method outlined above and in Appendix B.1. The “time of flight” delay was simply obtained by observing the separation between an electromagnetic excited main pulse and a delayed acoustic pulse. This method strictly yields a group velocity. The larger uncertainty in this delay is due to the rise time of the pulses. As seen in the last two columns of Table 4.1, the two methods agree quite well. This implies that the group velocity is, within error, the same as the phase velocity and therefore the propagation is nondispersive. The large uncertainties in the velocities are due to the difficulty in measuring the exact lengths in the acoustic paths. Lengths are summarized in Table 3.2.

The delays in both paths on Run 4.16 decreased by about 20 nsec when the sample was cooled from 300 K to liquid nitrogen temperature due to an increase in the acoustic velocity. This shift corresponds to a temperature coefficient,  $\alpha_T$ , of  $58 \times 10^{-6} \text{ K}^{-1}$  in A and

Table 4.1. Delays and velocities measured in Run 4.16.

Temperature (K)	$\Delta f$ (MHz) Channel A	$\Delta f$ (MHz) Channel C	Interferometric signal $\tau_A$ ( $\mu$ s)	Time of flight $\tau_A$ ( $\mu$ sec)	Interferometric signal $\tau_c$ ( $\mu$ sec)	Time of flight $\tau_c$ ( $\mu$ sec)	LiNbO <sub>3</sub> phase velocity (m/s)	LiNbO <sub>3</sub> group velocity (m/s)	Nb:H on LiNbO <sub>3</sub> phase velocity (m/s)	Nb:H on LiNbO <sub>3</sub> group velocity (m/s)
300	$0.571 \pm 0.001$	$0.599 \pm 0.001$	$1.725 \pm 0.004$	$1.73 \pm 0.01$	$1.642 \pm 0.003$	$1.64 \pm 0.01$	$3910 \pm 120$	$3930 \pm 130$	$3200 \pm 110$	$3170 \pm 110$
$85 \pm 5$	$0.5775 \pm 0.0005$	$0.6069 \pm 0.0004$	$1.705 \pm 0.003$	$1.71 \pm 0.01$	$1.621 \pm 0.002$	$1.625 \pm 0.01$	$3970 \pm 120$	$3960 \pm 130$	$3230 \pm 100$	$3220 \pm 120$
7	$0.5785 \pm 0.0005$	$0.6084 \pm 0.0007$	$1.703 \pm 0.003$	$1.70 \pm 0.03$	$1.617 \pm 0.003$	$1.61 \pm 0.03$	$3980 \pm 140$	$3990 \pm 200$	$3230 \pm 100$	$3240 \pm 190$
1.35	$0.5794 \pm 0.0006$	$0.6071 \pm 0.0004$	$1.700 \pm 0.002$	$1.70 \pm 0.03$	$1.621 \pm 0.002$	$1.62 \pm 0.03$	$3960 \pm 120$	$3970 \pm 200$	$3260 \pm 110$	$3250 \pm 190$
300 <sup>a</sup>	$0.5682 \pm 0.0005$	$0.5962 \pm 0.0003$	$1.731 \pm 0.003$	$1.71 \pm 0.03$	$1.648 \pm 0.002$	$1.63 \pm 0.03$	$3900 \pm 120$	$3950 \pm 200$	$3190 \pm 110$	$3230 \pm 190$

<sup>a</sup> A different circuit was used for this measurement, thus the different values of  $\Delta f$ .

$62 \times 10^{-6} \text{ K}^{-1}$  in C, where  $\alpha_T \equiv \frac{1}{\tau} \frac{d\tau}{dT} = \frac{1}{L} \frac{dL}{dT} + \frac{1}{v} \frac{dv}{dT}$ . Since both paths had essentially the same shift, it appears that this change originated in the LiNbO<sub>3</sub> substrate, not the Nb. This is further borne out by the value of  $\alpha_T$  for 128° rotated Y-cut, X-propagating LiNbO<sub>3</sub> is  $75 \times 10^{-6} \text{ K}^{-1}$ .<sup>1</sup>

## IV.2 The change in velocity in the acoustic path

### IV.2.i. Method for measuring the change in velocity

In order to detect the small change in velocity due to tunneling systems, a differential method was used. Using the circuit discussed in Appendix A, the CW signal from the oscillator was split into two paths, one primarily acoustic and the other purely electromagnetic, and then recombined in a mixer. The phase difference between the two paths is kept fixed (unlike in the absolute velocity measurements) by a phase-locking circuit. In the phase-locking circuit, the pulsed output of the mixer is sent to a boxcar integrator, providing a dc output proportional to  $\Delta\phi$ , which in turn is fed to the voltage-controlled input of the oscillator so that a constant phase difference between the two paths is maintained. The change in frequency to maintain a constant phase difference is related to the change in velocity of the Nb:H on LiNbO<sub>3</sub> by

$$\frac{v'_N - v_N}{v_N} = \frac{f' - f}{f} \left( \frac{v_N}{L_N v_{EM}} (L_B^{EM} - L_A) + \frac{v_N L_L}{L_L v_L} + 1 \right) \quad (4.3)$$

where  $v$  is the velocity,  $f$  is the frequency, and  $L$  is the pathlength. The subscripts N and L denote the Nb:H on LiNbO<sub>3</sub> and the bare LiNbO<sub>3</sub> parts of the acoustic path respectively.  $L_A$  is the electromagnetic length of the purely electromagnetic path and

$L_B^{\text{EM}}$  is the electromagnetic length in the path which includes the SAW device (or acoustic length). A general expression for  $\Delta v/v$  is given in Appendix B.2; Eq. 4.3 is a simplified expression when  $v_L$  is temperature-independent. For sample A in Run 4.16, we derive the calibration factor,

$$\frac{\Delta v}{v} = 1.86 \pm 0.04 \frac{\Delta f}{f} \quad (4.4)$$

#### IV.2.ii Results from Run 4.16

##### *10 K to 300 K*

The change in frequency was measured as the sample was cooled. The frequency shift has contributions from the Nb:H region as well as the  $\text{LiNbO}_3$  region, so that the change of the Nb:H velocity alone cannot be extracted. We denote the effective velocity change

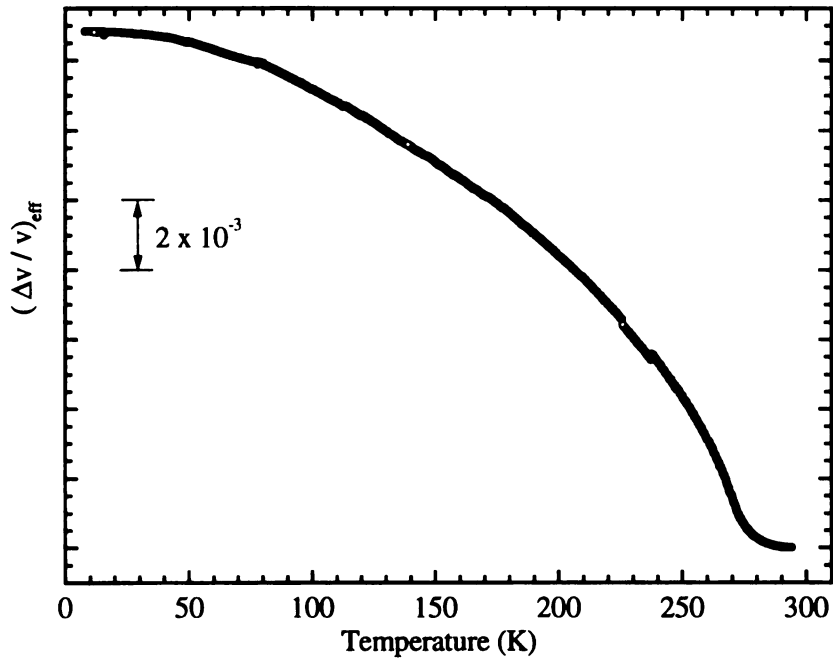


Figure 4.1. The effective velocity change with temperature. The high temperature tail is an experimental artifact.

averaged over the propagation path, as  $v_{\text{eff}}$ . Figure 4.1 shows a change  $(\Delta v/v)_{\text{eff}} = 1.48 \pm 0.02 \times 10^{-2}$  between 10 and 300 K. This is in agreement with the change in the average velocity calculated from the interferometric delays of Table 4.1, which yields a value of  $(\Delta v/v)_{\text{eff}} = 1.44 \pm 0.18 \times 10^{-2}$ .

#### *Change in velocity below 11 K*

In this section we will present the velocity results below 11 K. In this region, striking changes in SAW propagation occur, which are not expected in pure, weakly anharmonic crystalline substances, where the velocity should be temperature-independent. These results are strong evidence for tunneling, and will be further analyzed in Chapter V. There are several features to note in the velocity data shown in Figures 4.2 and 4.3. First, the velocity exhibits a broad maximum at 3.3 K. As we shall discuss in Chapter V, this peak is due to the crossover between resonant and relaxational acoustic interactions with

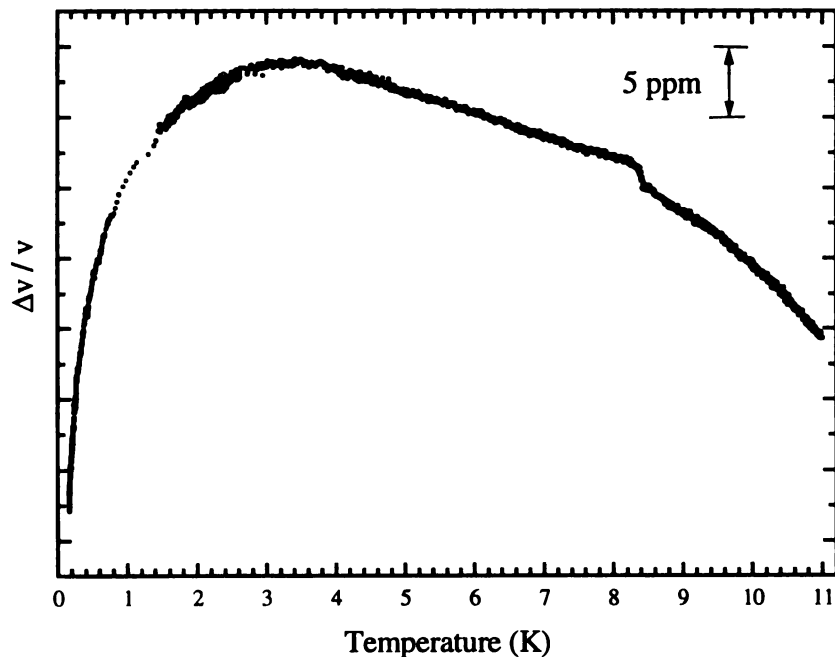


Figure 4.2. The change in velocity below 11 K.

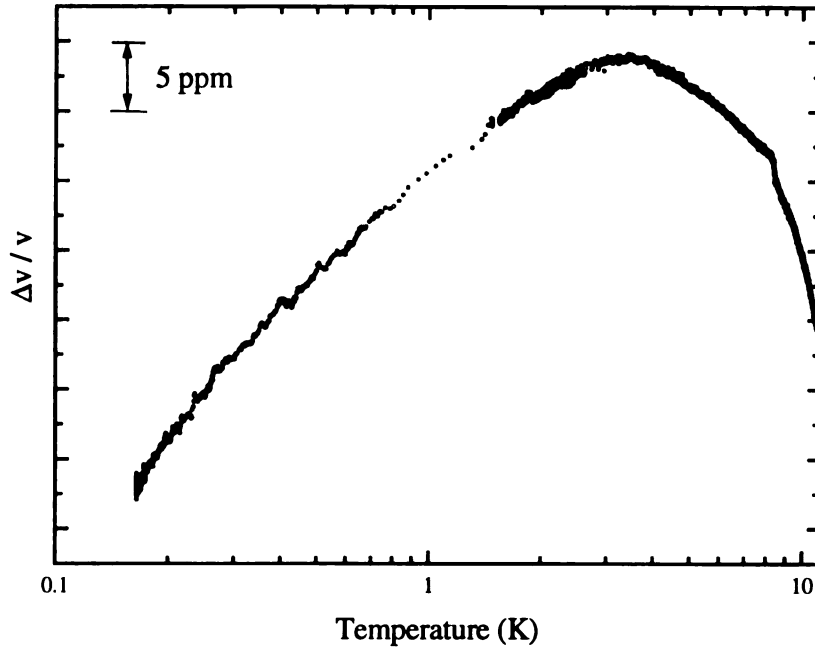


Figure 4.3. The change in velocity below 11 K on a log/linear plot

tunneling systems. Second, as can be seen in Figure 4.3, the velocity varies as  $\log T$  below the maximum. Finally, there is an abrupt jump, with  $\Delta v/v = 1.4 \pm 0.2$  ppm at  $T_{c,f}$ . This jump will be discussed further in Section IV.6.

### IV.3 Change in Attenuation.

#### IV.3.i Attenuation change between 10 and 300 K, Run 4.16

Acoustic attenuation was measured using the technique discussed in Appendix A in the cooldown from room temperature. Results are shown in Figure 4.4. Jumps in the data are spurious and result from mechanical instabilities in the cryostat's coaxial cables. In Figure 4.5 a smooth curve has been derived from the Figure 4.4. For data taken on cooldown, uncertainties occur from the difficulty in ensuring that the transducer

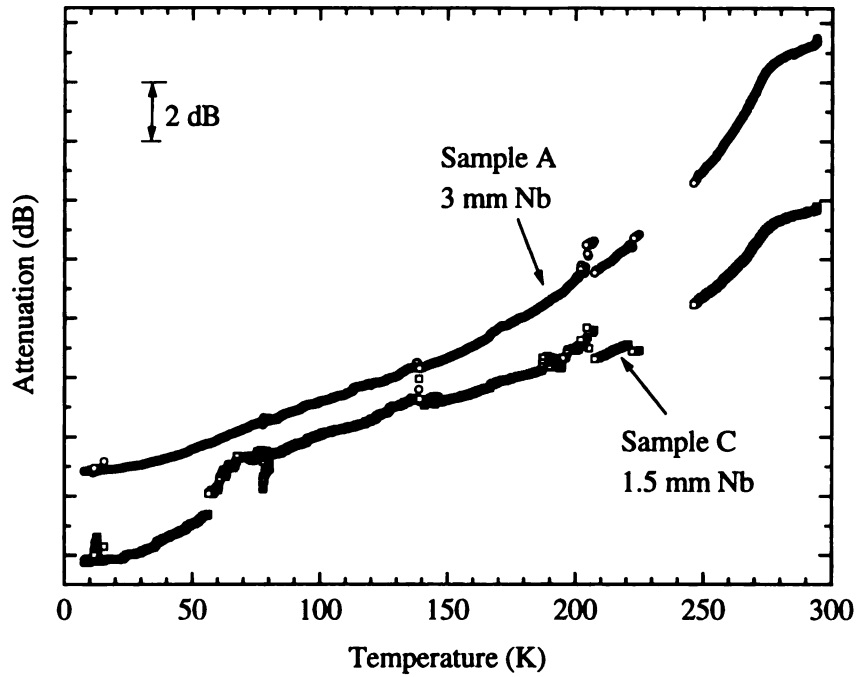


Figure 4.4. The change in attenuation as measured during cooling down.

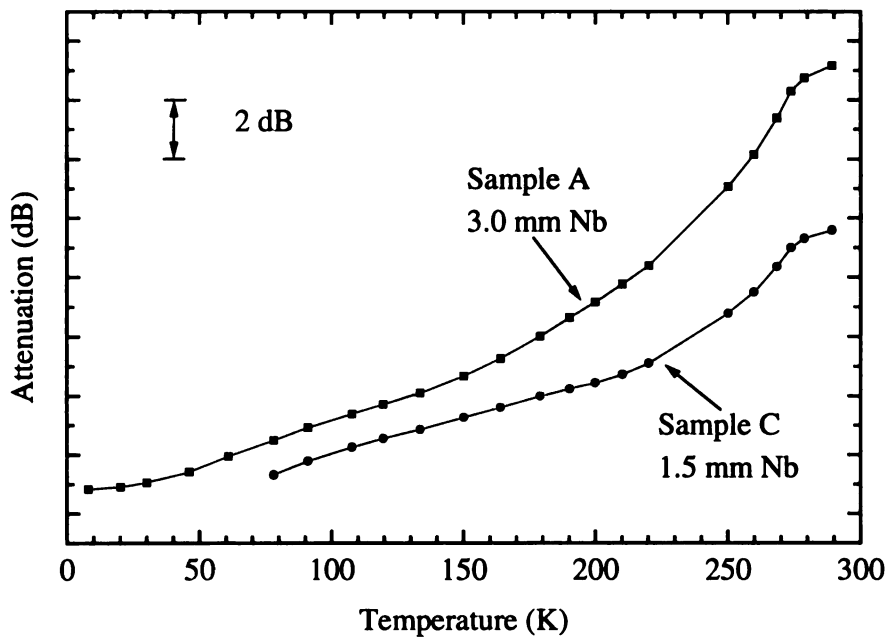


Figure 4.5. Smooth curve extrapolated from the change in attenuation as the samples cooled.

efficiency was constant. For example, the peak (resonant) frequency shifted as much as 25 MHz. To understand this effect we measured the resonance curves at 290, 95, 78, and 6 K and monitored that the signal amplitude was measured within a few MHz of the peaks as the samples cooled. The transducer resonances were measured using the method outlined in Appendix A. From these data, the change in attenuation as a function of temperature at resonance was found. These changes are summarized in Table 4.2.

Table 4.2. Summary of attenuation changes, 6 to 300 K.

Temperature region	Method <sup>b</sup>	Sample A; 3mm Nb:H (dB)	Sample C; 1.5 mm Nb:H (dB)
300 → 80 K	C	-12.65 ± 0.7	-8.3 ± 1.0
300; 80 K	F	-13.25 ± 0.9	-8.9 ± 0.9
80 → 6 K	C	-1.75 ± 0.8	Not measured
80; 6 K	F	-2.2 ± 0.8	-1.0 ± 0.8

<sup>b</sup>C, continuous drift; F, fixed temperature

The two methods of measuring the attenuation agree quite well. If the attenuation in the acoustic paths was only due to the niobium, the attenuation of sample C would be half of that of A. This was not the case as the sample cooled from 300 to 80 K; implying that the attenuation of the LiNbO<sub>3</sub> is also changing. This agrees with data taken for the LiNbO<sub>3</sub> channel in Run 4.15, where the attenuation changed by 4 dB between 300 and 80 K. Accounting for this contribution, we find that the attenuation change for sample A is double that in sample C consistent with the factor of two in the path length.

#### IV.3.ii Change in attenuation below 11 K, Run 4.16

Below 20 K we shall assume that the LiNbO<sub>3</sub> is constant so that any observed change in attenuation is due to the Nb:H. This is supported by the Run 4.15 blank channel data

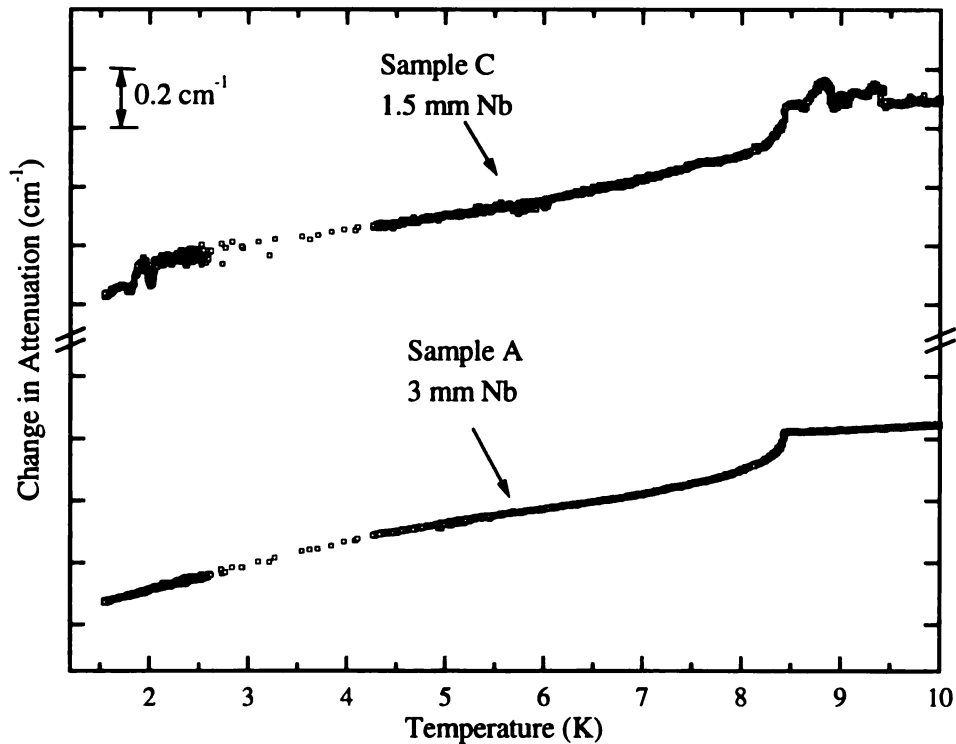


Figure 4.6. The change in attenuation for both samples below 10 K.

below 20 K in which the attenuation was temperature-independent within a scatter of 0.25 dB,  $0.09 \text{ cm}^{-1}$ . Furthermore the transducer resonances were constant below 10 K allowing the attenuation to be measured at the resonance peak. Figure 4.6 shows the change in the attenuation in the two samples measured simultaneously. The overall attenuation shift was normalized to dB/cm by dividing by  $L_N$ , and normalized to  $\text{cm}^{-1}$  by dividing by 4.343.

The change in attenuation in sample A between 8.4 and 2 K was  $(0.510 \pm 0.007) \text{ cm}^{-1}$ . In sample C the attenuation changed by  $(0.54 \pm 0.03) \text{ cm}^{-1}$ , where the larger error reflects a weaker signal to noise ratio. This result justifies our assumption that the attenuation is due solely to the Nb:H.

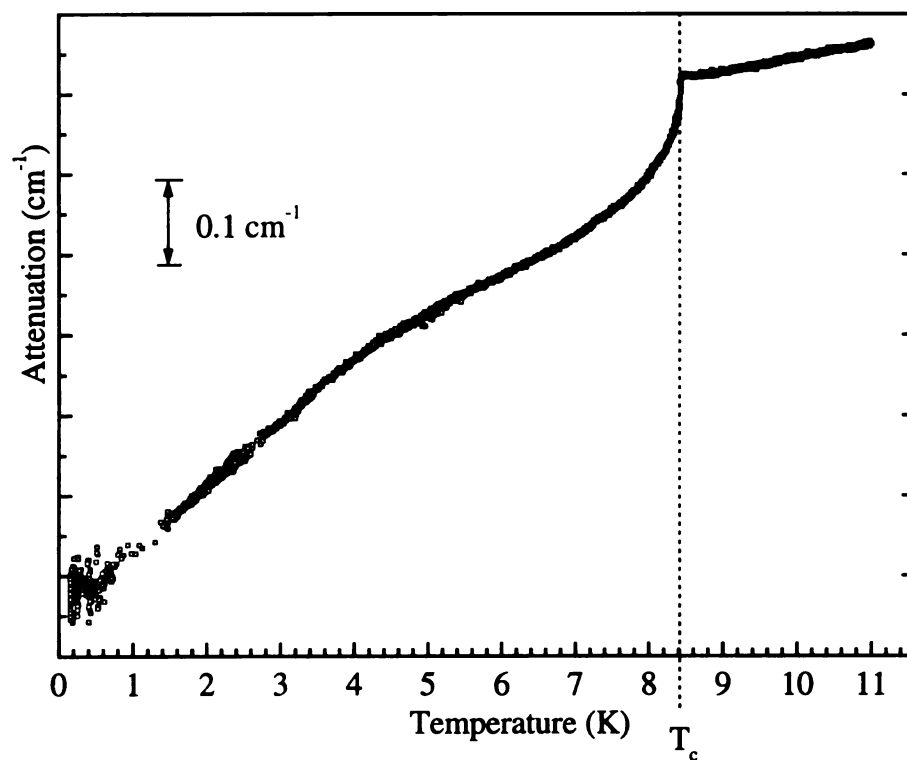


Figure 4.7. The change in attenuation in sample A between 0.16 K and 11 K.

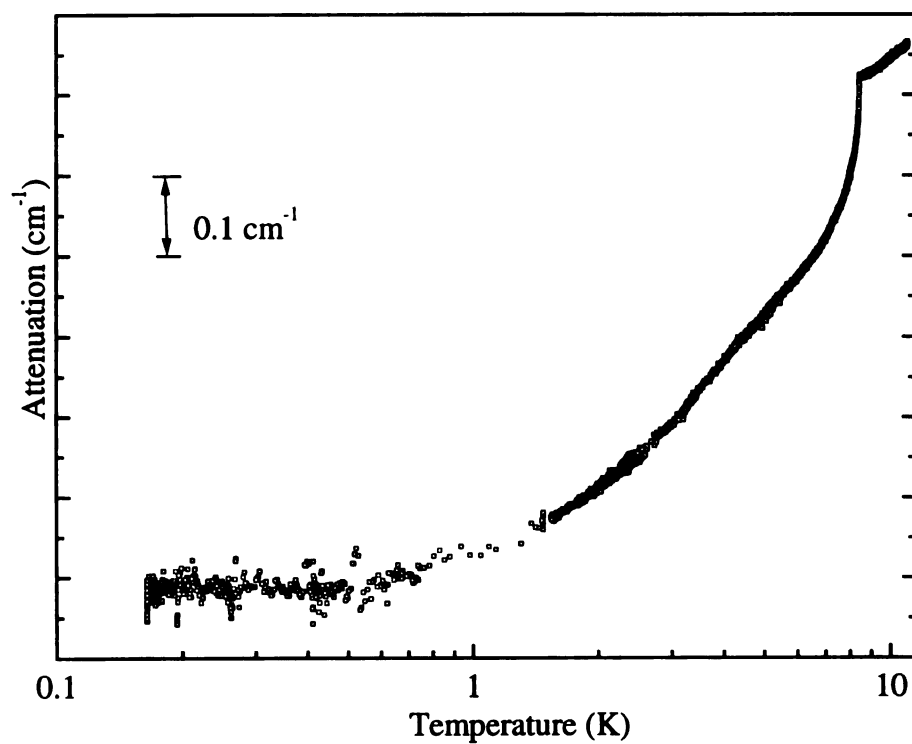


Figure 4.8. Log plot of change in attenuation below 11 K.

Figures 4.7 and 4.8 show the change in attenuation for sample A below 11 K. The gap between 1 and 2 K results from difficulties in controlling the Kelvinox in this temperature region.

There are several features to note in Figures 4.7 and 4.8. First of all there is a sudden decrease in the attenuation at  $T_{c,f} = 8.44$  K for Nb. This is expected from the BCS theory of superconductivity. However, if the change in attenuation was due only to the interaction between electrons and phonons, it would be temperature-independent by  $T \approx T_{c,f} / 2$  as the conduction electrons form Cooper pairs. This is not observed, suggesting that there is another interaction present. As we show later, the strongly temperature dependent attenuation is consistent with the presence of tunneling entities in the Nb:H film. Finally, in addition to the drop at  $T_{c,f}$  and temperature dependent attenuation below  $0.5 T_{c,f}$ , there is a slight knee around 4.5 K. This is a hint of a broad relaxational peak also arising from tunneling and will be further discussed in Chapter V.

#### IV.3.iii Change in attenuation below 11 K, Run 4.15

The sudden drop at  $T_{c,f}$  and knee also are apparent in Run 4.15, as shown in Figures 4.9 and 4.10. Unfortunately, the temperature scale for this run was not firmly established, leading us to place less weight on these results. However, one noticeable difference between the two runs is the different temperature dependence of the attenuation above  $T_{c,f}$ . This temperature dependence has been noted in another study.<sup>2</sup>

The overall change in attenuation between 2 K and  $T_{c,f}$  in Run 4.15 was  $(0.45 \pm 0.01)$   $\text{cm}^{-1}$ , smaller than the  $0.51 \text{ cm}^{-1}$  found for Run 4.16. If we make a background subtraction, so that the normal attenuation is temperature-independent, for Run 4.16 we

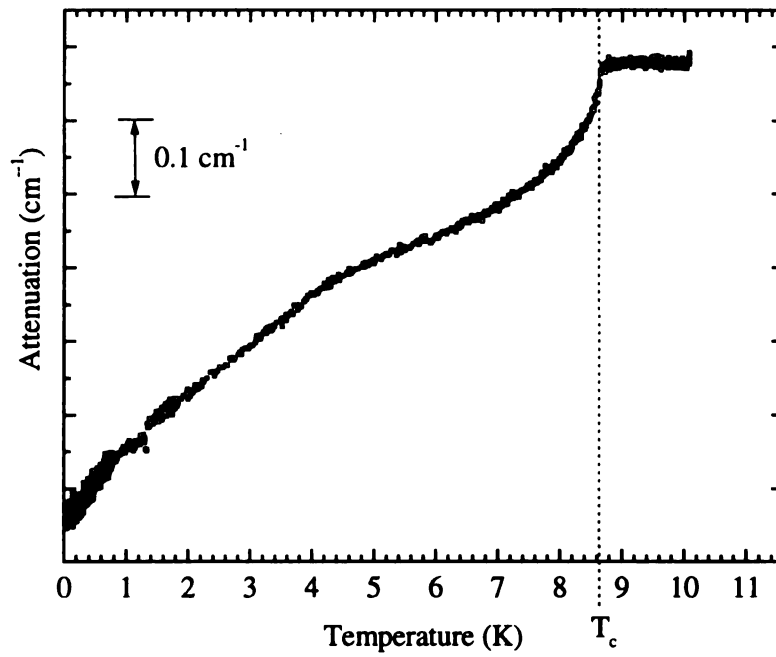


Figure 4.9. The change in attenuation during Run 4.15.

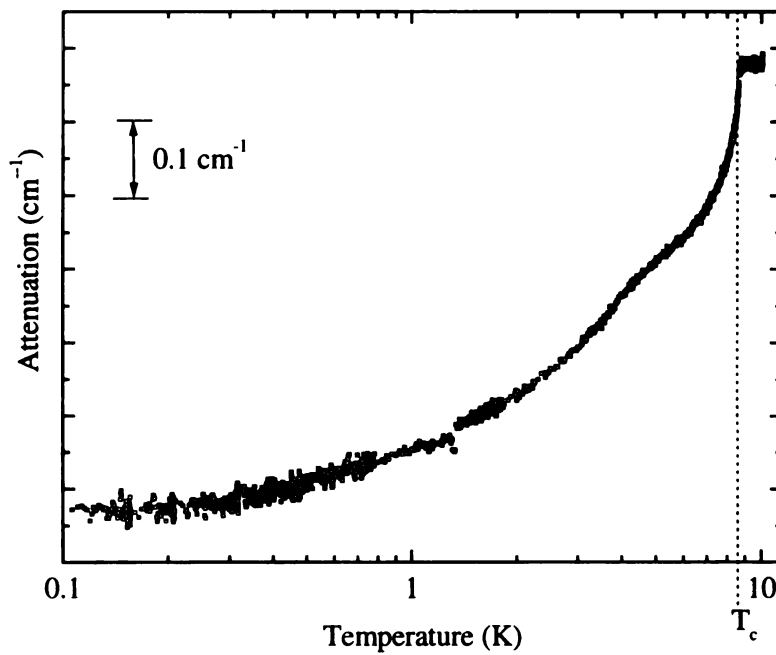


Figure 4.10. The change in attenuation in Run 4.15 on a log-linear plot.

find a change in attenuation between 2 K and  $T_{c,f}$  of  $(0.40 \pm 0.01) \text{ cm}^{-1}$ . The lack of agreement may reflect physical differences between the films studied in the two runs.

#### IV.3.iv Search for nonlinear propagation below 1K.

We looked for nonlinear attenuation below 1 K by varying the acoustic power in the Nb:H and measuring the corresponding change in the attenuation of the acoustic path. If the standard model applied to Nb:H is correct, there are no states below  $\Delta_0$ , approximately 1K. Thus there should be no attenuation due to tunneling states below 1K. However, evidence of states with energies less than  $\Delta_0$  has been observed in pulse echo experiments on Nb:D.<sup>3</sup> If low energy states do exist, the attenuation below 1K would be due to resonant phenomena. These resonant tunneling systems may all be saturated (the same number of tunneling systems are in the excited as ground state) in which case the

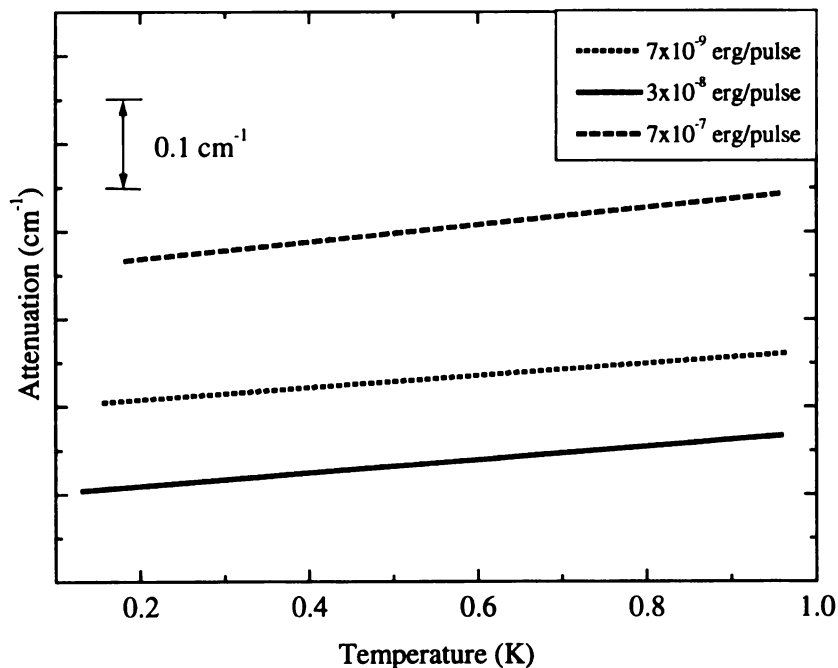


Figure 4.11. The change in attenuation for 3 different input powers. The attenuation has been normalized by the input power. ( $0.1 \text{ cm}^{-1} = 0.131 \text{ dB}$ ).

attenuation is temperature independent. Unsaturated resonant attenuation will increase with decreasing temperature varying as  $\tanh(\hbar\omega/2k_B T)$ .

The power into the Nb:H was varied by changing the variable attenuator before the generator. Lines were fit to the data and are presented in Figure 4.11. The lowest power signal, which corresponded to approximately 9 nW per pulse into the Nb, was barely detectable above the background. Two features to note are that all three signals had the same temperature dependence and decreased with temperature rather than increasing. If the system is linear, the curves should coincide. Also, if we are unsaturating the attenuation should decrease with input power. Since neither is the case, the uncertainty of the measurement of the normalized power is greater than the separation of the curves and the tunneling systems are still saturated at the lowest power.

#### IV.4 Discussion of the behavior near $T_{c,f}$

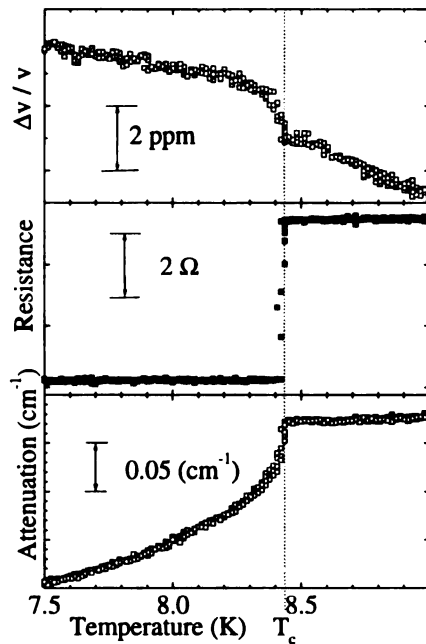


Figure 4.12. The change in the velocity, resistance, and attenuation near  $T_{c,f}$  from Run 4.16.

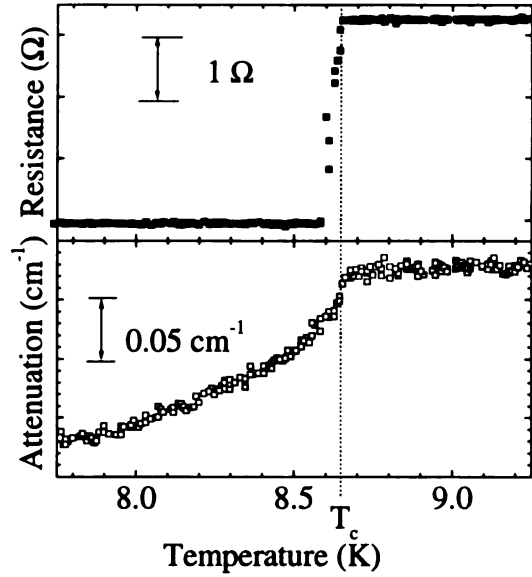


Figure 4.13. The change in the resistance and attenuation near  $T_{c,f}$  in Run 4.15.

Figure 4.12 is the velocity resistance and attenuation near  $T_{c,f}$  for Run 4.16. All three exhibit an abrupt change at  $T_{c,f}$ ,  $8.437 \pm 0.007$ . The velocity had a discontinuity which will be discussed further in V.3. The attenuation begins to drop rapidly at  $T_{c,f}$  due to the superconducting gap beginning to open and the electrons forming Cooper pairs and thus no longer interacting with the phonons. The same drop in the attenuation at  $T_{c,f}$  was observed in Run 4.15 as shown in Figure 4.13.

#### IV.5 Magnetic field data

In order to further explore the interactions of electrons with the tunneling systems, we applied a magnetic field perpendicular to the Nb:H film as shown in Figure 4.14. In the data taken with a 1 T field, it appears that the knee at  $H = 0$  has disappeared.

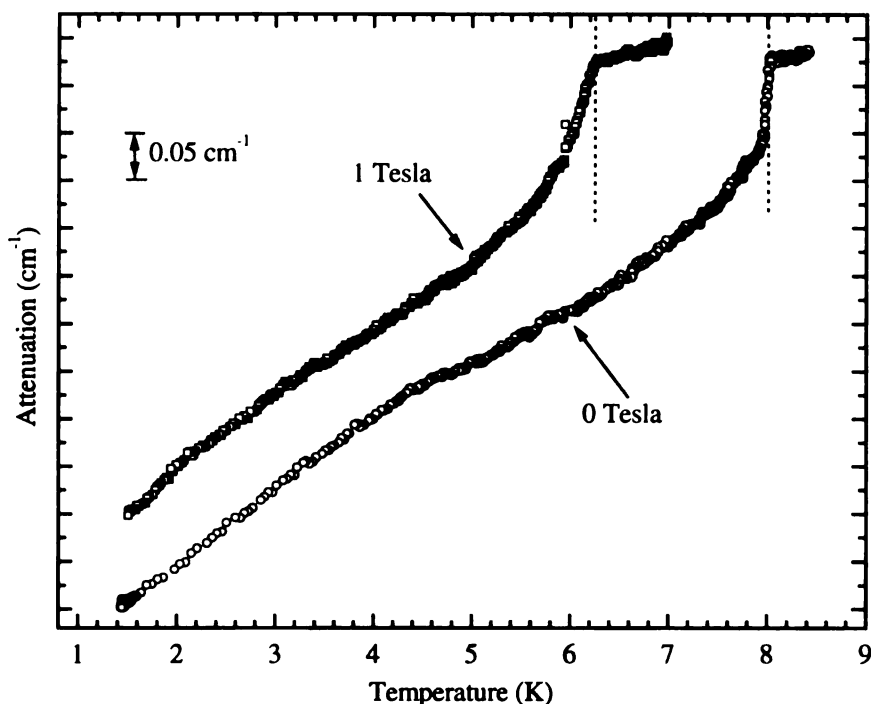


Figure 4.14. The change in attenuation as a function of temperature with and without an applied magnetic field. The dotted lines represent the  $T_{c,f}$  of the resistive sample. The temperatures are approximately 0.5 K too low.

In Figure 4.15 the field was ramped to 2 T at a fixed temperature of  $5.5 \pm 1$  K. The uncertainty in absolute temperature arises from a thermometer bridge malfunction discovered subsequent to the run.

The main item to note in Figure 4.15 is the jump in the velocity right below  $H_{c2}$  which is  $4.5 \pm 1$  ppm in the ramp up and  $3 \pm 1$  ppm in the ramp down. This indicates that the jump observed in the zero field velocity is due to the electrons which interact with the something in the Nb, which we will show to be tunneling systems in Chapter V, beginning to form Cooper pairs. Also, both the velocity and attenuation curves show hysteresis and a broader feature than the resistance.

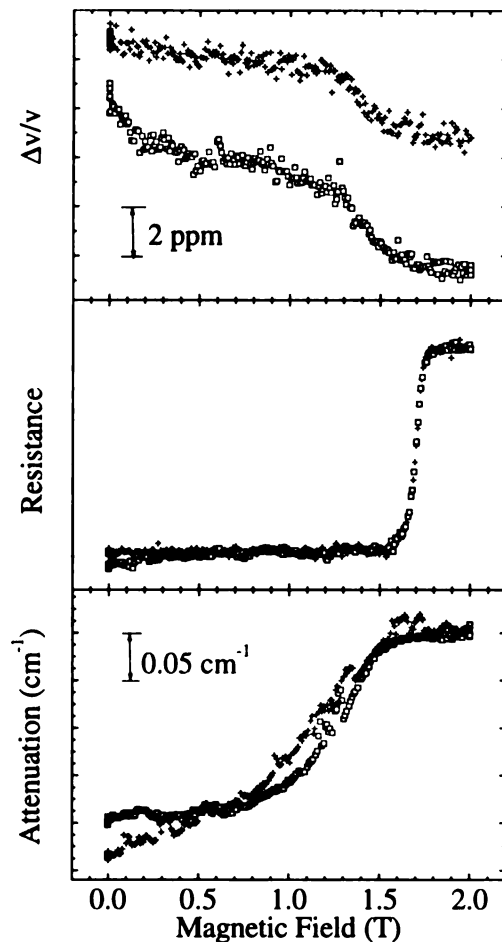


Figure 4.15. Effect of magnetic field at 5.5 K.  $\square$ , field increasing;  $+$ , field decreasing.

---

<sup>1</sup> *Surface-Wave Devices for Signal Processing*, by D.P.Morgan (Elsevier Science Publishing Co, New York, 1985) p. 152.

<sup>2</sup> "From low to high ( $T_c$ ): an ultrasonic investigation of niobium single crystal and YBaCuO superconducting thin films with surface acoustic waves", H.P. Baum, Ph.D. thesis, University of Wisconsin-Milwaukee (1990).

<sup>3</sup> B. Golding, (private communication).

## V. Discussion

### V.1 Qualitative discussion of results

The principal experimental results to be explained in this chapter are shown in Figure 5.1. In the velocity results, we need to understand the jump at  $T_{c,f}$ , the maximum at 3.3 K, and the rapid decrease to the lowest temperatures measured.

At the superconducting transition of the Nb:H, the acoustic attenuation exhibits a

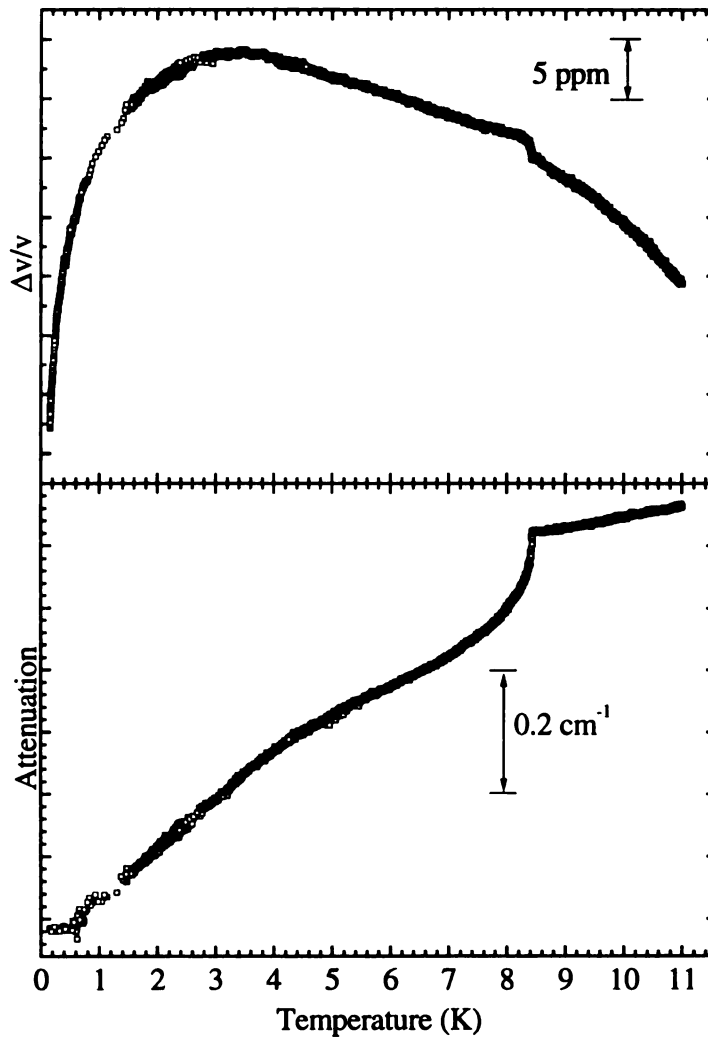


Figure 5.1. The change in attenuation and velocity; 3 mm Nb:H sample in Run 4.16.

sudden drop. If the attenuation were solely due to the electron-phonon interaction, it would be temperature-independent below 3 K. We observe a knee at 4.5 K followed by a strong, relatively linear, temperature-dependent decrease of the attenuation. It appears that the attenuation becomes relatively temperature-independent below 0.6 K.

## V.2. Tunneling systems in Nb:H

As stated in Chapter II, we shall attempt to explain much of our observations by constructing a quantitative model based on acoustic interactions with hydrogen tunneling states in Nb:H. We shall assume that tunneling originates in hydrogen trapped at tetrahedral interstitial sites of the Nb in the vicinity of octahedral impurities. Two tetrahedral sites have nearly degenerate energies so that hydrogen tunneling is possible at low temperatures. These tunneling systems can be described by an asymmetry energy  $\Delta$  and a tunneling matrix element,  $\Delta_0$ . Since the tunneling systems are formed by random point defects, the asymmetry is described by a Lorentzian distribution of width  $W$ , centered at  $\Delta = 0$ . The tunneling matrix element  $\Delta_0$  is assumed to be single-valued. This results in a density of states which is sharply peaked at  $\Delta_0$ , has a high energy tail, and no states below  $\Delta_0$ .

The aforementioned model has been used to describe the change in attenuation and velocity of *single crystal* Nb:N:H using a small value of the deformation parameter,  $\gamma = 0.023\text{eV}$ .<sup>1</sup> Applying a similar approach, we find that the standard model with small  $\gamma$  can fit the  $\Delta v/v$  data quite well. However, the same parameters do not fit the attenuation even qualitatively as they predict no change in attenuation below 2 K. We suggest that this discrepancy can be resolved by formulating the presence of additional strongly coupled

tunneling entities.

### V.2.i Velocity and attenuation dependence on parameters

Before constructing a quantitative model that explains our data, we shall present some illustrative examples of the dependence of the attenuation and velocity on tunneling model parameters. This is useful because the calculations involve numerical integration over energy and cannot be solved analytically.

The velocity shown in Figures 5.2-5.6 is the sum of the resonant and relaxation change in velocity, Eq. 2.10 and Eq. 2.13, integrated over a Lorentzian distribution in  $\Delta$ ,

$$\begin{aligned} \left(\frac{\Delta v}{v}\right)_{\text{res}} + \left(\frac{\Delta v}{v}\right)_{\text{rel}} = & - \int_{-\infty}^{\infty} n(\Delta) \frac{\gamma^2}{\rho v^2} \left(\frac{\Delta_0}{E}\right)^2 \frac{1}{E} \tanh\left(\frac{E}{2k_B T}\right) d\Delta \\ & - 2 \int_0^{\infty} n(\Delta) \frac{\gamma^2}{2\rho v^2} \frac{1}{k_B T} \left(\frac{\Delta}{E}\right)^2 \frac{1}{1 + \omega^2 T_1^2} \text{sech}^2\left(\frac{E}{2k_B T}\right) d\Delta \end{aligned} \quad (5.1)$$

The attenuation is given by Eq. 2.12 integrated over the same distribution and does not include attenuation due to the electron-phonon interaction,

$$\alpha_{\text{rel}} = 2 \int_0^{\infty} n(\Delta) \frac{\gamma^2}{\rho v^3} \frac{1}{k_B T} \left(\frac{\Delta}{E}\right)^2 \frac{\omega^2 T_1}{1 + \omega^2 T_1^2} \text{sech}^2\left(\frac{E}{2k_B T}\right) d\Delta \quad (5.2)$$

All of the plots shown below were generated using the  $E \rightarrow 0$  expression for the tunneling system electronic relaxation rate in the superconducting state, Eq. 2.9, to save computational time. For niobium with  $T_{c,f} = 8.437$  K and  $E / k_B > 1.5$  K, the low energy electronic relaxation rate results begin to deviate above 7 K from those calculated using the full electronic rate. Therefore only the calculated curves below 7 K and above  $T_{c,f}$  are shown. We used the values:  $T_{c,f} = 8.437$  K,  $v = 3.1 \times 10^5$  cm/s,  $\omega/2\pi = 690$  MHz, and  $n_0 \gamma^2 / \rho v^2 k_B \pi = 10^{-4}$  K.

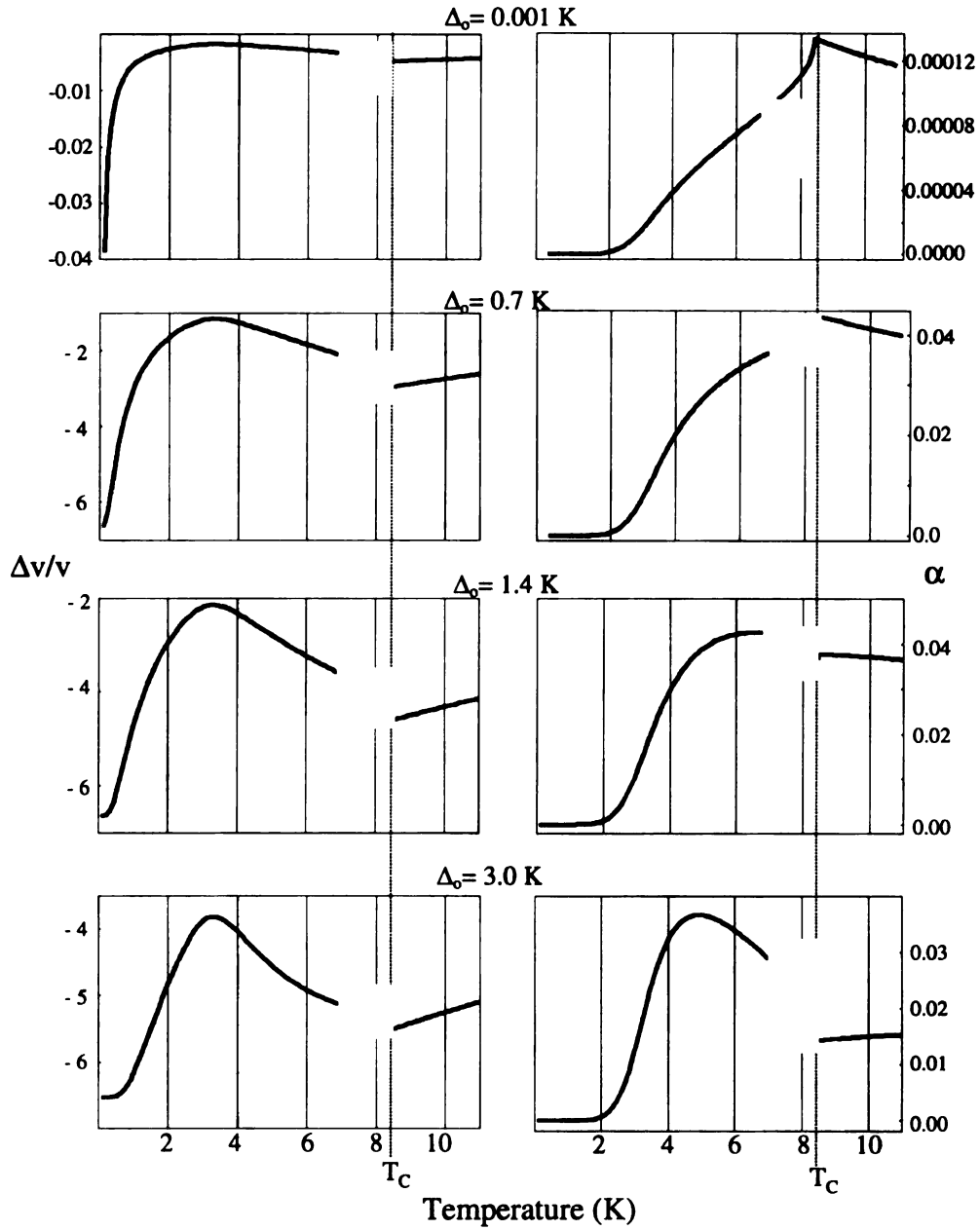


Figure 5.2. Plot of  $\Delta v/v$  and attenuation using Eq. 5.1 and 5.2 with several values of  $\Delta_0$ . Tunneling parameters are:  $W / k_B = 30$  K,  $\gamma = 0.023$  eV,  $K = 0.15$  and  $\omega = 4.3 \times 10^9 \text{ s}^{-1}$ .

In Figure 5.2 the dependence on the tunneling matrix element  $\Delta_0$  was studied. As  $\Delta_0$  becomes larger the relaxation rates increase. This results in the condition  $\omega = T_1$  being met at lower temperatures and thus the peak in the relaxation velocity shifting to lower

temperatures. In addition the hyperbolic tangent in the resonant velocity and the hyperbolic secants in the relaxational velocity and attenuation have a stronger temperature dependence.

In Figure 5.3 the electron-tunneling system coupling  $K$ , was varied. Increasing  $K$  increases the electronic relaxation rate. Thus the electronic relaxation will be greater than the phonon relaxation rate at lower temperatures and the peak of the velocity will shift to

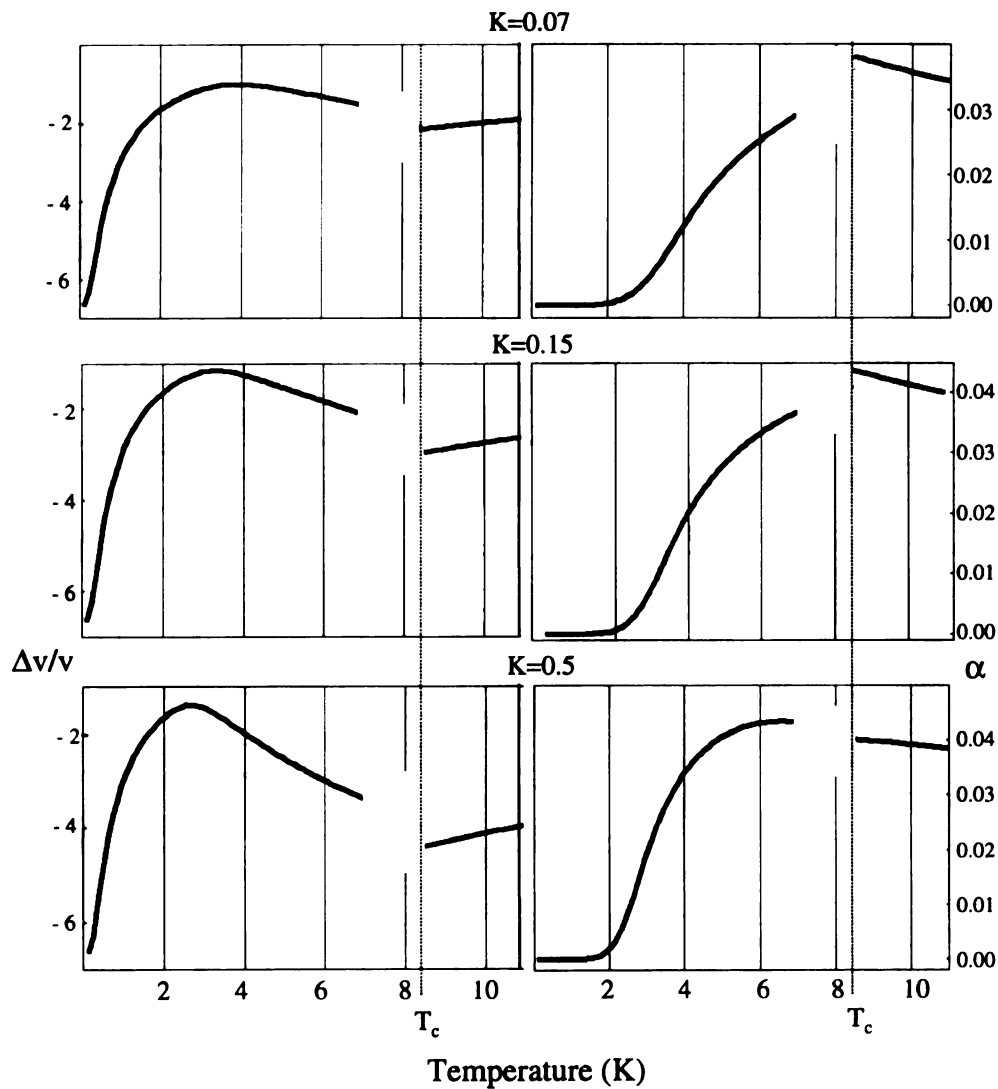


Figure 5.3. Plot of  $\Delta v/v$  and attenuation using Eq. 5.1 and 5.2 with several values of  $K$ . For all plots  $\Delta_0 / k_B = 0.7$  K,  $W / k_B = 30$  K,  $\gamma = 0.023$  eV, and  $\omega = 4.3 \times 10^9 \text{ s}^{-1}$ .

lower temperatures. In addition, the slope of the relaxational change in velocity will increase. The peak in the attenuation at  $\omega = T_1$  will also shift to lower temperatures as  $K$  is increased. Note that  $K = 0.5$  represents the maximal value for the coupling.

The phonon-tunneling system coupling was varied in Figure 5.4. For these calculations  $(n_0 \gamma^2 / \rho v^2)$  was held constant. The value,  $\gamma = 1$  eV, is a coupling on the order of that found in metallic glasses. The curves changed only slightly at low temperatures as  $\gamma$  was varied by over 2 orders of magnitude. The attenuation is

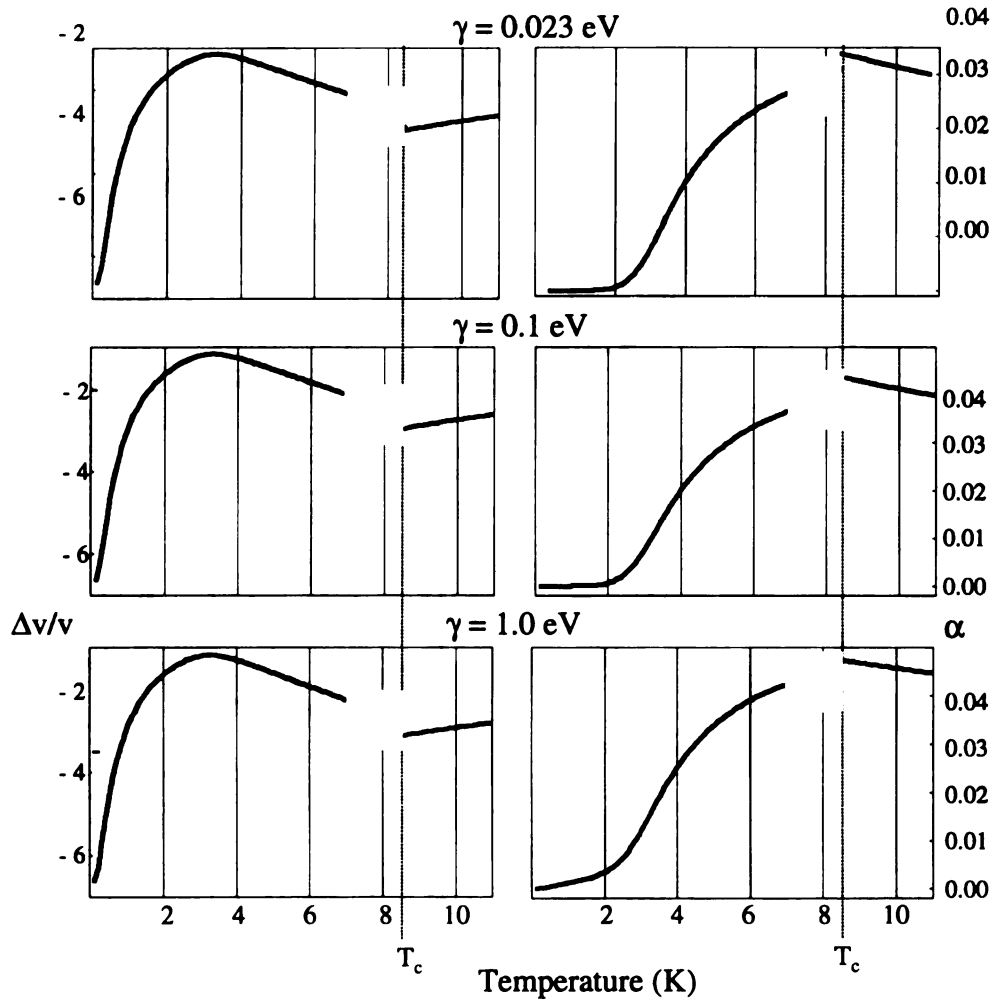


Figure 5.4. Plot of  $\Delta v/v$  and attenuation using Eq. 5.1 and 5.2 with several values of  $\gamma$ . For all graphs,  $\Delta_0 / k_B = 0.7$  K,  $W / k_B = 30$  K,  $K = 0.15$ , and  $\omega = 4.3 \times 10^9 \text{ s}^{-1}$ .

temperature-independent below 2 K until  $\gamma$  is on the order of an eV.

Figure 5.5 is a compilation of calculations in which the width of the Lorentzian distribution of  $\Delta$  was varied. The high temperature velocity slope due to the relaxational interaction becomes comparable (but of opposite sign) to the low temperature resonant velocity's slope with increasing width. The attenuation peak, occurring at  $\omega T_1 = 1$ , becomes wider as the distribution of energies and thus relaxation times increases in width. Note that there is very little difference between the shape of the curves with  $W/k_B$

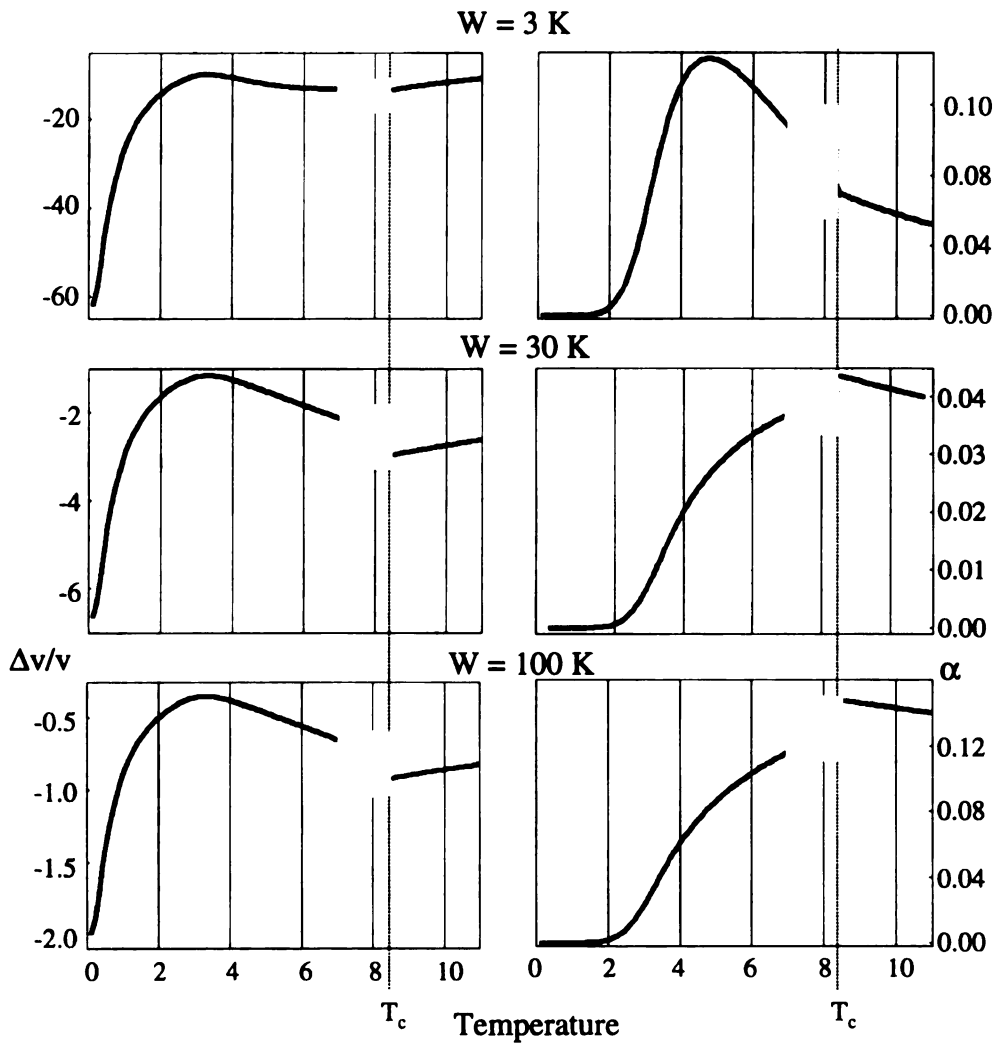


Figure 5.5. Plot of  $\Delta v/v$  and attenuation using Eq. 5.1 and 5.2 several values of  $W$ . For all figures,  $\Delta_0/k_B = 0.7 \text{ K}$ ,  $\gamma = 0.023 \text{ eV}$ ,  $K = 0.15$ , and  $\omega = 4.3 \times 10^9 \text{ s}^{-1}$ .

= 30 K and  $W / k_B = 100$  K. A larger width results from interactions between the defects at high concentrations of tunneling systems.<sup>2,3</sup>

Most previous work has assumed that the tunneling matrix element  $\Delta_0$  is constant in Nb:H. This assumption implies that all of the tunneling objects are in the same environment, i.e.  $d$  and  $V$  are single-valued. Thus, they must be formed by a single species of octahedral impurities, or different species which cause the same distortions in the potential energy surface about the trapped hydrogen. In addition, due to its dependence on mass, a constant  $\Delta_0$  also means that there is only one type of tunneling object.

A Lorentzian distribution of  $\Delta_0$ , has been invoked before in the  $\text{NbH}_x(\text{O,C,N})_y$  system. The width of the distribution was quite narrow,  $\approx 1\text{K}$ .<sup>4,5</sup> Figure 5.6 is a plot of the velocity and attenuation with and without a Lorentzian distribution of  $\Delta_0$ . The curves from the distributed  $\Delta_0$  were multiplied by 0.325 so that the shapes of the curves could be more easily compared. Adding a distribution to the tunneling matrix element broadened

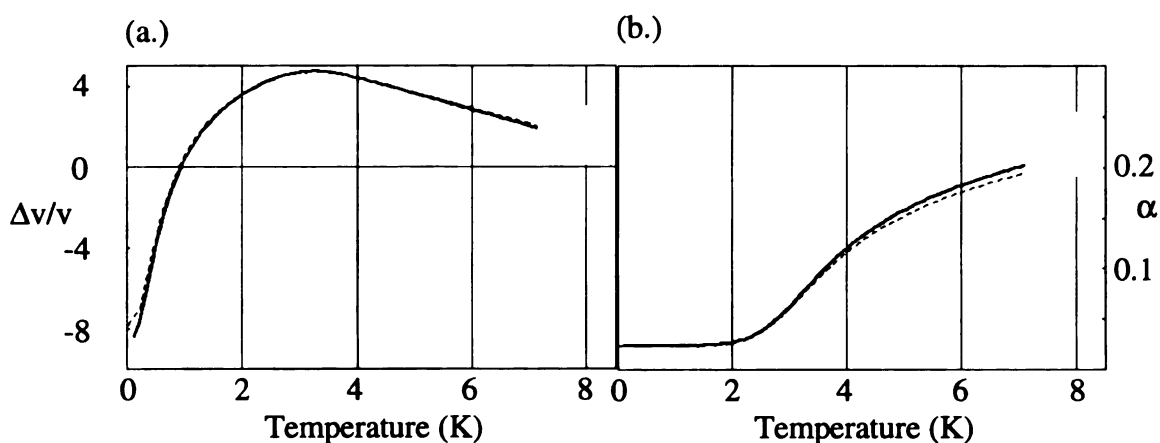


Figure 5.6. Effect of a narrow distribution of  $\Delta_0$  on velocity and attenuation due to tunneling. Solid line;  $\Delta_0 = 0.71$  K; dashed line; distribution of  $\Delta_0$  of width 1 K.  $W / k_B = 140$  K,  $\gamma = 0.023$  eV,  $K = 0.17$ , and  $\omega = 4.3 \times 10^9 \text{s}^{-1}$ .

the velocity peak and slightly flattened the attenuation peak but did not change the overall shape very much. The attenuation below 2 K was not increased as the relaxation rates were too slow to relax any additional tunneling systems.

### V.3 The polycrystalline data described by the standard tunneling model.

#### V.3.i Method for fitting the standard model to the Nb:H film data

We assume that the velocity and attenuation can be described by,

$$\left(\frac{\Delta v}{v}\right) = \left(\frac{\Delta v}{v}\right)_{\text{TLS}} + \left(\frac{\Delta v}{v}\right)_{\text{anh}} \quad (5.3)$$

$$\alpha = \alpha_{\text{TLS}} + \alpha_{\text{BCS}} + \alpha_{\text{Back}} \quad (5.4)$$

where  $(\Delta v/v)_{\text{TLS}}$  is equal to Eq 5.1,  $(\Delta v/v)_{\text{anh}} = \beta T^2 + \eta T^4$  where  $\beta$  and  $\eta$  are constants and is due to lattice anharmonicity,  $\alpha_{\text{TLS}}$  is given by Eq 5.2,  $\alpha_{\text{BCS}}$  is given by Eq. 3.6, and  $\alpha_{\text{Back}}$  allows for a background attenuation.

Since  $(\Delta v/v)_{\text{anh}}$  is only weakly temperature-dependent, we initially set it to zero and fit the polycrystalline Nb:H velocity. The parameters derived from this fit are then used to calculate  $\alpha_{\text{TLS}}$  and the amplitudes of  $\alpha_{\text{BCS}}$  and  $\alpha_{\text{Back}}$  adjusted to best fit the polycrystalline Nb:H data.

It is tedious to do a standard nonlinear least squares fit to the velocity data since the velocity calculation involves numerical integration over the asymmetry energies. Thus the velocity data were fit by minimizing the sum of squared differences between representative data points and calculated values for the velocity. These representative data points were spaced at intervals of 0.5 K except at the peak where two points were

used to describe the curvature, and in the final fit where a point was placed at both the top and the bottom of the jump near  $T_{c,f}$ . In order to judge the dependence of the fit on the low temperature data, the range of data at the low temperature end was varied. The matrix element,  $\Delta_0$ , Lorentzian width,  $W$ , electron-tunneling system coupling,  $K$ , velocity amplitude, i.e. density of tunneling systems, and offset varied to minimize the residuals. As discussed in V.2.i, the velocity's dependence on the phonon-tunneling system coupling is quite weak unless it is on the order of 1 eV. Thus it was fixed at 23 meV. The  $E \rightarrow 0$  electronic relaxation rate was used. This approximation is inaccurate near  $T_{c,f}$ . The following constants were used: the phonon-tunneling system coupling  $\gamma = 0.023$  eV,  $v_N = 3200$  m/s,  $\omega = 2\pi \times 690$  MHz,  $\rho = 8.58$  g/cm<sup>3</sup>, and  $T_{c,f} = 8.437$  K. The BCS gap was calculated by interpolating between the values given by Mühlischlegel.<sup>6</sup>

Once the “best fit” values were found using the low-energy electronic relaxation rate,  $(\Delta v/v)_{\text{TLS}}$  and  $\alpha_{\text{TLS}}$  were recalculated with the full electronic relaxation rate. In order to describe the Nb:H film attenuation, the amplitudes of  $\alpha_{\text{BCS}}$  and  $\alpha_{\text{Back}}$ , which was assumed temperature-independent, were adjusted. The amplitude of  $\alpha_{\text{BCS}}$  is the normal attenuation due to the electron-phonon interaction,  $\alpha_n$  from Eq. 3.6.

The quality of fit was judged by how well the velocity calculated with the full electronic relaxation rate described the jump at  $T_{c,f}$  and the rest of the velocity data. The jump at  $T_{c,f}$  is due to the rapid change in  $T_{1,el}^{-1}$  as the electrons form Cooper pairs. It cannot be due to the acoustoelectric effect, which was introduced in Chapter III, since the acoustoelectric effect causes a decrease on the order of  $10^{-6}$  ppm in the velocity as the film becomes superconducting.

### V.3.ii. Fits to the standard Nb:H tunneling model

The best fit tunneling parameters to the Nb:H film data velocity data are  $\Delta_0/k_B = 0.567$  K,  $W/k_B = 18$  K,  $K = 0.189$  and  $n_0 = 8.92 \times 10^{19} \text{ cm}^{-3}$  which corresponds to a tunneling hydrogen concentration of 0.16 at. %. These values were found when the largest range of data (0.2 K to  $T_{c,f}$ ) was used and included a representative data point above the jump at  $T_{c,f}$ . It is difficult to assign an uncertainty to the “best fit” parameters. We estimate  $\Delta_0$  and  $K$  to have an uncertainty of about 10% while  $W$  and  $n_0$  are known within a factor of 2 as the fit is insensitive to  $W$  and  $n_0$ .

Figure 5.7 shows the velocity data and calculations using the “best fit” parameters. The calculation with the approximate electronic relaxation rate describes the data quite well. As shown in the inset, the inaccuracies inherent in the approximate electronic

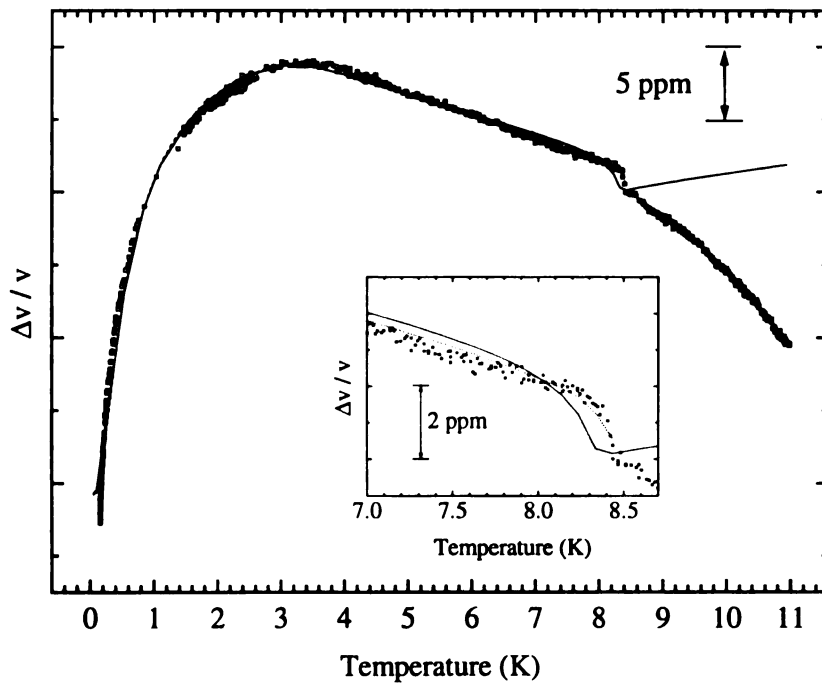


Figure 5.7  $(\Delta v/v)_{\text{TLS}}$ . Solid line, calculation with the full electronic relaxation rate; dashed line, calculations using the  $E = 0$  approximate electronic rate.

relaxation rate are apparent at  $T_{c,f}$  where the calculation does not match the normal state velocity, calculated from Eq. 2.7. The calculated velocity with the full electronic rate does match up with the normal velocity as it should. The full electronic rate calculation does not describe the data as well as the approximate electronic rate calculation which is not surprising as the fit was done with the approximate electronic rate. The jump is slightly below 8.437 K,  $T_{c,f}$ , and the velocity's value in the linear region above 4 K is slightly higher than that calculated with the approximate relaxation rate. Below the peak near 3.2 K, the approximate and full electronic relaxation rate calculations agree quite well. Above  $T_{c,f}$   $(\Delta v/v)_{\text{TLS}}$  does not describe the data completely as our assumption of  $(\Delta v/v)_{\text{anh}}$  weak temperature dependence becomes inaccurate, as discussed below in V.3.iv.

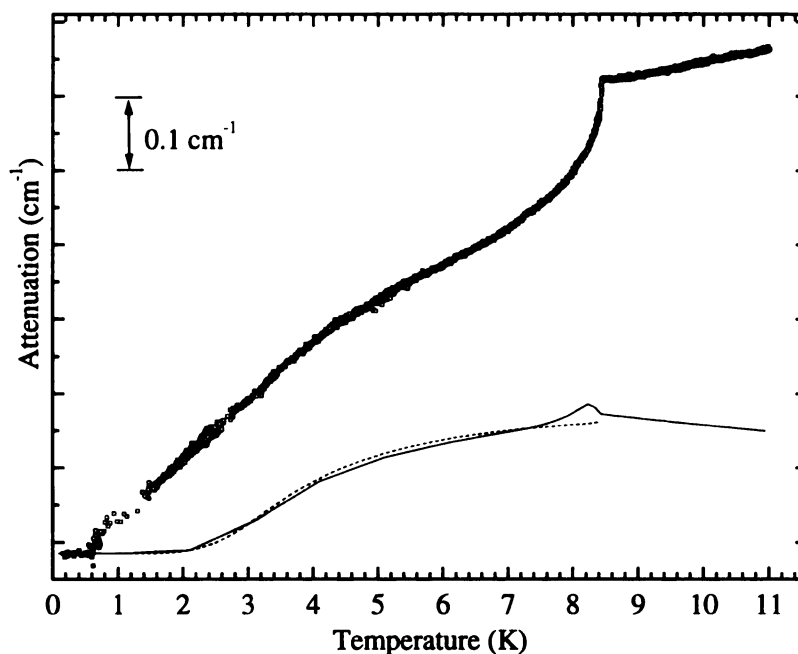


Figure 5.8. Tunneling contribution to the attenuation,  $\alpha_{\text{TLS}}$ , from the full electronic relaxation rate (solid line); calculated with the approximate relaxation rate (dashed line). The measured attenuation, top curve, includes  $\alpha_{\text{BCS}}$ .

In Figure 5.8  $\alpha_{\text{TLS}}$  with the full and  $E = 0$  electronic relaxation rates is shown along with the data. Both calculations exhibit a turnover which follows the knee in the data, fall less steeply below the knee than the data, and are temperature-independent below 2 K. Near  $T_{c,f}$  the two calculations deviate from each other. The full electronic calculation exhibits a small peak which the  $E \rightarrow 0$  approximate rate does not. This peak increases in amplitude with  $\Delta_0$  and in width with the width of the Lorentzian. Again the full electronic calculation meets the normal calculated  $\alpha_{\text{TLS}}$  at  $T_{c,f}$ .

The total attenuation and its contribution with  $\alpha_{\text{Back}} = 0.16 \text{ cm}^{-1}$  are shown in Figure 5.9. The attenuation is fit adequately down to 2 K by Eq. 5.4. But there is additional change in the attenuation below 2 K which is not described by either  $\alpha_{\text{TLS}}$  or  $\alpha_{\text{BCS}}$ . As

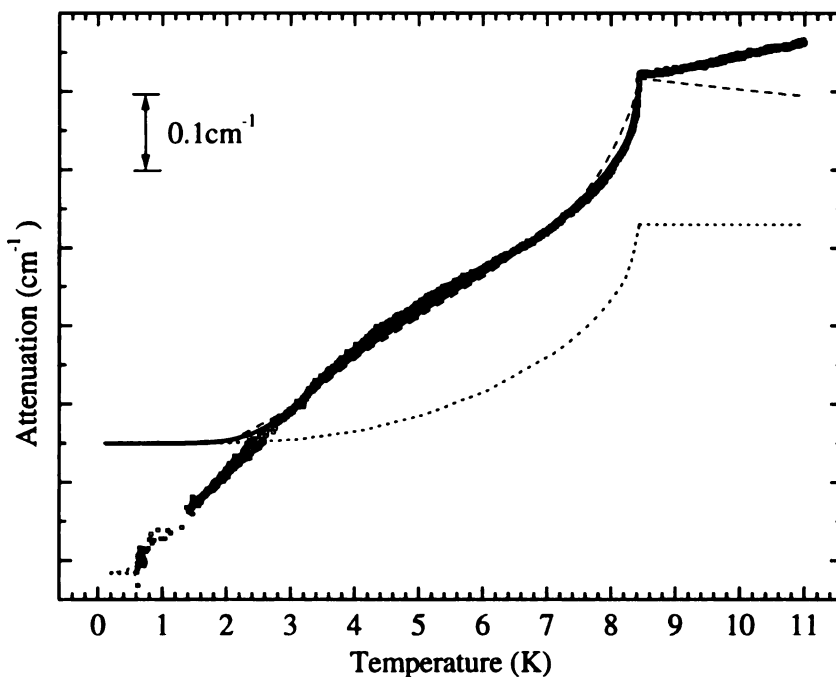


Figure 5.9.  $\Delta_0 / k_B = 0.567 \text{ K}$ ,  $W / k_B = 18 \text{ K}$  and  $K = 0.189$ . Dotted line,  $\alpha_{\text{BCS}}$ ; dashed line,  $\alpha_{\text{TLS}}$  with full relaxation rate summed with  $\alpha_{\text{BCS}}$ ; solid line,  $\alpha_{\text{TLS}}$  with approximate relaxation rate added to  $\alpha_{\text{BCS}}$ . The solid line falls directly on the data below  $T_{c,f}$  and thus the line cannot be seen between 6.5 K and  $T_{c,f}$ .  $\alpha$  is assumed equal to zero at 0.2 K.

with the velocity, the  $E \rightarrow 0$  relaxation rate attenuation is a better fit. For the  $\alpha_{\text{BCS}}$  calculation  $\alpha_n = 0.28 \text{ cm}^{-1}$ .

$\alpha_n$  in conjunction with the resistivity of the Nb film can be used to determine the factor  $F(v)$  of Eq. 3.5. Using the resistivity of the film just above  $T_{c,f}$ , the electron mean free path can be calculated from the free electron expression<sup>7</sup>

$$l_e = \frac{mv_F}{Ne^2\rho_{8.5K}} \quad (5.5)$$

where  $m$  is the electron mass,  $9.1 \times 10^{-28} \text{ g}$ ,  $v_F$  is the Fermi velocity,  $1.4 \times 10^8 \text{ cm/s}$ ,  $N$  is the electron density,  $5.6 \times 10^{22} \text{ cm}^{-3}$ ,  $e$  is the electronic charge,  $1.6 \times 10^{-19} \text{ C}$ , and  $\rho_{8.5K}$  is the resistivity at 8.5K,  $12.3 \pm 0.5 \mu\Omega\text{-cm}$ . Eq. 5.5 yields a value for  $l_e$  of  $71 \text{ \AA}$ . Substituting this value along with  $\omega = 4.335 \times 10^9 \text{ s}^{-1}$ ,  $\rho_{\text{substrate}} = 4.65 \text{ g/cm}^3$ ,  $v_s = 3.2 \times 10^5 \text{ cm/s}$ ,  $q = 1.35 \times 10^4 \text{ cm}^{-1}$ ,  $h = 2915 \text{ \AA}$  and  $\alpha_n = 0.28 \text{ cm}^{-1}$  into Eq. 3.5 one finds that  $F(v)$  is 1.2. This is larger than any of the cited values for  $F(v)$  which range from  $0.022^8$  to  $0.455^9$ .

### V.3.iii Comparison of Nb:H film and single crystal tunneling parameters.

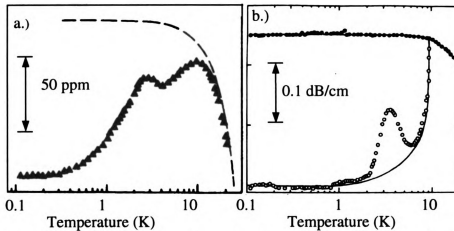


Figure 5.10. Single crystal  $\text{NbN}_{0.0015}\text{H}_{0.003}$  data from Ref (1). a.) velocity, the dashed line is hydrogen free data b.) attenuation, the solid line is hydrogen free data,  $\bullet$  is in the normal state, and  $\circ$  data is from the superconducting state.

The tunneling parameters obtained for Nb:H films differ from those determined from acoustic measurements in single crystal Nb:H.<sup>1</sup> The latter experiments were carried out with NbN<sub>0.0015</sub>H<sub>0.003</sub> crystals at 30, 90 and 150 MHz between 0.1 and 20 K. These results are shown in Figure 5.10. The tunneling resonant change in velocity is similar to the Nb:H polycrystalline film; temperature-independent below 0.2 K, rising to a peak just below 3 K. Unlike the Nb:H film, the tunneling relaxational change in velocity passes through a minimum and then rises to another peak near T<sub>c</sub>. This shape is indicative of a narrow distribution of asymmetries. The relaxation peak in the attenuation occurs at near 3.5 K and is much more prominent in single crystals than in the polycrystalline films. Morr et al.<sup>1</sup> fit the velocity using the approximate electronic relaxation rate and found  $\Delta_0 = 1.4$  K and  $W = 3$  K. By assuming that the concentration of tunneling systems was equal to the N concentration, they derived a phonon tunneling system coupling  $\gamma$  of 23 meV. From the attenuation, they then derived an electron-tunneling system coupling  $K = 0.07$ . Using our fitting programs we were able to duplicate their fits if we used a velocity

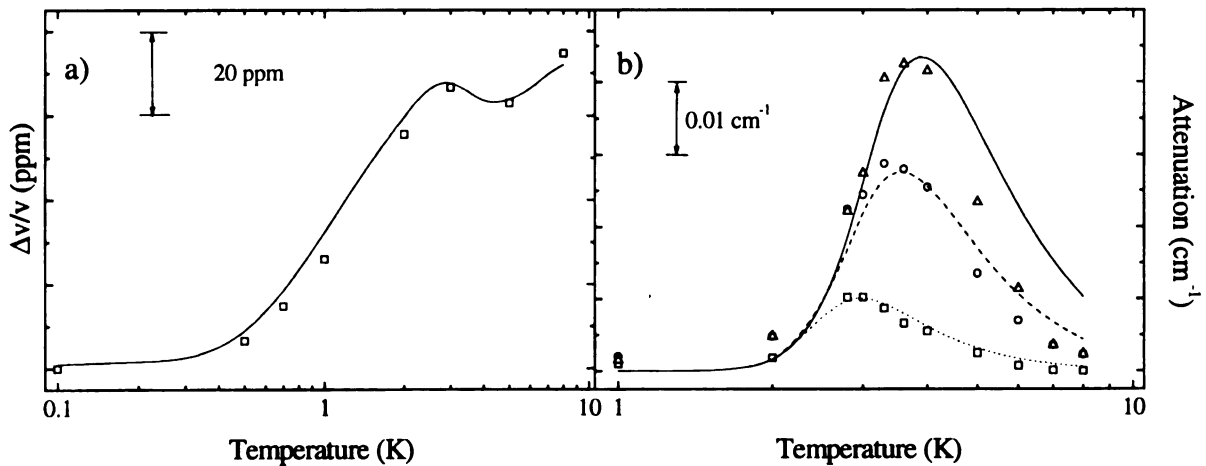


Figure 5.11 Single crystal Nb:N:H data from Ref.(1) with our calculations (lines). a)  $\Delta v/v$  at 90 MHz (with no anharmonic correction). b) attenuation (hydrogen free Nb background subtracted).  $\Delta$ ,  $\omega/2\pi = 150$  MHz;  $\circ$ ,  $\omega/2\pi = 90$  MHz;  $\square$ ,  $\omega/2\pi = 30$  MHz.

of  $4.16 \times 10^5$  cm/s; see Figure 5.11. Note that the attenuation below 2 K still is temperature dependent, especially in the high frequency data, which is not accounted for in the fit.

The value for the tunneling matrix element found in Ref. (1) is slightly lower than the  $2.0 \pm 0.2$  K found in other niobium experiments with nitrogen and hydrogen impurities.<sup>10,11,12,13</sup> From Appendix D, we can conclude that  $\Delta_0$  varies between 1.4 and 3.1 K for C, N, or O impurities. Also, the tunneling matrix element is smaller if the octahedral impurity is N or C rather than O. Our value for the tunneling matrix element in the polycrystalline film is lower than all of the previous experiments.

To see if our data could be described by  $\Delta_0 = 1.4$  K,  $\Delta_0$  was fixed and the fitting routine performed. Taking  $\gamma = 0.023$  eV, the parameters  $W = 25.9$  K,  $K = 0.147$ , and  $n_0 =$

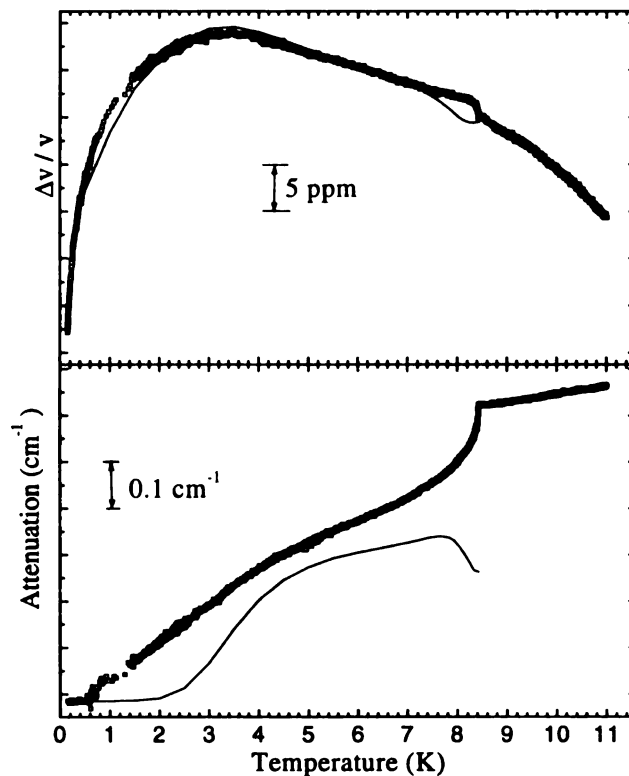


Figure 5.12. Our data along with the best fit with  $\Delta_0$  fixed at 1.4 K. Solid line is  $(\Delta v/v)_{\text{TLS}}$  and  $\alpha_{\text{TLS}}$  (see text).

$9.7 \times 10^{20} \text{ cm}^{-3}$  were found. As is apparent in Figure 5.12, this fit is poor.

For the polycrystalline Nb:H we find a width  $W = 18.5 \text{ K}$ , significantly larger than that found in single crystal Nb:H. However it is well within the range found in neutron scattering and specific heat experiments with polycrystals or single crystals with tunneling system concentrations on the order of a tenths of a percent.<sup>13,14,15,16</sup> We find in Nb:H a value for  $K$  twice that found in single crystals.

### V.3.iv Fit after temperature-dependent $(\Delta v/v)_{\text{anh}}$ has been subtracted

In the single crystal acoustic experiments the Nb velocity and attenuation of the Nb prior to H doping were measured. The velocity lattice background is described by  $\beta = -0.003$ .<sup>1</sup> Thus  $(\Delta v/v)_{\text{anh}}$  could be subtracted from the data before it was fit. We could not measure a hydrogen free thin film since the hydrogen in our samples was incorporated during the deposition process. Therefore, an anharmonic background term was estimated by assuming that the temperature dependence of the normal state  $(\Delta v/v)$  was due to  $(\Delta v/v)_{\text{anh}}$  since  $(\Delta v/v)_{\text{TLS}}$  is only weakly temperature-dependent in the normal state. Figure 5.13 (a) shows that a  $T^4$  term is sufficient to describe the normal state velocity.

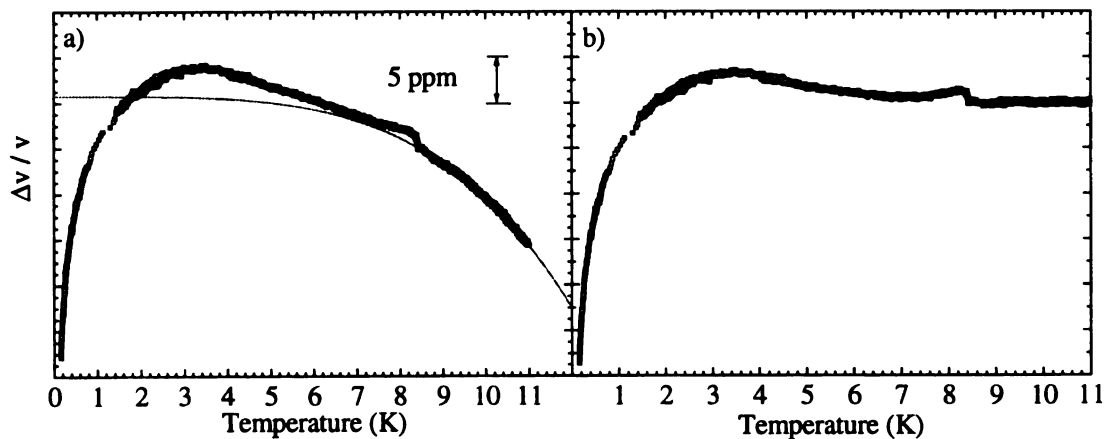


Figure 5.13. a) Anharmonic contribution to the velocity with  $\beta = -0.00112$  (solid line) b)  $\Delta v/v$  with anharmonic background subtracted.

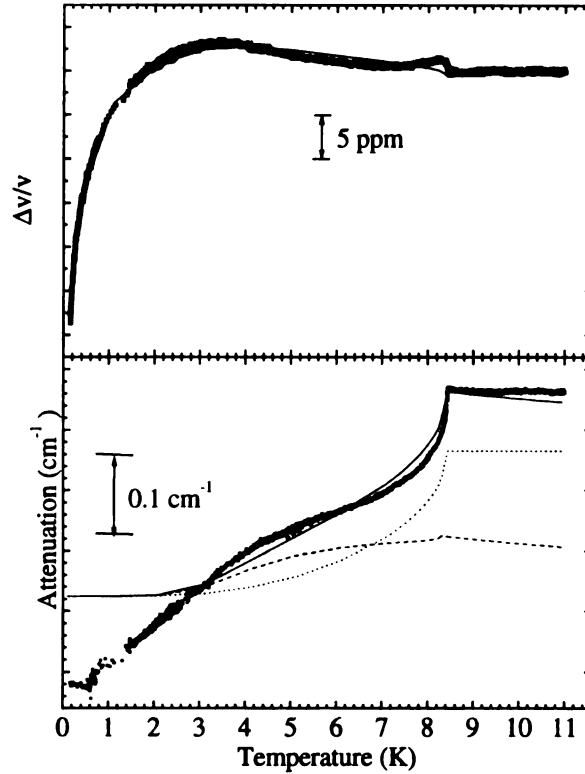


Figure 5.14. Fit to the data after an approximate anharmonicity subtracted. In the upper graph: solid line,  $(\Delta v/v)_{\text{TLS}}$ . In the lower graph the linearized attenuation data; dashed line,  $\alpha_{\text{TLS}}$ ; dotted line,  $\alpha_{\text{BCS}}$  with normal amplitude of  $0.24 \text{ cm}^{-1}$ ; solid line,  $\alpha_{\text{TLS}} + \alpha_{\text{BCS}}$ . All were calculated with the full electronic relaxation rate.

The measured velocity minus the  $(\Delta v/v)_{\text{anh}}$  was then used for the fit. The constants used were  $\gamma = 0.023 \text{ eV}$ ,  $\omega = 4.3 \times 10^9 \text{ s}^{-1}$ ,  $v = 3.2 \times 10^5 \text{ cm/s}$ , and  $T_{c,f} = 8.437 \text{ K}$ . The fit yielded the values,  $\Delta_0 = 0.465 \text{ K}$ ,  $W = 6.79 \text{ K}$ ,  $K = 0.073$ , and  $n_0 = 3.3 \times 10^{19} \text{ cm}^{-3}$  and is shown in Figure 5.14. Note that while the tunneling matrix element remained small,  $K$  is now quite similar to that found in bulk Nb:H samples.

The fit to the velocity is not perfect, however, it does describe the general shape. The calculated attenuation fits the linearized attenuation data much better than the raw data. The linearized attenuation data was created by subtracting  $\alpha_{\text{Back}} = \kappa T$  from the raw data, where  $\kappa$  is chosen so that the normal  $\alpha$  data is temperature independent after subtraction of  $\alpha_{\text{Back}}$ . This is unlike the fit from the parameters derived from the raw data which fit

the attenuation data better with a temperature independent  $\alpha_{\text{Back}}$ . This indicates that the slope above  $T_{c,f}$  is due to anharmonicity. Although this is not a perfect fit, it does indicate that the high electron-tunneling system coupling  $K$  found when fitting to the raw data is probably due to the anharmonicity and not a characteristic of the tunneling systems.

#### V.4 Evidence for anomalous attenuation

The standard tunneling model for Nb:H, with small phonon-tunneling system coupling and lack of states below  $\Delta_0$ , is not able to describe the strong temperature dependence of the relaxational attenuation below 2 K if slow relaxation rates exist below 2 K. The electronic relaxation rate  $T_{1,el}^{-1}$  is  $< 10^6 \text{ s}^{-1}$  below 2 K as most of the electrons are bound in Cooper pairs and thus no longer able to relax the tunneling systems. The phonon coupling is also comparable.

This extra attenuation cannot arise from resonant attenuation since the resonant process is saturated. The situation also cannot be improved by postulating an enhanced number of states at low energies. The data depend linearly on temperature below 2 K, becoming temperature-independent around 0.6 K, in disagreement with the calculated temperature dependence. Thus simply increasing the number of states below 2 K cannot change the temperature dependence.

In order to get attenuation below 2 K with the correct temperature dependence, it is necessary to have a larger relaxation rate. Since the electrons are coupled in Cooper pairs, this increase in the relaxation rate must come from phonons. We postulate the existence of additional tunneling systems with strong phonon coupling. Evidence for

strongly coupled tunneling systems in Nb has been observed previously. In phonon echo experiments below 1 K with Nb:D (sample used in Ref. (1)) phonon echoes were observed at 1.5 GHz. From  $T_1$  echo decay measurements, a phonon coupling of  $\gamma = 0.1$  eV can be inferred using  $v_{\text{Long}} = 4.92 \times 10^5$  cm/s,  $v_{\text{Shear}} = 2.1 \times 10^5$  cm/s,  $\rho = 8.58$  g/cm<sup>3</sup> and  $\coth(\hbar\omega/2k_B T) = 1$  at low temperatures.<sup>17</sup>

To account for the anomalous attenuation, we calculated various attenuation curves taking  $\gamma = 1.85$  eV. The result of one calculation is shown in Figure 5.15. The figure shows the residual attenuation after subtracting  $\alpha_{\text{BCS}}$  (with  $\alpha_n = 0.40$  cm<sup>-1</sup>), and  $\alpha_{\text{TLS}}$  (with  $\gamma = 0.023$  eV). In Figure 5.16  $(\Delta v/v)_{\text{anh}} = 0$  was assumed. In all calculations with  $\gamma \sim 1$  eV the  $E = 0$  relaxation rate was used.

The curves shown in Figures 5.15 and 5.16 were calculated with  $\Delta_0 = 2.0$  K, a Lorentzian distribution of  $\Delta$  with a width of 27 K, and a density of  $9.5 \times 10^{15}$  cm<sup>-3</sup>. Note

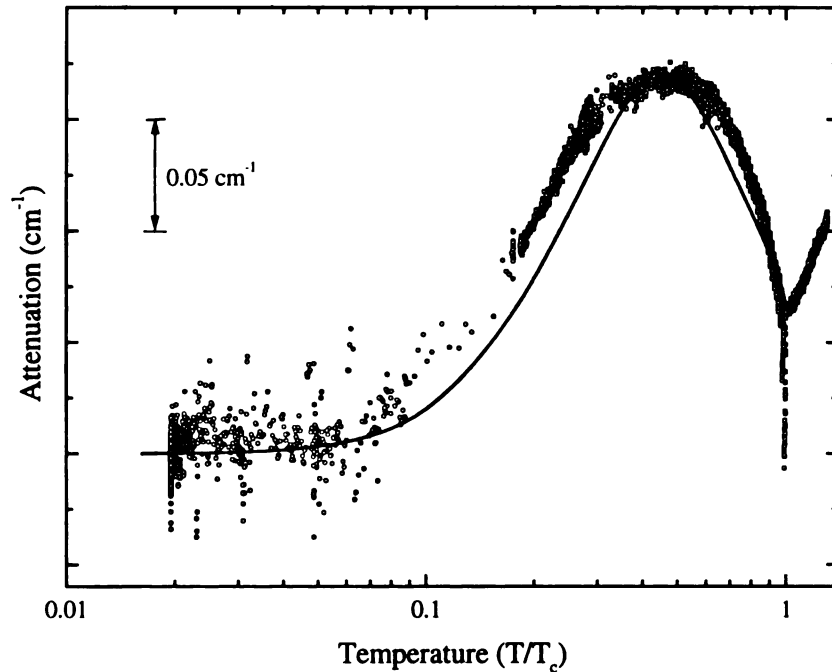


Figure 5.15. The residual attenuation after  $\alpha_{\text{TLS}}$  with  $\gamma = 0.023$  eV and  $\alpha_{\text{BCS}}$  have been subtracted. The solid line is the calculation with  $\gamma = 1.85$  eV.

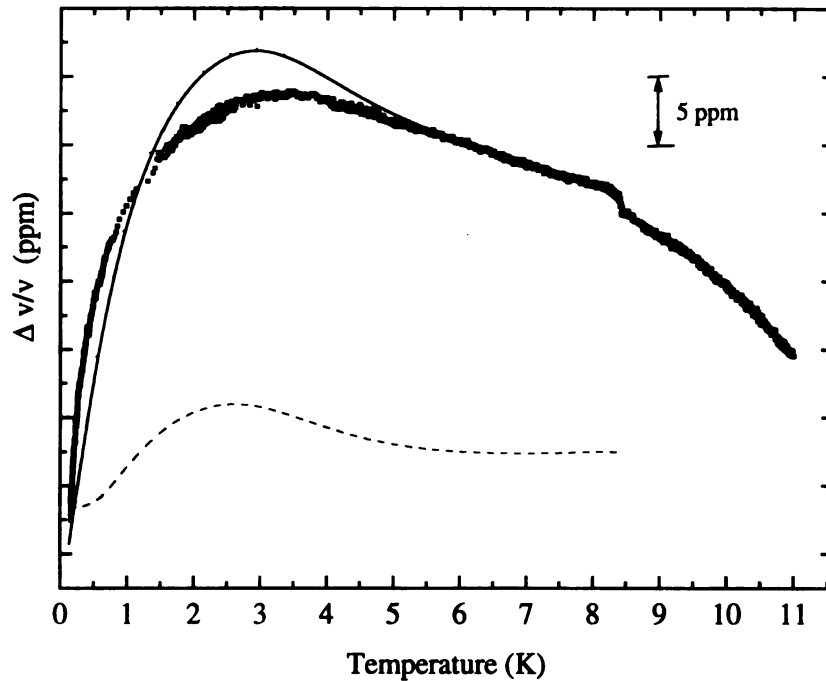


Figure 5.16. The velocity. Dashed line,  $\alpha_{\text{TLS}}$  with  $\gamma = 1.85$  eV; solid line,  $\alpha_{\text{TLS}}$  from the  $\gamma = 0.023$  eV fit plus  $\alpha_{\text{TLS}}$  calculated with  $\gamma = 1.85$  eV.

that the density is 4 orders of magnitude smaller than that found with the small  $\gamma$ . Thus very few states are needed to account for the anomalous attenuation. The strongly coupled states have little effect on the high temperature velocity, as shown in Figure 5.16. The deviations in the low temperature velocity indicate that the strongly and weakly coupled tunneling states must be fit simultaneously rather than consecutively.

Since phonon echoes require resonant absorption there must be states at  $E/k_B = 72$  mK in the Nb:D single crystal. The distribution of the low energy states could be similar to a glass, i.e. with a flat distribution. However, this would result in an incorrect temperature dependence for  $\alpha_{\text{TLS}}$  below 2 K. Another option would be a Lorentzian distribution of  $\Delta_0$  with a small width. Since  $\Delta_0$  is 180 mK in Nb:D,<sup>1</sup> only a relatively narrow distribution width would be necessary to generate states at 70 mK.

## V.5 Summary and Conclusions

We have measured the change in velocity and attenuation in polycrystalline Nb:H films using surface acoustic waves. The data below 11 K were fit with a standard tunneling model which had been successful in describing the acoustic properties of single crystal Nb:H. We found that this model described the polycrystalline film change in velocity and the attenuation above 2 K quite well. However, it was unable to account for the attenuation below 2 K.

We have concluded that the standard model with a weak phonon-tunneling system coupling is insufficient to describe our data. We have postulated the existence of a small fraction,  $10^{-4}$ , of the tunneling systems which may have a strong coupling to phonons  $\sim 1$ eV. These strongly coupled states may occur in regions of high disorder, such as grain boundaries, or may be due to the interactions of larger atoms.

The small tunneling matrix element found in the Nb:H films vis-à-vis single crystals suggests that some states must exist below the cutoff in the density of states below  $\Delta_0$  in the standard model. This is supported by the fact that phonon echoes were previously observed in single crystal Nb:D. Thus, there may be a narrow distribution in  $\Delta_0$  in addition to the Lorentzian distribution of the  $\Delta$ . Adding a narrow distribution of  $\Delta_0$  would increase its peak value and add states at very low energies.

In summary, although the standard model is adequate to describe the bulk of our data, it is necessary to add states with a large coupling to phonons in order to explain the low temperature attenuation. In addition, our small values for the tunneling matrix element indicate that there should be a narrow distribution assigned to the tunneling matrix

element.

## V.6 Future experiments

To further investigate the tunneling of hydrogen in polycrystalline films of Nb more should be done on both the experimental and theoretical fronts. On the experimental front, acoustic measurements should be made on films which have been doped with a higher concentration of H and a known octahedral impurity. In addition, a method for determining the anharmonic contribution to sound propagation in the absence of dopants would be quite useful. On the theoretical front, efficient numerical routines should be developed that will allow one to fit the data with arbitrary distributions in  $\Delta$  and  $\Delta_0$  and that allow for two species of tunneling systems.

- 
- <sup>1</sup> "Isotope dependence of hydrogen tunneling in niobium", W. Morr, A Müller, G. Weiss, H. Wipf, and B. Golding, *Physical Review Letters* 63, 2084-2087 (1989).
- <sup>2</sup> "H and D tunneling in niobium", H. Wipf and K. Neumaier, *Physical Review Letters* 52, 1308-1311 (1984).
- <sup>3</sup> "Low temperature tunneling and quantum diffusion of hydrogen in Nb(NH)<sub>x</sub>", D. Steinbinder, H. Wipf, A.-J. Dianoux, A. Magerl, D. Richter, K. Neumaier, and R. Hemplemann, *Journal of the Less Common Metals* 172-174, 685-692 (1991).
- <sup>4</sup> "Concentration dependence and temperature dependence of hydrogen tunneling in Nb(OH)<sub>x</sub>", A Magerl et al., *Physical Review Letters* 56, 159- 162 (1986).
- <sup>5</sup> "H tunneling and local diffusion in NbO<sub>x</sub>H<sub>y</sub>", H. Wipf, A. Magerl, and K. Neumaier, in *Atomic Transport and Defects in Metals by Neutron Scattering*, edited by C. Janot,

- 
- W. Petry, D. Richter, and T. Springer (Springer-Verlag, New York, 1986) 161-164.
- <sup>6</sup> “Die thermodynamischen Funktionen des Supraleiters”, B. Mühschlegel, *Zeitschrift für Physik* **155**, 313-327 (1959).
- <sup>7</sup> *Introduction to Solid State Physics* by C. Kittel, (John Wiley and Sons, Inc, New York, 1986) 142.
- <sup>8</sup> “SAW measurements on a Nb film and an YBa<sub>2</sub>Cu<sub>3</sub>O<sub>7</sub> film”, H.P. Baum, B.K. Sarm, M. Levy, J. Gavaler, and A. Hohler, *IEEE Transactions on Magnetics* **27**, 1280-1283 (1991).
- <sup>9</sup> “From low to high (T<sub>c</sub>): an ultrasonic investigation of niobium single crystal and YBaCuO superconducting thin films with surface acoustic waves”, H.P. Baum, Ph.D. thesis, University of Wisconsin-Milwaukee (1990).
- <sup>10</sup> “Acoustic absorption due to hydrogen tunneling in NbN<sub>0.0015</sub>H<sub>0.0025</sub>”, J.L. Wang, G. Weiss, H. Wipf, and A. Magerl, in *Phonon Scattering in Condensed Matter*, edited by W. Eisenmenger, K. Laßmann, and S. Döttinger (Springer Verlag, New York, 1984) pp. 401-403.
- <sup>11</sup> “Ultrasonic detection of an energy gap change in the N/S transition for trapped H in Nb”, K.R. Maschhoff, E. Drescher-Krasicka, and A.V. Granato, in *Phonon Scattering in Condensed Matter V*, edited by A.C. Anderson and J.P. Wolfe (Springer-Verlag, New York, 1986) pp. 64-66.
- <sup>12</sup> “H and D tunneling in Nb: dependence on defect concentration and trapping center”, P. Gutsmeidl, M. Schiekhofer, K. Neumaier, and H. Wipf, in *Quantum Aspects of Molecular Motions in Solids*, edited by A. Heidemann, A. Magerl, M. Prager, D.

- 
- Richter and T. Springer, (Springer Verlag, New York, 1987) pp. 158-162.
- <sup>13</sup> “Low temperature tunneling and quantum diffusion of hydrogen in Nb(NH)<sub>x</sub>”, D. Steinbinder, H. Wipf, A.-J. Dianoux, A. Magerl, D. Richter, K. Neumaier, and R. Hemplemann, *Journal of the Less-Common Metals* 172-174, 685-692 (1991);
- “Quantum diffusion of trapped-hydrogen interstitials in Nb: the role of tunnel splitting”, D. Steinbinder, H. Wipf, A.-J. Dianoux, A. Magerl, K. Neumaier, D. Richter, and R. Hemplemann., *Europhysics Letters* 16, 211-216 (1991).
- <sup>14</sup> “Low temperature hydrogen tunneling in NbO<sub>x</sub>H<sub>y</sub> (x ≈ 0.002; y ≈ 0.002)”, H. Wipf, K. Neumaier, A. Magerl, A. Heidemann and W. Stirling, *Journal of the Less-Common Metals* 101, 317-326 (1984).
- <sup>15</sup> “H and D tunneling in niobium”, H. Wipf and K. Neumaier, *Physical Review Letters* 52, 1308-1311 (1984).
- <sup>16</sup> “Nonadiabatic low temperature quantum diffusion of hydrogen in Nb(OH)<sub>x</sub>”, D. Steinbinder, H. Wipf, A. Magerl, D. Richter, A.-J. Dianoux and K. Neumaier, *Europhysics Letters* 6, 535-540, (1988).
- <sup>17</sup> B. Golding (private communication).

## Appendix A

### Circuitry

In this appendix the details of the electronic circuits and the methods used in measuring the attenuation and change in velocity in the acoustic channel will be presented.

#### A.1 The circuit used above 1.2 K.

In the following discussion, the electronics circuit used above 1.2 K is divided into three parts. First, the circuitry used to define the pulses before they are input into the generating transducer will be discussed. The circuitry used to detect the attenuation of the SAW will then be addressed. Finally, the phase lock circuit used to measure the change in velocity of the acoustic wave will be shown.

##### A.1.i Pulse forming circuit

The pulse forming circuit is shown in Figure A.1. The sweep oscillator, a, generates continuous wave signals with frequencies between 0.01 and 2.4 GHz. This CW signal is converted into pulses by switches. Two switches were used in order to reduce the amount of signal which might leak through a single closed switch. One switch, f, was open for  $\sim 100$  nsec. The second, g, was open for  $\sim 1$   $\mu$ sec. The width of both pulses was set by the custom pulse stretcher, h.

The stretcher was triggered by a pulse generator, i. The repetition rate of the pulse generator was set to 1 kHz. The delays of the pulse generator outputs were set so that  $B = T_0 + 0.3$   $\mu$ sec and  $D = B + 0.2$   $\mu$ sec.  $T_0$  triggered the broad pulse and B opened the

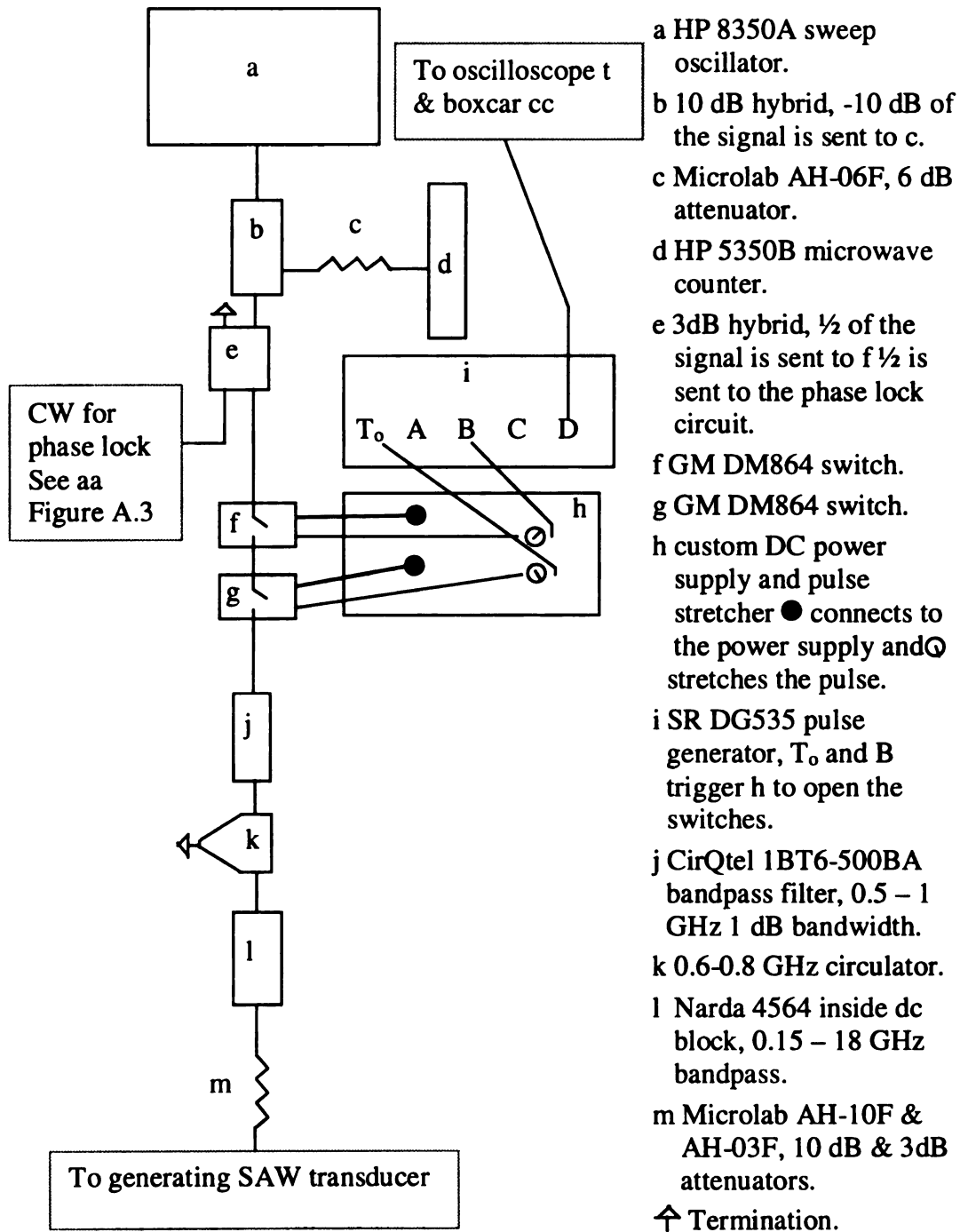


Figure A.1. The pulse forming circuit

narrow pulse. D triggered both the oscilloscope (see Figure A.2) and the boxcar (see Figure A.3).

After the pulse was formed it was sent through various filters in order to remove noise due to the switches and/or frequency generator. The CirQtel filter, j, removed much of the switching noise. The circulator, l, acted as a diode, only allowing signals to travel in the forward direction from the sweep oscillator to the SAW device. Thus any signals reflected after the circulator were eliminated.

The sweep oscillator was set at power of 15.0 dBm in order to drive the mixer, aa from Figure A.3. Therefore to reduce the signal into the generating transducer the signal was attenuated at m.

The measurements done with an applied magnetic field were done after the circuit had been altered to allow for measuring the attenuation by the homodyne method (see A.2). When the diode detector circuit was put back together to measure the attenuation in a magnetic field, it was slightly different. The sweep oscillator's power was increased to 16.0 dBm. In order to protect the microwave counter, an AH-03F 3dB attenuator was added to the 6 dB, c, already in place. In addition, the 13 dB, m, was removed and HP 8494H & HP 8496H variable attenuators powered by an HP 117134A attenuator/switch driver were put between j and k. These changes were insignificant to how the circuit operated, but did affect the calibration which will be discussed below.

### A.1.ii Detection circuit

The signals from the two receiving transducers were individually amplified by preamplifiers o and p. After amplification, the rf signals were converted into dc signals by diode detectors r. These dc signals were then amplified by a pulse amplifier, s, and sent to the scope. The amplitude of the pulse was measured within a 10 nsec window. The scope continually measured and averaged the statistical base within the measurement window for 3 seconds. This corresponded to averaging about 200 measurements. The averaged value was then sent to a computer. In order to compensate for any drift in the signal, after every fifth measurement of the pulse height, a 3 second average was taken of the baseline and the average value sent to the computer. Later this base value was subtracted from the amplitude in order to obtain the absolute pulse height.

When the resonance curves of the transducers were measured at a set temperature, the frequency of a was manually set. The frequency was changed by set increments and the corresponding amplitude of the signal measured by the oscilloscope and sent to the computer. Before heating and cooling runs, the frequency was manually set at the peak of the resonance curve. As the temperature changed, the frequency was varied by the phase lock circuit as discussed in A.1.iii and Appendix B.

The detection circuit was calibrated by replacing the part of the circuit in the Kelvinox with the variable attenuator and then measuring the pulse height as discussed above over a range of 25 dB. The variable attenuator settings could be varied in increments of 1 dB. The variable attenuator had a stated repeatability of  $\pm 0.01$  dB and an accuracy of  $\pm 1$  dB. The 25 amplitudes measured described a smooth curve. This curve was then used to convert all subsequent measurements of the pulse amplitude to attenuation.

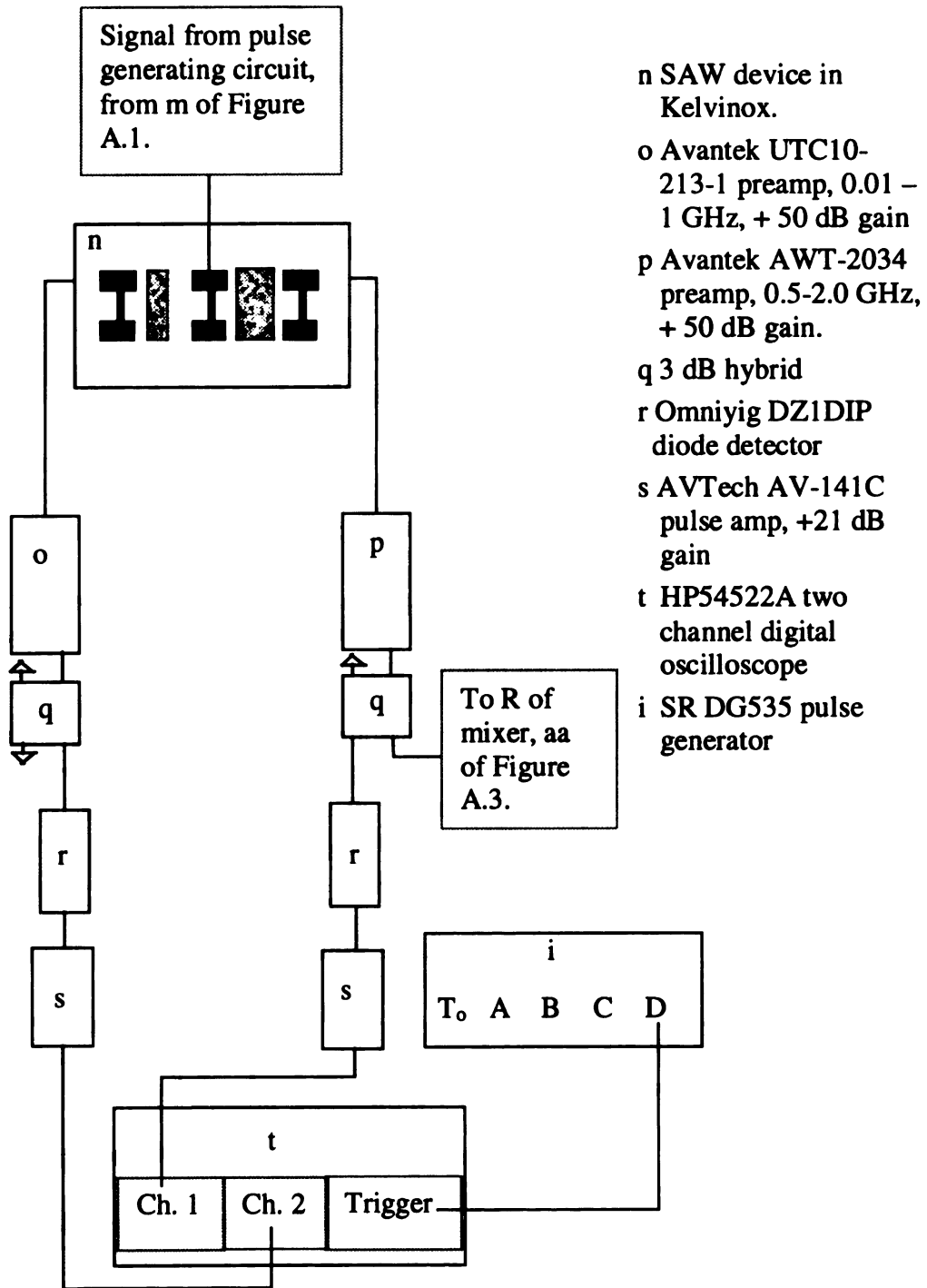


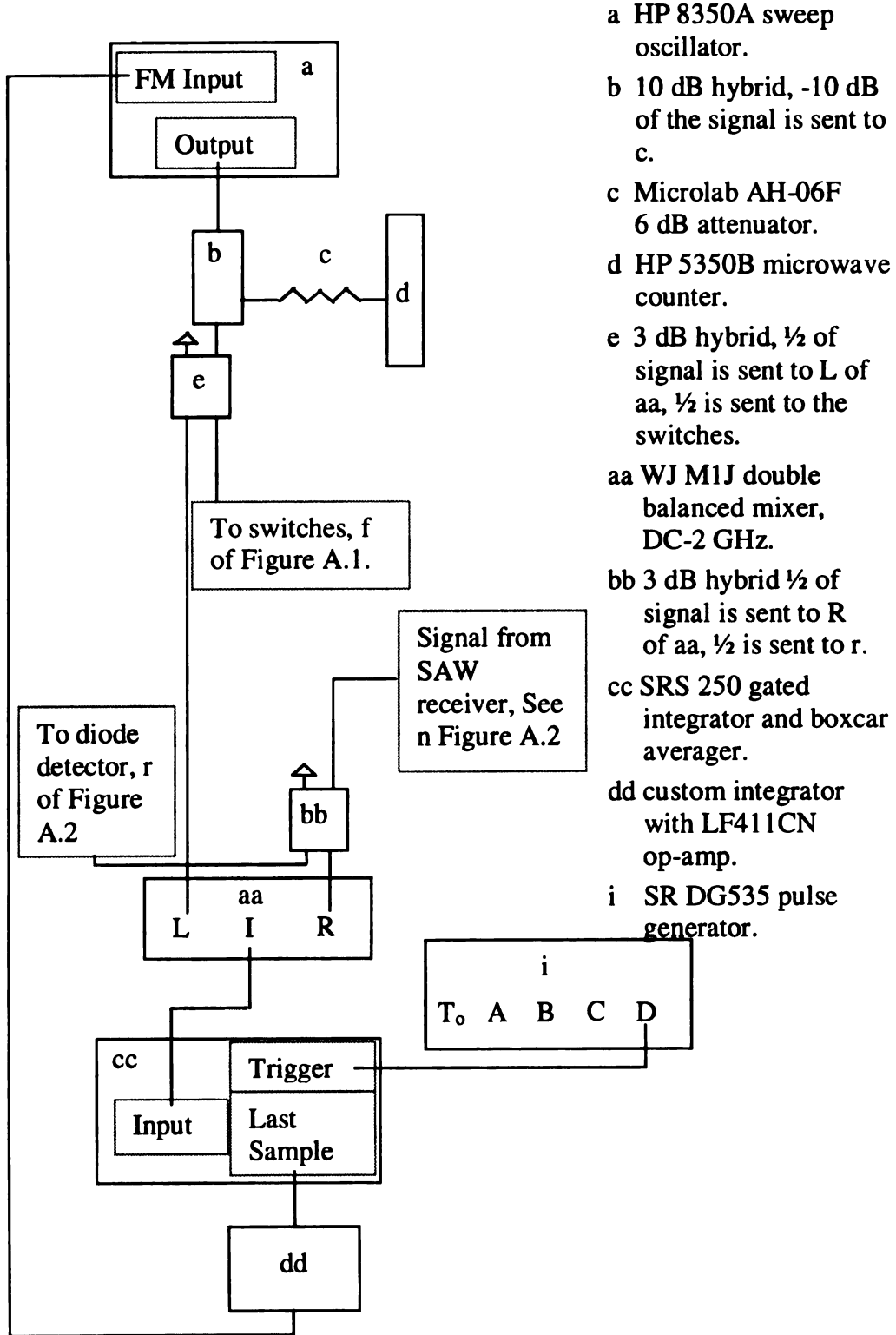
Figure A.2 The attenuation measurement circuit

The measurements taken with a magnetic field were calibrated by varying the setting of the variable attenuator and measuring the corresponding SAW signal height. A smooth curve was then drawn through the points and this curve used to convert amplitudes to attenuation.

### A.1.iii Phase Lock Circuit

The change in velocity in the acoustic channel was measured using a differential method called phase locking. A CW signal was sent to the local oscillator port of the mixer, L of aa, and mixed with a signal which had traveled through the LiNbO<sub>3</sub> with an overlayer of Nb. The two signals had the same frequency, but different phases due to the fact that they had traveled along different paths. The mixer's output from port I was a dc signal with an amplitude which was proportional to the phase difference between the two inputs. If the phase difference was equal to 90° or 270° the output of the mixer was a null signal. If the two signals were in phase a maximum was output and if they were 180° out of phase a minimum was output. In order to measure the change in velocity with temperature, the frequency change required to maintain a constant phase difference was measured by the microwave counter, d. The mathematical relationship between the change in frequency and the change in velocity is derived in Appendix B.

Thus, to measure the change in velocity, the frequency was varied so that a constant phase was maintained. In other words the circuit was phase locked. Phase locking was accomplished by sending the output of the mixer to a boxcar, cc, with a 10-20 nsec gate. The boxcar output a constant dc signal to the integrator, dd, which was proportional to the amplitude of the signal from the mixer. The integrator controlled the frequency



- a HP 8350A sweep oscillator.
- b 10 dB hybrid, -10 dB of the signal is sent to c.
- c Microlab AH-06F 6 dB attenuator.
- d HP 5350B microwave counter.
- e 3 dB hybrid, 1/2 of signal is sent to L of aa, 1/2 is sent to the switches.
- aa WJ M1J double balanced mixer, DC-2 GHz.
- bb 3 dB hybrid 1/2 of signal is sent to R of aa, 1/2 is sent to r.
- cc SRS 250 gated integrator and boxcar averager.
- dd custom integrator with LF411CN op-amp.
- i SR DG535 pulse generator.

Figure A.3. Phase locking circuit

output of the sweep oscillator, a, and varied this frequency until its input (the output from the mixer) was a null signal and thus a constant phase difference was maintained.

## A.2 The circuit used below 1.2 K.

Below 1.2 K the attenuation in the Nb was measured by homodyning. The velocity measurement was identical to that used above 1.2 K. As mentioned above, the output of a mixer is maximized when the two inputs are in phase. This is a very sensitive method for measuring small changes in attenuation. As shown in Figure A.4, both the CW signal and the output from a receiving transducer were split by a 3 dB hybrid and sent to the two inputs of two mixers. A phase adjuster was placed in the path for the local oscillator of aa-A. It was used to adjust the phase so that the signal from aa-A was maximized when the output of aa-F was zero. The output of aa-A was then sent to a pulse amplifier and into the oscilloscope. The amplitude of the signal was measured using same method as above 1.2 K. A calibration curve for converting amplitude to attenuation was created by varying the variable attenuator and measuring the corresponding signal amplitude. A smooth curve was then drawn through these points to create the calibration curve.

The phase and average velocity change with temperature in the two acoustic channels were different (due to the difference in the Nb lengths). Therefore the amplitude of only one channel could be measured using the homodyne method.

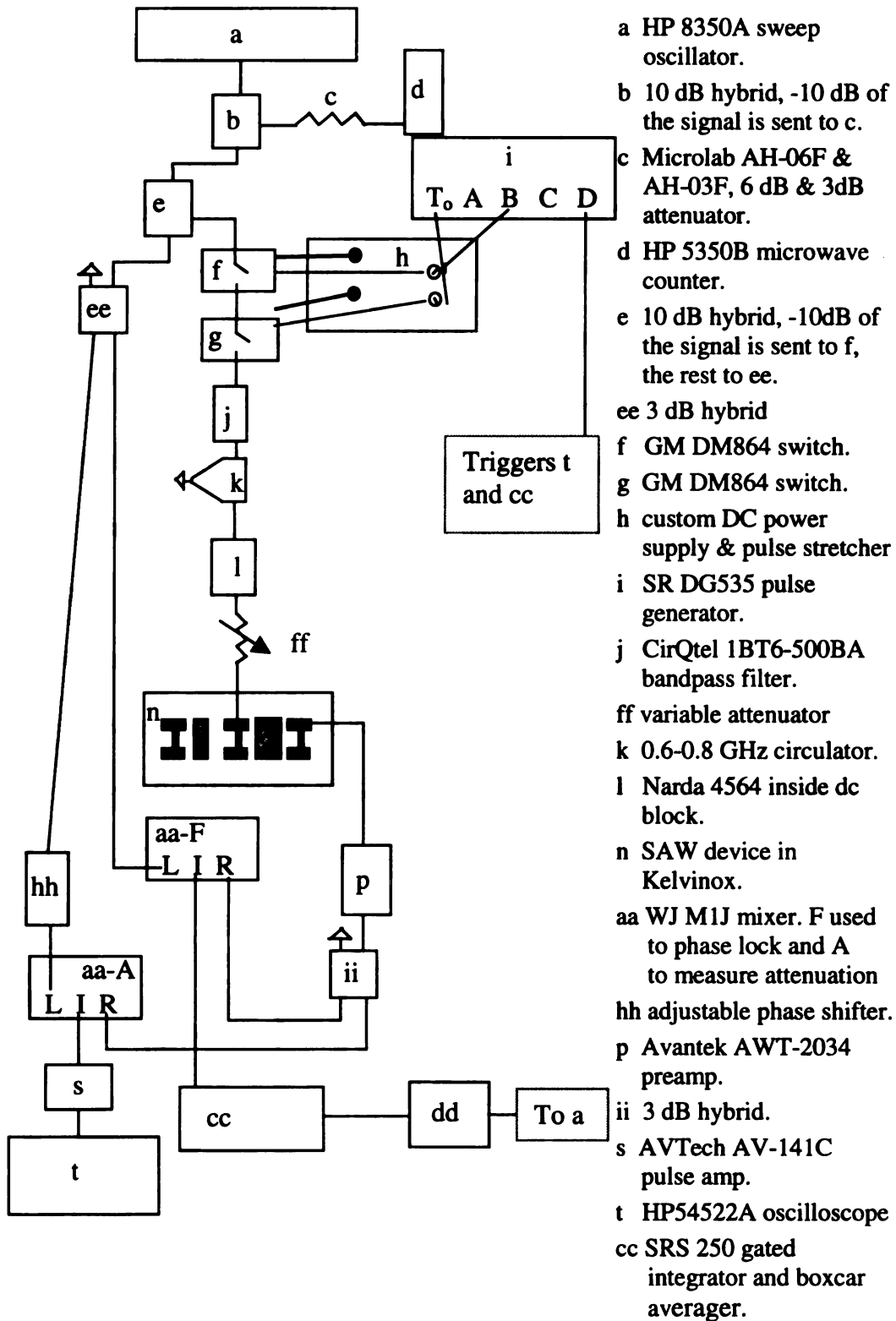


Figure A.4. The homodyning circuit used below 1.2 K

## Appendix B

### Velocity measurements

#### B.1 Measuring the velocity at constant temperature

In order to measure the absolute velocity at fixed temperature a signal was split into two paths. One path was purely electromagnetic and the other has an acoustic length in addition to an electromagnetic length. It is the velocity in this acoustic path which we wished to measure. After passing through the two paths, the signals were recombined in a microwave mixer. The output of a microwave mixer is proportional to the phase difference between the two inputs. If the phase difference between the two paths is  $90^\circ$  or  $270^\circ$  the mixer output is zero. Assuming that all relevant lengths are known, the acoustic velocity can be measured by measuring the change in frequency between successive zeros of the mixed signal. Below is a derivation of the relationship between the velocity and the zeros of the mixed signal.

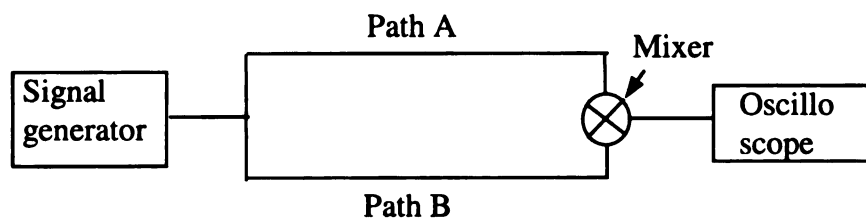


Figure B.1. A signal is split and travels through two different paths. The signal is then recombined in a mixer and the combined signal observed on an oscilloscope

Phase =  $\varphi = \frac{\omega L}{v}$  where  $\omega$  = angular frequency,  $L$  = pathlength, and  $v$  = velocity

$\varphi_A = \varphi_B \pm (2n + 1/2)\pi$   $n$  is an integer, implying the phase difference between the two paths is  $90^\circ$ .  $n$  &  $n + 1$  will have the same phase difference

$$\Rightarrow \left\{ \begin{array}{l} \omega_1 \frac{L_A}{v_A} = \omega_1 \frac{L_B}{v_B} + (2n + 1/2)\pi \\ \omega_2 \frac{L_A}{v_A} = \omega_2 \frac{L_B}{v_B} + (2(n+1) + 1/2)\pi \end{array} \right\} \quad \begin{array}{l} \omega_1 \text{ and } \omega_2 \text{ are successive zeros} \\ \text{of the mixed signal} \end{array}$$

subtracting the two above equations,

$$\Rightarrow (\omega_1 - \omega_2) \frac{L_A}{v_A} = (\omega_1 - \omega_2) \frac{L_B}{v_B} + 2\pi$$

$$\Rightarrow \Delta f^{-1} = \frac{L_A}{v_A} - \frac{L_B}{v_B} \quad \text{where } \Delta f \text{ is the change in frequency between successive zeros of the mixed signal.}$$

In our experiments Path A is a pure CW electromagnetic signal and Path B contains a pulsed signal with both acoustic and electromagnetic lengths, implying that  $\frac{L_A}{v_A} = \frac{L_{em}^{CW}}{v_{em}}$

and  $\frac{L_B}{v_B} = \frac{L_{em}^{pulsed}}{v_{em}} + \frac{L_{acoustic}^{pulsed}}{v_{acoustic}}$ . Although the delay due to the electromagnetic part of the

path is quite small, it is important to include it in order to calculate accurate acoustic delays. The acoustic delay,  $\tau^{ac} = L_{acoustic} / v_{acoustic}$ , is further broken up into a sum of delays if one has two different velocities, i.e. a LiNbO<sub>3</sub> and a LiNbO<sub>3</sub> plus an overlayer of Nb velocity.

The delay for each acoustic channel was found individually and then the two delays were combined to deduce the velocity of the LiNbO<sub>3</sub> alone and with a thin film of Nb. In

Run 4.16 when both acoustic paths were partially covered with Nb, the LiNbO<sub>3</sub> velocity,  $v_L$ , and the LiNbO<sub>3</sub> plus Nb velocity,  $v_N$  were calculated using the equations,

$$v_L = \frac{L_{LC} - L_{LA} \left( \frac{L_{NC}}{L_{NA}} \right)}{\tau_C^{ac} - \tau_A^{ac} \left( \frac{L_{NC}}{L_{NA}} \right)}$$

$$v_N = \frac{L_{NA}}{\tau_A^{ac} - \frac{L_{LA}}{v_L}}$$

where the two acoustic channels are denoted by subscripts A and C (corresponding to the name of the receiver).  $\tau_i^{ac}$ ,  $L_{Li}$ , and  $L_{Ni}$  are the delay, the length of the free LiNbO<sub>3</sub>, and the length of the LiNbO<sub>3</sub> with a Nb film in the  $i^{\text{th}}$  acoustic channel respectively.

## B.2 Derivation of frequency to velocity conversion factor.

The change in velocity in an acoustic channel as a function of temperature was also measured. This was accomplished by varying the frequency of the signals into the mixer so that a constant phase difference was maintained. The circuit used is described in Appendix A. The derivation of the conversion factor for converting the change in frequency to a change in velocity is discussed in the following paragraphs. First a general derivation of the  $\frac{\Delta f}{f} \rightarrow \frac{\Delta v}{v}$  factor will be shown. Then specific adaptations for

Run 4.15 and Run 4.16 will be discussed.

## B.2.i General derivation.

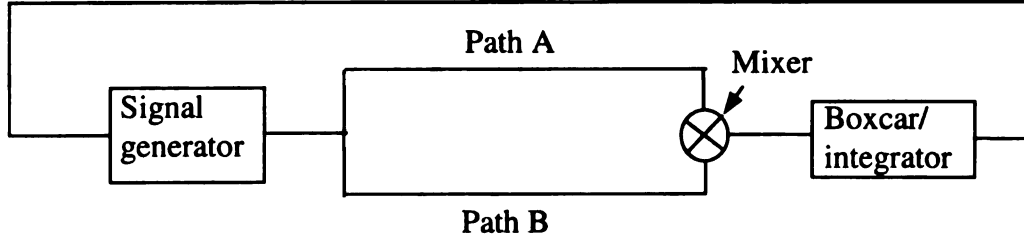


Figure B.2. A signal is split and travels through two different paths. The velocity is constant in path A and varies in path B. The signal is then recombined in a mixer and sent to the boxcar/integrator which varies the frequency of the signal generator so that constant phase at the mixer is maintained.

As shown in Figure B.2, a signal is split into two paths, in Path A the velocity is constant while in Path B the velocity changes. The frequency of the signal generator is changed so that the phase at the mixer remains constant. The phases before and after the velocity in Path B changes are shown in Table B.1.

Table B.1, the phase,  $\phi$ , of the two paths before and after the velocity changes in Path B

	Path A	Path B	$\phi_A - \phi_B$
$\phi$	$k_A L_A + \omega \frac{L_A}{v_A}$	$k_B L_B + \omega \frac{L_B}{v_B}$	$k_A L_A - k_B L_B + \omega \left( \frac{L_A}{v_A} - \frac{L_B}{v_B} \right)$
$\phi'$	$k'_A L_A + \omega' \frac{L_A}{v_A}$	$k'_B L_B + \omega' \frac{L_B}{v'_B}$	$k'_A L_A - k'_B L_B + \omega' \left( \frac{L_A}{v_A} - \frac{L_B}{v'_B} \right)$

where  $k$ ,  $L$ , and  $v$  are the wavevector, length and velocity of a path and  $\omega$  is the frequency.

The change in the phase difference between the two paths is given by,

$$\Delta(\phi_A - \phi_B) = (k_A - k'_A) L_A - (k_B - k'_B) L_B + (\omega - \omega') \frac{L_A}{v_A} - \omega \frac{L_B}{v_B} + \omega' \frac{L_B}{v'_B}$$

$k = \frac{\omega}{v}$  and the boxcar/integrator varies the frequency such that  $\Delta(\varphi_A - \varphi_B) = 0$

$$\Rightarrow 0 = (\omega - \omega') \frac{L_A}{v_A} - \omega \frac{L_B}{v_B} + \omega' \frac{L_B}{v_B} \quad *$$

Let  $v'_B = v_B + \varepsilon$ , then  $\frac{1}{v_B + \varepsilon} = \frac{1}{v_B} - \frac{\varepsilon}{v_B^2}$  assuming that  $\varepsilon \ll v_B$

$$\Rightarrow 0 = (\omega - \omega') \left( \frac{L_A}{v_A} - \frac{L_B}{v_B} \right) - \frac{\omega' \varepsilon}{v_B^2} L_B$$

$$\Rightarrow \frac{\Delta v_B}{v_B} = \frac{\Delta \omega}{\omega} \left( 1 - \frac{L_A v_B}{v_A L_B} \right)$$

since  $\omega \approx \omega' \gg \Delta \omega$

### B.2.ii Specific derivation for Run 4.16.

In Run 4.16, Path A is purely electromagnetic while Path B has an electromagnetic path plus a constant velocity acoustic path, LiNbO<sub>3</sub>, plus a varying velocity acoustic path, LiNbO<sub>3</sub> covered with a thin film of Nb. Thus

$$\frac{L_A}{v_A} = \frac{L_A}{v_{EM}}$$

$$\frac{L_B}{v_B} = \frac{L_B^{EM}}{v_{EM}} + \frac{L_L}{v_L} + \frac{L_N}{v_N}$$

where the subscripts L and N denote the LiNbO<sub>3</sub> and LiNbO<sub>3</sub> + Nb paths respectively and the sub/superscript EM denotes the electromagnetic path's length or velocity. In

order to derive the  $\frac{\Delta f}{f} \rightarrow \frac{\Delta v}{v}$  relationship, one must go to the starred equation in the

general derivation and substitute the above lengths in.

$$\begin{aligned} \Rightarrow 0 &= (\omega - \omega') \frac{L_A}{v_{EM}} - \omega \left( \frac{L_B^{EM}}{v_{EM}} + \frac{L_L}{v_L} + \frac{L_N}{v_N} \right) + \omega' \left( \frac{L_B^{EM}}{v_{EM}} + \frac{L_L}{v_L} + \frac{L_N}{v'_N} \right) \\ &= (\omega - \omega') \left( \frac{L_A}{v_{EM}} - \frac{L_B^{EM}}{v_{EM}} - \frac{L_L}{v_L} \right) - \omega \frac{L_N}{v_N} + \omega' \frac{L_N}{v'_N} \end{aligned}$$

Let  $v'_N = v_N + \varepsilon$ , then  $\frac{1}{v_N + \varepsilon} = \frac{1}{v_N} - \frac{\varepsilon}{v_N^2}$

$$\begin{aligned} \Rightarrow 0 &= (\omega - \omega') \left( \frac{L_A - L_B^{EM}}{v_{EM}} - \frac{L_L}{v_L} \right) - \omega \frac{L_N}{v_N} + \omega' \frac{L_N}{v_N} - \omega' \frac{L_N \varepsilon}{v_N^2} \\ \Rightarrow \frac{(\omega' - \omega)}{\omega'} \left( \frac{v_N}{L_N} \right) \left( \frac{L_B^{EM} - L_A}{v_{EM}} + \frac{L_L}{v_L} + \frac{L_N}{v_N} \right) &= \frac{v'_N - v_N}{v_N} \\ \Rightarrow \frac{\Delta v}{v} = \frac{\Delta \omega}{\omega} \left( \frac{v_N}{L_N v_{EM}} (L_B^{EM} - L_A) + \frac{v_N L_L}{L_N v_L} + 1 \right) \end{aligned}$$

Using the values (taken from Table 3.2 and Table 4.1)  $v_N = 3242 \pm 90$  m/s,  $v_L = 3960 \pm 80$  m/s,  $L_N = 3.018 \pm 0.031$  mm,  $L_L = 3.059 \pm 0.069$  mm,  $L_B^{EM} = 13.3 \pm 0.3$  m,  $L_A = 7.9 \pm 0.3$  m, and  $v_{EM} = 2.07 \cdot 10^8$  m/s one finds that  $\frac{v_N}{L_N v_{EM}} (L_B^{EM} - L_A) = 0.028 \pm 0.002$

and  $\frac{v_N L_L}{L_N v_L} = 0.830 \pm 0.035$ . Thus  $\frac{\Delta v}{v} = (1.86 \pm 0.04) \frac{\Delta f}{f}$ .

*Checking the limits of the equation.*

As  $L_L \rightarrow 0$ , i.e. the acoustic path is completely filled with Nb,

$$\frac{\Delta v}{v} \rightarrow \frac{\Delta f}{f} \left( \frac{v_N}{L_N v_{EM}} (L_B^{EM} - L_A) + 1 \right).$$

If the electromagnetic lengths were equal and thus

their phase not affected by a changing frequency, then  $\frac{\Delta v}{v} \rightarrow \frac{\Delta f}{f}$  which is as expected.

If  $L_N$  becomes quite small, but not zero, the multiplicative factor for  $\frac{\Delta f}{f}$  becomes quite large. This is correct. As the portion of Nb in the channel shrinks, so will the change in the average velocity,  $\frac{\Delta v}{v}$  avg. The average velocity equals  $\frac{\Delta f}{f}$  when the electromagnetic lengths are equal and thus as  $\frac{\Delta v}{v}$  avg shrinks so must  $\frac{\Delta f}{f}$ . But, the change in the velocity of the niobium remains the same, thus  $\frac{\Delta f}{f}$  must be multiplied by a larger number to recover the change in velocity in the small piece of Nb.

### B.2.iii The conversion for Run 4.15.

In Run 4.15 the two acoustic channels were mixed to measure the change in velocity with temperature. Path B was the same as Run 4.16, but Path A included an acoustic length of uncovered  $\text{LiNbO}_3$ . Thus,

$$\begin{aligned} \frac{L_A}{v_{EM}} &\rightarrow \frac{L_A^{EM}}{v_{EM}} + \frac{L_A^{ac}}{v_L} \\ \Rightarrow \frac{\Delta v}{v} &= \frac{\Delta f}{f} \left( \frac{v_N}{L_N v_{EM}} (L_B^{EM} - L_A) + \frac{v_N}{L_N} \left( \frac{L_L}{v_L} - \frac{L_A^{ac}}{v_L} \right) + 1 \right) \\ &= ((-0.005 \pm 0.003) - (0.819 \pm 0.04) + 1) \frac{\Delta f}{f} \\ &= (0.176 \pm 0.04) \frac{\Delta f}{f}. \end{aligned}$$

This was found using the velocities from Run 4.16 and

$L_B^{EM} = 14.5 \pm 0.3$  m,  $L_A^{EM} = 15.4 \pm 0.5$  m,  $L_N = 3.024 \pm 0.01$  mm,  $L_L = 3.056 \pm 0.01$  mm, and  $L_A^{ac} = 6.08 \pm 0.01$  mm.

## Appendix C

### Thermometer Calibrations

#### C.1 Run 4.15.

In this run the calibration RuO<sub>2</sub> was used. It was a polynomial fit to the superconducting standard points measured 2/95 by M. Jaeger plus a spline fit to points measured versus the Pt thermometer at 10, 15, and 20 K. The high T points were not calibrated well – the Pt and RuO calibrations did not agree during the warm up at the end of the run. This polynomial fit had strange curvature below 0.2K. The calibration curve is shown in Figure C.1.

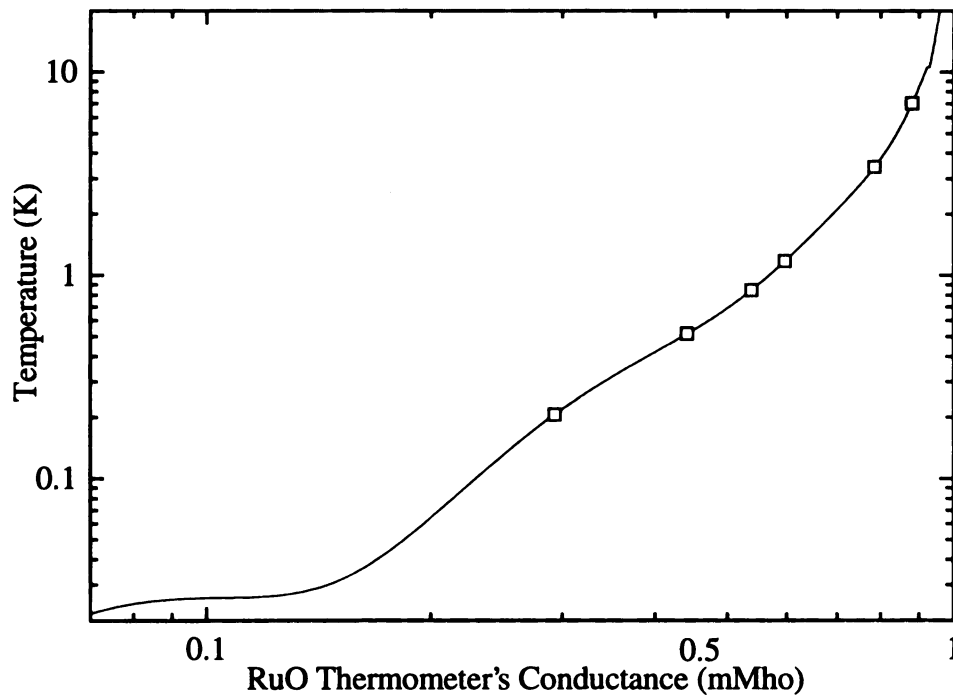


Figure C.1. The RuO thermometer calibration used in Run 4.15. , su perconducting standard points measured 2/95.

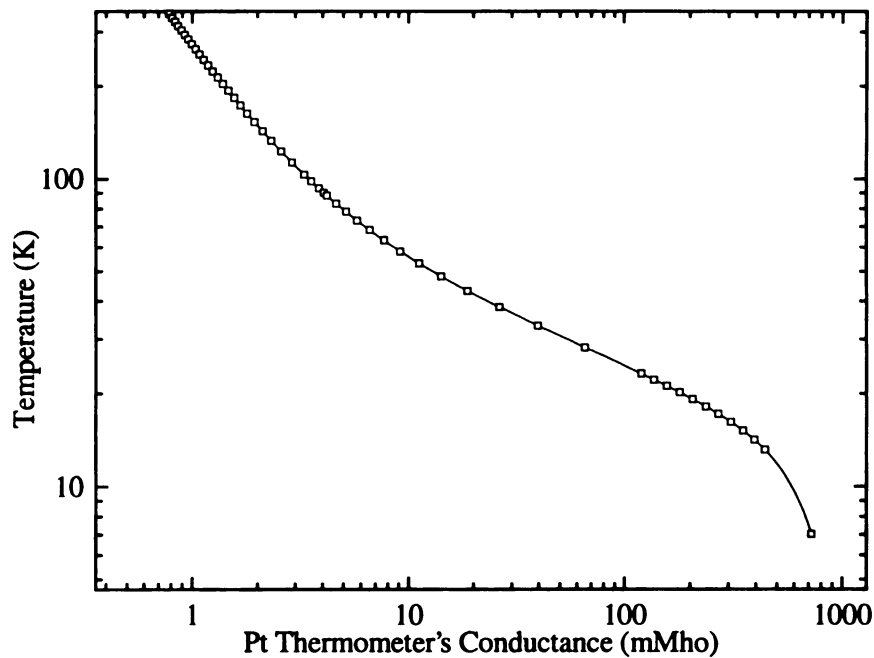


Figure C.2. The Pt thermometer calibration curve. The line is the prtmdj, a spline fit to the data points of Pt95.dat.

The superconducting standard was briefly measured around the Pb transition temperature. The Pb superconducting transition was around 6.87 K (according to RuO2 calibration) instead of 7.021 K as it should be, indicating that the RuO2 calibration polynomial was converting temperatures a little low.

Above 15 K the Pt calibration prtmdj was used. This calibration is a spline fit to Pt95.dat done by Mike Jaeger and is shown in Figure C.2.

## C.2 Run 4.16

I created my own polynomial fit of the transitions seen in the superconducting standard during this run. This conversion is in an Origin script file Ruo925.txt. The bridge readings at the superconducting transitions, if converted with RuO2, were all low compared to their true values. The Ruo925 fit is untrustworthy below 0.2 K as there were

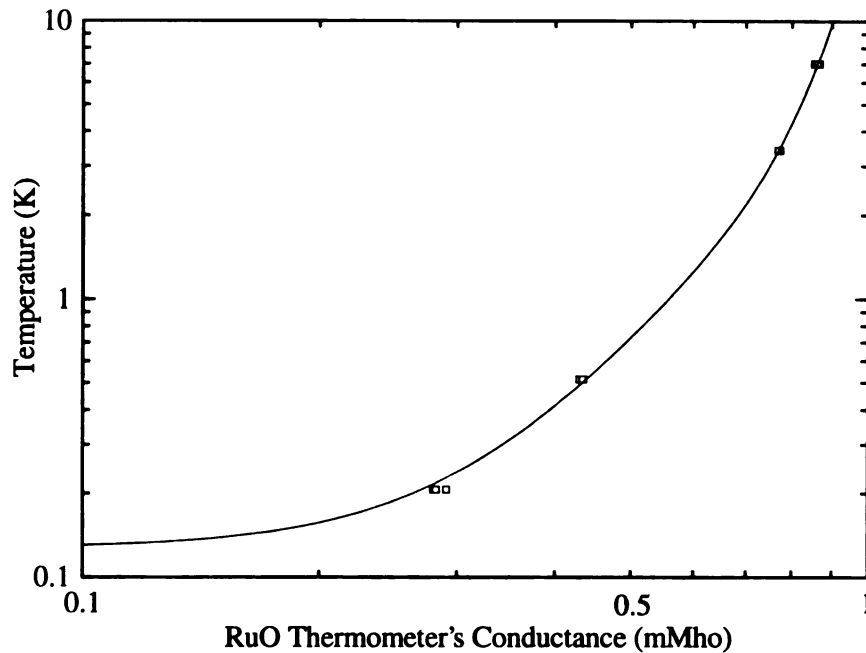


Figure C.3. RuO calibration during Run 4.16. The points are the conductance read when the superconducting standard underwent transitions as the Kelvinox was heated or cooled.

no points below this to fit to (as was the case with RuO<sub>2</sub>) and it was possible to fit all the points and have quite different curvatures below 0.2 K. The calibration curve is shown in Figure C.3.

Above 15 K prtmj, the same Pt thermometer calibration as used in Run 4.15, was used. By the end of Run 4.16 the conductance bridge for reading the thermometers was becoming increasingly unstable.

## Appendix D

## Previous Research on Nb:H

Author/year	compound	Single crystal?	method	Temperature	Width	$\Delta_0$	K, $\gamma$	Comments
Wipf '81 <sup>1</sup>	NbO <sub>0.13</sub> H <sub>0.016</sub>	Polycrystal-line rods	Neutron scattering	At 0.09 K & 5 K	$\geq 11.6$ K	<b>2.2K</b>	?	
Bellessa '83 <sup>2</sup>	NbO <sub>0.0007</sub> H <sub>0.017</sub>	Monocrystal line rods	Velocity at 200 MHz	.05 K to 10K	No distribution	<b>1.5 K</b>		No relaxational interaction
Wipf '84 <sup>3</sup>	<sup>91</sup> Nb(OH) <sub>0.002</sub>	4 single crystal rods	Neutron Scattering	0.15 K	$52 \pm 17$ K	<b>2.2<math>\pm</math>0.2 K</b>	?	Both neutron scattering &
		1 single crystal rod	Specific heat	0.2 – 2.0 K	$41 \pm 17$ K	<b>2.4<math>\pm</math>0.3 K</b>	?	specific heat were on the same samples.
Wipf '84 <sup>4</sup>	NbO <sub>0.001</sub> H <sub>0.0008</sub>	Polycrystal-line rods	Specific heat	0.04 – 2 K	18.6 K	<b>2.2K</b>	?	
	NbO <sub>0.003</sub> H <sub>0.0024</sub>				53 K	<b>2.2K</b>		
Dresher-Krasicka '85 <sub>5</sub>	Nominal NbO <sub>0.0001</sub> H <sub>0.0007</sub> Analysis = 70ppm C, 49ppm N, & 64ppm O	?	Attenuation and velocity at 10 & 30 MHz	T < 20K	Avg $\Delta$ = 0.85K	<b>1.7 K</b>	?	Random distribution of strain

Author/year	compound	Single crystal?	method	Temperature	Width	$\Delta_0$	K, $\gamma$	Comments
Cannelli '86 <sub>6</sub>	Nb-O(N)-H <sub>0.002</sub>	Polycrystalline disk	Internal friction at 20 & 73 kHz			10.4K	?	Tunneling matrix is a function of strain. Probably a different tunneling system. No isotope dependence
Magerl '86 <sup>7</sup>	Nb(OH) <sub>0.011</sub>	?	Neutron scattering	0.5 K – 10 K	> $\Delta_0$	3.1 K	?	$\Delta_0$ distribution isn't Lorentzian W=1.16 K
	Nb(OH) <sub>0.0022</sub> <sup>a</sup>	Two single crystals			> $\Delta_0$	2.7 K	?	Lorentzian $\Delta_0$ with W=0.17 K
	Nb(OH) <sub>0.00015</sub>	?			0.7 K	2.0 K	?	Lorentzian $\Delta_0$ with W=0.06K
Wipf '87 <sup>8</sup>	Nb(OH) <sub>0.002</sub> and Nb(OH) <sub>0.0002</sub>	?	Neutron scattering	0.1 to 10 K		SC=2.6 K N <sub>b</sub> =2.4K	Found K=0.053 ± 0.008	No W given but used Lorentzian $\Delta_0$ and $\Delta$
Wipf '87 <sup>9</sup>	NbO <sub>0.0002</sub> H <sub>0.0002</sub>	2 Single Crystals	Neutron Spectroscopy	At 0.2 & 4.3 K		SC=2.6 K N <sub>b</sub> =2.4K	K=0.05-0.06	$\Delta_0$ normal varies with T by about 10%
Gutsmiedl '87 <sup>10</sup>	NbO <sub>x</sub> H <sub>y</sub> series (0.00005 < x,y < 0.02)	Polycrystalline rods	Specific Heat	0.3 to 4 K	Increases w/ concentration	2.74 K		Width of $\Delta_0$ = 0.14K – low, $\Delta_0$ = 0.41 K – high concentration

Author/year	compound	Single crystal?	method	Temperature	Width	$\Delta_0$	K, $\gamma$	Comments
Steinbinder '88 <sup>11</sup>	Nb(OH) <sub>0.002</sub> <sup>a</sup>	2 Single Crystals	Neutron Spectroscopy	10-160 K	2.3K	Used Ref (9) values	Assumed K=0.055	
	Nb(OH) <sub>0.01</sub>	Single Crystal			93 K	Used Ref (9) values		
Neumaier '89 <sup>12</sup>	Nb(OH) <sub>0.002</sub> <sup>a</sup>	2 single crystals	Neutron Spectroscopy	1.8 K	>17.4 K	2.6 K	?	This is a much broader width than Ref (11)
Steinbinder '91 <sup>13</sup>	Nb(OH) <sub>0.0002</sub>	Single Crystal	Neutron Spectroscopy	1.5 K and 10-160 K	1.16 K	2.6K	Assumed K=0.055	
Wang '83 <sup>14</sup>	NbN <sub>0.0015</sub> H <sub>0.0025</sub>	?	Attenuation at $\omega = 15$ & 195 MHz	Below 15 K	No distribution mentioned	Agree with 2.2 K		Used full electronic rate Relaxation peak moved with $\omega$ . 2.7K @ $\omega = 15$ 4.0K @ $\omega = 195$
Maschhoff '86 <sup>5</sup>	64ppm O, 49ppm N, 70ppm C, 700ppmH	Single crystal	Change in velocity at 10.8 MHz	Below 12 K	1.1K	SC= 2.2K N= 1.4 K <sup>b</sup>		
Gutsmeidl '87 <sup>10</sup>	NbN <sub>x</sub> H <sub>y</sub> series (0.00005 < x,y < 0.02)	Polycrystalline rods	Specific Heat	0.3 to 4 K	(10 ± 3) * N(at%)	2.02 ± 0.11K		Width of $\Delta_0 = 0.10K - low, \Delta_0 = 0.30 K - high$ concentration

Author/year	compound	Single crystal?	method	Temperature	Width	$\Delta_0$	K, $\gamma$	Comments
Morr '89 <sup>16</sup>	NbN <sub>0.0015</sub> H <sub>0.003</sub>	Single crystal	Attenuation & velocity at 30, 90, and 150 MHz	0.1 - 20 K	3 K	1.4 K	Found K = 0.07 $\gamma =$ 0.023eV	$\gamma$ found by assuming $n_0 =$ concentration of trapping centers
Steinbinder '91 <sup>13</sup>	Nb(NH) <sub>0.0005</sub>	Polycrystal	Neutron Spectroscopy	1.5K & 10-160 K	2.3K	1.9 K	As- sumed 0.055	$\Delta_0$ normal = 0.9 $\Delta_0$ sc
	Nb(NH) <sub>0.004</sub>	Polycrystal			25K	2.0 K		$\Delta_0$ from 1.5K measurement.
	Nb(NH) <sub>0.004</sub>	Single Crystal			35 K	2.0K		Higher concentration width is difficult to find
Neumaier '89 <sup>12</sup>	Nb(CH) <sub>0.0002</sub> <sup>c</sup>	2 polycrystal-line rods	Neutron Spectroscopy	1.8 K	2.3 K	1.88 K	?	

<sup>a</sup> all measurements denoted by <sup>a</sup> were done on the same sample

<sup>b</sup> SC = superconducting, N= normal

<sup>c</sup> The concentration is either 0.0002 or 0.002, it is inconsistent in the article.

- 
- <sup>1</sup> “Neutron spectroscopic evidence from hydrogen tunneling states in niobium”, H. Wipf, A. Magerl, S.M. Shapiro, S.K. Satija, and W. Thomlinson, *Physical Review Letters* 46, 947-950 (1981).
- <sup>2</sup> “Effect of the hydrogen tunneling states of the acoustic wave propagation in niobium at low temperatures”, G. Bellessa, *Journal de Physique – Lettres* 44, L-387 –L-391, (1983).
- <sup>3</sup> “Low temperature hydrogen tunneling in  $\text{NbO}_x\text{H}_y$  ( $x \approx 0.002$ ;  $y \approx 0.002$ )”, H. Wipf, K. Neumaier, A. Magerl, A. Heidemann and W. Stirling, *Journal of the Less-Common Metals* 101, 317-326 (1984).
- <sup>4</sup> “H and D tunneling in niobium”, H. Wipf and K. Neumaier, *Physical Review Letters* 52, 1308-1311 (1984).
- <sup>5</sup> “Quantum tunneling of trapped hydrogen in Nb”, E. Drescher-Krasicka and A.V. Granato, *Journal de Physique* 46, C10-73 – C10-80 (1985).
- <sup>6</sup> “Tunneling of H and D trapped by O(N) in niobium by anelastic relaxation measurements”, G. Cannelli, R. Cantelli, and F. Cordero, *Physical Review B* 34, 7721-7726 (1986).
- <sup>7</sup> “Concentration dependence and temperature dependence of hydrogen tunneling in  $\text{Nb}(\text{OH})_x$ ”, A Magerl, A.-J. Dianoux, H. Wipf, K. Neumaier, and I.S. Anderson, *Physical Review Letters* 56, 159- 162 (1986).
- <sup>8</sup> “The Influence of electrons on the tunneling state of a hydrogen atom in a metal”, H. Wipf, D. Steinbinder, K. Neumaier, P. Gutsmeidl, A. Magerl, and A.J. Dianoux, in *Quantum Aspects of Molecular Motions in Solids*, edited by A. Heidemann, A.

- 
- Magerl, M. Prager, D. Richter and T. Springer, (Springer Verlag, New York, 1987) pp. 153-157.
- <sup>9</sup> "Influence of the electronic state on H tunneling in niobium", H. Wipf, D. Steinbinder, K. Neumaier, P. Gutsmedl, A. Magerl, and A.J. Dianoux, *Europhysics Letters* 4, 1379-1384 (1987).
- <sup>10</sup> "H and D tunneling in Nb: dependence on defect concentration and trapping center", P. Gutsmeidl, M. Schiekhofer, K. Neumaier, and H. Wipf, in *Quantum Aspects of Molecular Motions in Solids*, edited by A. Heidemann, A. Magerl, M. Prager, D. Richter and T. Springer, (Springer Verlag, New York, 1987) pp. 158-162.
- <sup>11</sup> "Nonadiabatic low temperature quantum diffusion of hydrogen in Nb(OH)<sub>x</sub>", D. Steinbinder, H. Wipf, A. Magerl, D. Richter, A.-J. Dianoux and K. Neumaier, *Europhysics Letters* 6, 535-540 (1988).
- <sup>12</sup> "Tunneling of hydrogen in Nb(CH)<sub>0.0002</sub>", K. Neumaier, D. Steinbinder, H. Wipf, H. Blank, and G. Kearley, *Zeitschrift für Physik B* 76, 359-363 (1989).
- <sup>13</sup> "Low temperature tunneling and quantum diffusion of hydrogen Nb(NH)<sub>x</sub>", D. Steinbinder, H. Wipf, A.-J. Dianoux, A. Magerl, D. Richter, K. Neumaier, and R. Hemplemann, *Journal of the Less-Common Metals* 172-174, 685-692 (1991).
- "Quantum diffusion of trapped-hydrogen interstitials in Nb: the role of tunnel splitting", D. Steinbinder, H. Wipf, A.-J. Dianoux, A. Magerl, K. Neumaier, D. Richter, and R. Hemplemann., *Europhysics Letters* 16, 211-216 (1991).
- <sup>14</sup> "Acoustic absorption due to hydrogen tunneling in NbN<sub>0.0015</sub>H<sub>0.0025</sub>", J.L. Wang, G. Weiss, H. Wipf, and A. Magerl, in *Phonon Scattering in Condensed Matter*, edited by W. Eisenmenger, K. Laßmann, and S. Döttinger (Springer Verlag, New York,

1984), pp. 401-403.

<sup>15</sup> "Ultrasonic detection of an energy gap change in the N/S transition for trapped H in Nb", K.R. Maschhoff, E. Drescher-Krasicka, and A.V. Granato, in *Phonon Scattering in Condensed Matter V*, edited by A.C. Anderson and J.P. Wolfe (Springer-Verlag, New York, 1986), pp. 64-66.

<sup>16</sup> "Isotope dependence of hydrogen tunneling in niobium", W. Morr, A. Müller, G. Weiss, H. Wipf, and B. Golding, *Physical Review Letters* 63, 2084- 2087 (1989).

MICHIGAN STATE UNIV. LIBRARIES



31293016826376